Reduced Order Modeling of Near-wall and Roughness Sublayer Turbulence Using Resolvent Analysis

Thesis by
Miles Chan

In Partial Fulfillment of the Requirements for the
Degree of
Doctor of Philosophy

Caltech

CALIFORNIA INSTITUTE OF TECHNOLOGY
Pasadena, California

2025
Defended April 22, 2025

Miles Chan
ORCID: 0009-0007-7898-3739

ACKNOWLEDGEMENTS

During my PhD, I have enjoyed the camaraderie of many wonderful and supportive communities composed of my colleagues, mentors, friends, and family. All these people have supported and inspired me in my career, music, sports, and life. Without them, I could not have conducted the research presented in this thesis.

I theorize that it is impossible for any set of acknowledgments to fully resolve all the interpersonal interactions that have contributed to this endeavor, which is as much of the heart as of the mind. Therefore, I claim only to capture broader themes and that all omissions are errors arising from the honorable pursuit of brevity, for which I beg forgiveness.

My advisor, Dr. Beverley McKeon, has always been fair, kind, and honest in our interactions. I am thankful for her good taste in research problems and her advice which I have found invaluable in my research journey. Beverley led our group through COVID and a move to Stanford, making it possible for me to stay with the group and experience two different wonderful places to do graduate school. I will miss being able to pop in for a quick chat when the office door was open, which helped immensely with the smooth handling of countless research thoughts and logistical issues. She somehow manages to be available while managing her many responsibilities with admirable grace. I have had a wonderful experience working with Beverley, for which I am forever grateful.

I am also thankful for my good relationship with Dr. Ugo Piomelli, who has been very generous with his time and knowledge in our interactions. We have had many fun and insightful conversations about surface roughness, simulations, and music. His thoughts and questions have influenced and strengthened several aspects of this work.

I am also grateful for the other members of my committee, Dr. Dan Meiron and Dr. Anthony Leonard. Dan served as the option representative during my early years in the PhD program and taught my class in partial differential equations. During those tumultuous years, which included a global pandemic and virtual qualifying exams, Dan was an important resource for me and our student cohort, and I am very thankful for him. Tony was also present during much of my time at Caltech, always attending our group meetings and asking great questions. Therefore, it was very fitting that Dan and Tony were on my committee, and I am grateful for their questions and suggestions, which have improved this thesis.

It was a pleasure to work with my long-time collaborator on the wall-modeled LES project, Zvi Hantsis, who generously helped with many questions I had about simulations and analyzing rough wall flows. In addition to his duties on the wall modeling project, Zvi also produced the time-averaged roughness DNS data that is often referenced in this thesis and set up simulation code on our computing clusters, with which I have generated many useful datasets. It was also very cool to work briefly with Nam Hoang, who is pushing the wall modeling work forward now. I hope to see what he can achieve.

Thank you to all the members of Beverley's group whose company I have enjoyed over the years. I cherish the memories of our movie nights, dinners, and random conversations in our offices about a wide array of meaningful topics, such as the true definition of a sandwich. I will miss peeking over my cubical wall in Firestone to pepper Greg with math questions, deep philosophical discussions I shared with Tanner, Aaron parking himself at the empty desk next to me for camaraderie, wondering where Federico is, unlocking the office door for Claire MacDougall, and jumping out of an airplane with Yuting. I hope that Miya will find someone else to silently pop out of nowhere in her office with questions about triadic interactions in turbulence. I will miss the bountiful wisdom, silly jokes, wide smiles, and hearty laughter of the lab postdocs Tomek, Jonah, Facundo, Shilpa, Eric, and Teresa. We have commiserated and shared in each others' good moments, and as such I consider you all to be true friends who have a special place in my heart.

I would also like to thank my GALCIT friends, especially my first year classmates, for being my buddies through the zoom class era when we endured a global pandemic, studying in our rooms for virtual qualifying exams, and a terrible fire season in LA. I am so grateful for their friendship and care during those difficult times and beyond, when we were able to go on beach outings and play hilarious games of frisbee and flag football (at least, until Brayden's retirement!). My fond memories of these people include Peter's weekly nondimensional numbers and our practices for quals, Sorina's supreme ownership of the role of group mom, food adventures with Ying and Liam, driving Stephanie, Tracy, and Sahangi around in Yosemite, parties at John's, and Nikhil's grilled bell peppers.

I am also thankful for my Building 500 friends at Stanford, who welcomed me to a new place with open arms. I appreciate all the open office doors in the building and the many fun interactions I have had with many of you who work on wall-modeled large eddy simulations and experiments alike. I will miss our office and lunch discussions, revolving around Tony's political discussions, Murray's interest in ways of staying young, Tim's love of marmite, Carlos' unhinged takes on many subjects of general interest, and the universal topic of what constitutes a sandwich. I have particularly fond memories of our Lord of the Rings viewing parties and Mak's excellent cooking and cocktails.

In parallel with my experiences in research, I had a lovely time playing music with many wonderful people at Caltech and Stanford, particularly in the orchestral and chamber music communities. I am especially thankful for the four years that Ziyun, Vincent, Sam, and I spent working through so much of the string quartet repertoire. I always looked forward to our rehearsals inside and outside the Music House and at Sam's house in the hills. Our performances in many Caltech Chamber showcases, the Athenaeum Holiday Party, and in Sam's backyard for our friends are precious memories for me. I'm also grateful for Calen's Band Camp music parties; I always love seeing the passion for music and performance of all forms that people show in such an intimate, supportive environment, and some of my most memorable bouts of music-making have been here with Nathan, Nina, Étienne, and others. At Stanford, I also had a blast exploring the piano quartet, piano quintet, and string quartet literature with Daiyao, Ben, Cyrus, and Elisabeth. Many aspects of our work together had fantastic entertainment value, including our musical choices, fierce Dvořák-inspired rivalry with other chamber groups, and delicious oranges from Cyrus' tree. I am thankful to have learned so much from wonderful chamber coaches Maia, Martin, Stephen, and Dawn. I am especially grateful to my teacher at Stanford, Joo-Mee, who has added a lot of value to my brief stint at Stanford by encouraging my exploration of new repertoire, pursuit of competition and performance opportunities, and continued artistic growth.

Sports have also brought me a lot of joy, meaning, and camaraderie, and I have enjoyed countless wonderful adventures, training sessions, and races with dear friends at Caltech and Stanford. Caltech Triathlon gave me so many priceless memories, including savage Oxford hill repeats and track workouts, well earned spells in the hot tub after long swim sessions, fast laps of the Rose Bowl, and sweaty trips to Lucky Baldwin's. I really loved Wednesday and Saturday morning trail runs through the San Gabriel and Angeles mountains with the Caltech Alpine club runners. Long adventure rides at team camp, Collegiate Nationals, and countless pleasant coffee rides with Stanford Cycling are also big highlights for me. I have spent meaningful and memorable times with so many wonderful athletes that it is truly overwhelming trying to list all your names. So, I will do my best, and patch the rest using academia-speak. Thank you Angus, Annette, Matias, Ryan, Scott, William, Stephanie, Carina, Marshall, Shae, Jack, Lindsey, Rob, Calen, Maria, Ashley, Sam, Aubrey, Daniel, Pippa, Paddy, Cris, Ed, Adele, Adrian, Carlos, Alex, Claire, Gina, Jack, Jess, Matt, Michael, Murray, Nikhil, Owen, Rohit, et al. for all the love, kudos, and stoke.

A special thank you goes to my undergraduate advisor Dr. David Hu and graduate student mentor Dr. Patricia Yang, who were instrumental at the beginning of my research career. I am thankful that my memories of delving into the mysteries of wombat feces with them are fond, though somewhat odorous.

I am also grateful for all the friends I've made along the way. I think often of my teammates and the mentors of my high school robotics team, who fostered my desire to pursue a career in STEM and continue to inspire me with their hard work and achievements. I'm thankful for Claire Bang, whose continued friendship and blunt honesty I find invaluable. I am grateful for my undergraduate roommates Ben, Elena, Eric, and Asutosh, who hold a special place in my heart.

Finally, I am thankful for my family. My mother has always supported and loved me unconditionally, which has allowed me to pursue my dreams with reckless abandon. When I was young, she made sure I was able to attend orchestra rehearsal, robotics club meetings, and cross country practice, fostering my enduring love of music, science, and sports, activities which have brought me so much friendship and fulfillment in my life. I acknowledge my father, whose beliefs in the importance of education and hard work I share. I am grateful for the good and mutually-supportive relationship I have with my sibling Morgan, whose supreme passion for music inspires me to pursue my own dreams with vim and vigor.

ABSTRACT

Modeling near-wall and roughness sublayer turbulence using physics-based methods remains a topic of paramount importance, since most engineering-relevant flows are turbulent and most surfaces are not smooth. While today there exists a wide range of empirical, data-driven modeling approaches for turbulence, these methods are limited because fully resolved turbulence data remains expensive to generate and burdensome to store and analyze. Therefore, the ability to predict out-of-sample is important, and since data-driven methods struggle to extrapolate, developing physics-based approximations that give useful, inexpensive predictions remains necessary. Yet the complexity of near-wall turbulence makes developing theoretical models difficult. This thesis tackles two main challenges. First, methods for reduced order modeling of the sensitivity of turbulence to multiscale, engineering-relevant roughness geometries are developed. In particular, a physics-based method for incorporating a drag-scaled, Reynolds-decomposed volume penalization into resolvent analysis yields a linear reduced order model that gives computationally inexpensive estimates for roughness sublayer fluctuations and dispersive stresses given a surface geometry and the mean flow profile in a rough wall channel flow. Then, an iterative method is developed to predict the mean flow profile, equivalent sand grain roughness, and Hama roughness function that utilizes the discovered relationship between the fluctuations and the mean flow. That model yields a closed-loop system for predicting roughness sublayer turbulence and the mean response given only a scan of the roughness geometry and a bulk Reynolds number in a rough wall channel flow. Second, a methodology for generating spatiotemporal representations of near-wall turbulence with very few degrees of freedom is developed. It utilizes a coarse-graining approach to reduce the number of modes required to describe a turbulent flow, selection criteria for picking descriptive modes, and Reynolds number scaling to provide predictions for an out-of-sample, higher Reynolds number flow. A spatiotemporal representation is generated, and results from Piomelli et al. that incorporate the modal representation into the wall layer of a wall modeled large eddy simulation are presented. Overall, this thesis contributes new reduced order modeling approaches that make use of physics-based insights to tackle outstanding problems in the prediction of near-wall and roughness sublayer turbulence.

PUBLISHED CONTENT AND CONTRIBUTIONS

Chan, M., U. Piomelli, and B. J. McKeon (2024). "Coarse-grained representations of near-wall turbulence using resolvent analysis". In: *Annual Research Briefs*. Center for Turbulence Research, Stanford University.
M.C. developed the modeling methodology, generated the data, performed the analysis, and was the primary author of the paper.

TABLE OF CONTENTS

LIST OF ILLUSTRATIONS

LIST OF TABLES

Chapter 1

INTRODUCTION

1.1 Motivation

Turbulence is in the tempestuous swirling of gases inside a star, oil gushing through a pipeline, and the wind passing over an airplane wing; it is ubiquitous in fluid flows of universal significance and human relevance. Anyone who has experienced a bumpy ride in a commercial aircraft is aware of the effects of clear air turbulence that occurs on an atmospheric scale. However, even when the aircraft is in calm air and the passengers are comfortable, turbulence on a smaller scale still occurs close to the surfaces of the wing, tail, and body of the aircraft. The character of this near-wall turbulence is sensitive to any roughness on the surface that arises from various sources, including manufacturing processes, corrosion, biofouling, ice accretion, and by design (Kadivar et al., 2021). Near-wall turbulence enhances mixing and momentum transport near those surfaces, and is responsible for an increase in drag of up to 50% for a modern airliner (Marusic, Mathis, et al., 2010).

Due to the universality and profound impact of turbulence in nature and engineering applications, scientists and engineers have devoted themselves to its study for over a century. Yet a complete understanding of turbulence remains elusive. The notorious intractability of turbulence can be understood by considering the governing equations of fluid motion, the Navier-Stokes equations (NSE).

In the Newtonian, incompressible flows considered in this thesis, the NSE enforce conservation of mass and momentum. These equations are nonlinear, which means that the interaction between different scales of motion is important for the system. Furthermore, the range of scales represented in turbulent flows is enormous. That separation of scales is captured by the Reynolds number, which is the ratio between inertial and viscous forces. Below a critical Reynolds number, the flow remains laminar. However, above that critical Reynolds number, the flow transitions to turbulence (Reynolds, 1883). For aerospace vehicles, the range of scales that must be considered ranges from the micrometer scale of near-wall motions and surface roughness to the tens or hundreds of meters that characterize the aerodynamic body shape, which is a scale separation of $O(10^6 - 10^8)$. For high Reynolds number flows relevant to engineering and geophysical applications, a full-fidelity evaluation of the exact Navier-Stokes equations that resolves all the relevant scales is intractable for modern and foreseeable computational power.

Despite the fact that directly solving for the turbulent flow is impractical in many circumstances, there remains an ever-present need to provide information about the turbulence in systems of human relevance. Therefore, turbulence research is concerned with the development of modeling approaches that replace some or all of the fidelity of the full NSE with simplified relations and equations that approximate turbulence or flow quantities of interest. Turbulence research also involves developing and applying methods for analyzing and understanding the observed structure of turbulent flows. Most of these methods rely on the key observation that while turbulence can be usefully understood as stochastic, it also contains coherent structures (Kline et al., 1967; Brown and Roshko, 1974). Furthermore, these structures appear to have an organized distribution of sizes and display self-similarity. Townsend, 1976 codified this in his attached eddy hypothesis, which models turbulence using hierarchies of geometrically self-similar eddies. The attached eddy idea is powerful and has been profitably implemented to model turbulent stresses (Perry and Chong, 1982; Moarref, Sharma, et al., 2014).

The existence of dominant coherent structures in turbulence has prompted a high degree of interest in reduced order modeling of turbulence. These methods are based on the description of high-dimensional systems and/or data as the sum of weighted basis functions called modes, which can be determined based on data or governing equations. These modal decompositions are attractive for describing phenomena in which dominant structures or trends exist, because it is reasonable to expect that only a corresponding subset of the possible basis functions is strongly represented. It is possible then to construct reduced-order models of physical phenomena by considering only the dominant subset of basis functions. These approaches can achieve a great degree of freedom reduction, which can lead to increased computational efficiency and model interpretability. Therefore, the study of how to determine modes, which modes are active, and how to model their weights in turbulent flows is a topic of interest to the scientific community.

Reduced order models can be roughly classified into physics-based and data-driven approaches, although aspects based on observation and physical intuition pervade both types of models. The distinction is related to how the modes and their weights are determined. The proper orthogonal decomposition (POD) and its implementation in wave number space, spectral POD (SPOD), are examples of data-driven methods where weights and modes are determined from data (Lumley, 1970; Towne et al., 2018). Resolvent analysis is an equation-based method that determines modes from the linearized Navier-Stokes equations and an exact relation for the weights (McKeon and Sharma, 2010). The two types of models are useful in particular scenarios. When data is abundant and accurate governing equations are not known, data-driven models are a natural choice. When data is scarce but the governing equations describe the system well, physics-based approaches offer more generalizable results. Since fully-resolved data for turbulence is challenging to generate and burdensome to store and share, there remains a strong need for physics-based reduced order modeling techniques that give more universal insights.

Surface roughness adds another layer to the modeling challenge posed by classical wall-bounded turbulence, which is significant given the ubiquity of roughness in engineering flows. Despite decades of study, there is no comprehensive theory for the sensitivity of turbulence and flow quantities of interest to features of the surface roughness. In lieu of this, scientists have devised a plethora of empirical approximations and machine-learning models using data from experiments and geometry-resolving simulations, as well as physics-based models applicable to idealized geometries. Given the extreme expense of performing simulations and experiments at Reynolds numbers in the fully rough regime across the whole range of conceivable surface geometries, it is fair to ask if reduced order modeling techniques for roughness can contribute to deeper understanding and modeling of this problem.

The present thesis contributes to the development and application of reduced-order modeling methods for analyzing and predicting near-wall and roughness sublayer turbulence. First, a physics-based reduced order modeling framework is developed that yields a linear transfer function relating a multiscale, engineering-relevant roughness geometry to the spatially-varying turbulent flow response in the roughness sublayer. That framework is used to provide quantitatively reasonable predictions for the response of turbulent fluctuations, stresses, mean flow profile, and drag to a particular surface geometry, given minimal empirical assumptions. This approach models the spatially-varying flow sensitivity to features of the surface roughness, yielding physical insights into rough wall flows that are not provided by empirical models that seek only the mean or drag response from roughness statistics or spectra. Second, a method is developed for coarse-graining spatiotemporal representations of near-wall turbulence which greatly reduces the degrees of freedom required to describe turbulent motions.

1.2 Similarity and modeling of roughness in wall-bounded turbulent flows

The turbulent flow over surface roughness can no longer be parameterized by the Reynolds number alone, since the geometrical features of the roughness geometry affect the drag and set the scales of the observed turbulent motions. However, important behavioral similarities are observed between smooth and rough wall-bounded turbulent flows that are foundational for historical and present modeling efforts.

Nikuradse, 1933 conducts a systematic study of sand grain roughness with different grain sizes and Reynolds numbers and observes that both smooth and rough pipe flows scale with the friction velocity u_τ and fluid viscosity ν, the mean flow profiles are similar in the outer layer far from the wall, and the friction factor becomes constant above a certain Reynolds number. Colebrook, 1939 introduces the equivalent sand grain roughness k_s^+, which is a hydrodynamic quantity that relates a given surface roughness to the grain dimension of the sand grain roughness that produces the same friction factor or drag at a given Reynolds number. Hama, 1954 introduces the shift between the smooth and rough wall mean flow profiles for flows observing outer layer similarity at a given Reynolds number, ΔU^+. That shift can also be interpreted as a change in the virtual origin of the wall d, where if statistics are plotted against $y - d$, the profiles of the mean and statistics collapse in the outer layer (Chung et al., 2021). For fully rough, zero pressure gradient flows, d can be taken as the centroid of the drag force (Jackson, 1981). Oftentimes, k_s^+, ΔU^+, or d are quantities of interest for engineers in a rough wall flow, as they characterize the response of the mean flow profile to a rough geometry as compared with a smooth wall, assuming outer layer similarity.

Outer layer similarity can be observed in the mean flow and second-order statistics, and is expected to hold for a sufficient separation between the roughness scale k and outer length scales of the flow δ. Jiménez, 2004 provides the guideline $\delta/k \gtrsim 50$ for flows that are expected to respect outer layer similarity. In flows that respect outer similarity, the effects of roughness are confined to the roughness sublayer, a region of the flow that extends to approximately $y = 2 - 5k$ (Raupach, 1981). In flows over obstacles where $\delta/k \lesssim 50$ or where long length scales in the streamwise or spanwise directions are present, roughness effects can be expected to extend through the outer region.

In many engineering contexts at high Reynolds number, the scales of roughness are small with relation to the outer scales of fluid motion, so outer similarity is respected. Therefore, this thesis considers only turbulent flows over surface roughness with outer similarity. In these flows, the turbulence in the outer region feels the presence of the surface roughness only indirectly, through the drag and scales of motion set in the roughness sublayer. Meanwhile, the roughness sublayer turbulence that determines the drag and roughness scales depends spatially on the specific geometric attributes of the surface roughness.

Many efforts for modeling the effects on turbulence over realistic, multiscale surface geometries bypass the details of the spatially-varying roughness sublayer fluctuations and focus instead on directly predicting the drag-related flow quantities k_s^+ and/or ΔU^+ given statistics and spectral information about the roughness using empirical models. There is a large body of literature on the development of fitted equations to relate surface statistics to roughness flow parameters, which is well reviewed by Flack and Chung, 2022. Due to the difficulty inherent in discovering truly generalizable fitted equations, several efforts have been made to link surface statistics and spectral information to roughness flow parameters by training neural networks (Aghaei Jouybari et al., 2021; S. Lee et al., 2022; Yang et al., 2023). These methods are useful for predicting drag for rough surfaces without considering the complex, spatially-varying turbulent flow response in the roughness sublayer. However, as with all data-driven methods, generalizing outside the training dataset remains an issue.

For modeling the mean flow profile, Bornhoft, 2024 and Brereton and Yuan, 2018 give empirically-fitted relations between the statistics of the roughness and k_s^+ to the shape of the mean flow profile for use in WMLES. These methods are practical for usage in a wall model, but do not provide a method for predicting k_s^+, which is an input to the analysis.

Therefore, it remains desirable to develop more generalizable models, and it is natural to seek model forms that more directly encode the physics that link roughness features to the drag response through modeling the roughness sublayer fluctuations and their spatially-varying effects. However, the complexity of turbulent motions observed over realistic roughness geometries has made theoretical development extremely challenging. One promising physics-based effort is the wind shade model of Meneveau et al., 2024 that uses minimal empirical assumptions to link surface features of realistic roughness to the resulting drag.

For modeling turbulent fluctuations and stresses arising from surface roughness, recent studies have focused on idealized or filtered roughness geometries, with the goal of identifying important scales and patterns that can be generalized to realistic surfaces. Mejia-Alvarez and Christensen, 2010 fabricates 3D-printed low order representations of a wind turbine roughness using subsets of POD modes and compares their performance in wind tunnel testing. A 16 mode POD representation is found to produce similar stresses as the original 383 mode surface, indicating that only certain geometric scales contribute to the drag response. Studies of Fourier-filtered roughness are also suggestive of the importance of different scales in determining the flow response (Alves Portela et al., 2021). Morgan, 2019 studied sinusoidal roughness in a wind tunnel, finding a linear response in the time averaged field and suggesting that the flow over realistic surfaces may be determined by superposing the flow responses to a linear combination of simple roughness geometries.

None of these models provide predictions for a realistic roughness. Therefore, there remains a need for a generalizable, inexpensive model that predicts the sensitivity of the spatially-varying turbulent fluctuations and drag response to features of a multiscale, realistic roughness geometry. Also, the question of whether linear trends can be used to give quantitatively useful predictions is unanswered by these studies. The present thesis tackles these challenges.

1.3 Reduced order modeling of turbulence

Reduced order models are based on spatiotemporal representations of turbulence consisting of the superposition of weighted modes, each embodying different spatial and temporal scales. There exists a wide variety of data-driven and physics-based methods to determine modes and weights that describe turbulence.

The Fourier transform is a rational choice for analyzing flows with homogeneous directions; for the flows considered in this thesis, the Fourier transform is taken in the homogeneous streamwise and spanwise directions, resulting in Fourier modes parameterized by wave number that are coherent in the wall-normal direction. This technique can be applied to the governing equations as well as the data.

Data-driven methods for generating modal representations include POD, SPOD, and DMD (Lumley, 1970; Schmid, 2010). POD seeks a set of modes that optimally capture the variance of an ensemble of flow data, while DMD gives modes that optimally describe the dynamic motions of the flow. SPOD is the spatiotemporal counterpart of POD for a statistically stationary flow, giving converged spatiotemporal modes at

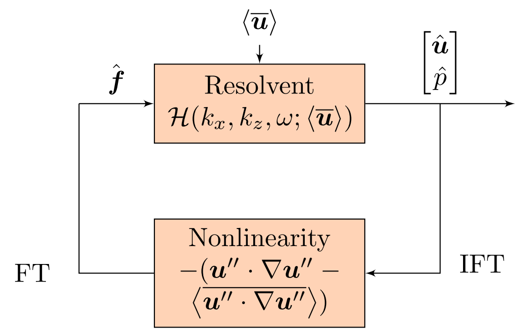

Figure 1.1: Resolvent analysis.

each frequency. These methods, and particularly SPOD, are data-intensive because they rely on many realizations of a flow to obtain converged mode shapes.

Resolvent analysis of the NSE, developed by McKeon and Sharma, 2010 provides a physics-based method for generating efficient, descriptive modal bases for turbulent flows. Resolvent analysis is an exact expression of the NSE linearized about the turbulent mean and forced with the nonlinear term in the fluctuations. It can be understood as a self-sustaining, closed-loop system consisting of the resolvent operator, which serves as a transfer function relating the endogenous forcing from the nonlinear term to the flow response, as illustrated in Figure 1.1. For the flows in this thesis, resolvent analysis is derived from the NSE Fourier transformed in time and the homogeneous streamwise and spanwise directions. In this case, for a given wave number, the resolvent operator relates the forcing at that wave number to the response at the same wave number. Taking the SVD of the resolvent operator yields response modes, gains, and forcing modes. The resolvent operator has been shown to be low rank at wave numbers where turbulence is energetic, meaning that the first (few) SVD modes have much larger gains than those of the remaining modes. Therefore, resolvent response modes are a reasonable choice for developing a low-rank basis for reconstructing or modeling the flow response. The projection of the nonlinearity onto the forcing modes gives an exact expression for the mode weights. However, exact calculation of the weights requires the loop to be closed, which is challenging to implement. Approximate treatments of the weights can give approximate solutions, and in this way resolvent analysis successfully provides low order models for turbulent spectra (Moarref, Sharma, et al., 2013; Moarref, Jovanović, et al., 2014). An advantageous aspect of using a resolvent mode basis for describing turbulent flows is the potential applicability of Reynolds number scalings for resolvent modes and singular values developed by Moarref, Sharma, et al., 2013, as well as for resolvent weights that represent self-sustaining turbulence and agree with classical turbulence theories such as the attached eddy hypothesis by Moarref, Sharma, et al., 2014. Therefore, from weighted resolvent mode bases, it should be possible to develop predictions that apply in other turbulent flows, and this thesis begins some preliminary work in this direction.

Resolvent analysis has been extended to accommodate non-spatially uniform boundary conditions, including linearized velocity-pressure conditions for compliant walls (Luhar et al., 2015; Huynh et al., 2021), velocity conditions for opposition control (Toedtli, Luhar, et al., 2019; Toedtli, Yu, et al., 2020), and perforated surfaces (Jafari et al., 2023). For modeling roughness, Chavarin and Luhar, 2020 develops a volume penalization method using a permeability function that drives the velocities to 0 in the solid region and is set to 0 in the fluid region, and applies the method to streamwise riblets. Flynn et al., 2024 has developed an approach to represent roughness using a projection-based immersed boundary method and applied it to a sinusoidal roughness. All the resolvent analysis methods developed for roughness rely on the solution of wave-number-coupled systems, and have therefore been limited to systems that can be well described by a single wave number and its harmonics.

SPOD and resolvent analysis are closely connected. For uncorrelated forcing, SPOD and resolvent modes are equivalent, and to obtain the best reconstruction of the SPOD statistics using resolvent modes, resolvent weights must be determined by the best projection onto the SPOD modes using a statistical rather than deterministic understanding of the weights (Towne et al., 2018).

1.4 Thesis Outline

Chapter 2 introduces methods for relating velocity and pressure fluctuations to drag forces in rough wall-bounded flows, resolvent analysis, and spectral proper orthogonal decomposition. Chapter 3 analyzes linear trends observed in resolvent mode representations of the temporally-averaged, spatially-varying roughness sublayer fluctuations in the presence of surface roughness, and shows what drag-related quantities are captured by these representations. Chapter 4 develops a drag-normalized, Reynolds-decomposed treatment of resolvent analysis with volume penalization (RAVP) to predict roughness sublayer fluctuations and dispersive stresses given a mean flow profile and a surface scan of an engineering-relevant, multiscale roughness in a channel flow. Chapter 5 details a modeling approach that predicts the mean flow profile and drag response given a surface roughness geometry in a channel flow with a given bulk Reynolds number, using an iterative framework that leverages the link between the mean flow profile, surface scan, and dispersive stresses encoded in RAVP. Chapter 6 introduces a framework for constructing data-driven reduced-order models of turbulent fluctuations at high Reynolds numbers from resolvent representations constructed using data collected at computationally-feasible Reynolds numbers. Finally, Chapter 7 draws conclusions and identifies pathways for future research.

Chapter 2

METHODS

2.1 Averaging operators and the triple decomposition for rough wall flow

When considering the temporally-averaged turbulent flow over surface roughness, spatial variation is readily observed. Therefore, spatial and temporal averaging must be considered separately.

Intrinsic, superficial, and planar spatial averages

First, define the area occupied by fluid at a particular y-height to be A_f. The domain area at that y-height is $A_t = L_x \times L_z$. Then, the intrinsic average of a flow quantity $q(x, y, z, t)$ can be written

$$\langle q \rangle (y, t) = \frac{1}{A_f} \int_{A_f} q(x, y, z, t) dA. \tag{2.1}$$

The superficial average can then be written

$$\langle q \rangle_s (y, t) = \frac{1}{A_t} \int_{A_f} q(x, y, z, t) dA. \tag{2.2}$$

Note that both averages are computed with integrals over the area occupied by fluid. The plane average is the usual definition,

$$\langle q \rangle_{xz} (y, t) = \frac{1}{A_t} \int_{A_t} q(x, y, z, t) dA. \tag{2.3}$$

When there is no roughness, all these averages are observed to collapse because $A_t = A_f$ in this case.

Triple decomposition for rough wall flow quantities

The Reynolds decomposition decomposes a turbulent flow into a mean and fluctuations about that mean. Here, the flow quantity is decomposed into a temporal average and temporal fluctuations,

$$q(x, y, z, t) = \overline{q}(x, y, z) + q'(x, y, z, t). \tag{2.4}$$

In a smooth wall turbulent channel flow, the temporal average does not vary in the streamwise or spanwise directions (x, z), so the temporal average is equal to the spatiotemporal average, $\langle\overline{q}\rangle = \overline{q}$. However, in a rough wall turbulent channel flow, the temporal average has spatial variation, $\langle\overline{q}\rangle \neq \overline{q}$. The temporal average can be further decomposed into the spatiotemporal average and wake field,

$$\overline{q}(x, y, z) = \langle\overline{q}\rangle(y) + \tilde{q}(x, y, z) \tag{2.5}$$

which leads to the triple decomposition,

$$q(x, y, z, t) = \langle\overline{q}\rangle(y) + \tilde{q}(x, y, z) + q'(x, y, z, t). \tag{2.6}$$

Also, define the sum of wake field and temporal fluctuations,

$$q''(x, y, z, t) = \tilde{q}(x, y, z) + q'(x, y, z, t), \tag{2.7}$$

so that the following holds:

$$q(x, y, z, t) = \langle\overline{q}\rangle(y) + q''(x, y, z, t). \tag{2.8}$$

2.2 Fourier transform

The Fourier transform in time and the streamwise and spanwise directions is natural for the streamwise- and spanwise-homogeneous flows studied in this thesis. The Fourier transform pair used is

$$\begin{aligned}\hat{q}(y; k_x, k_z, \omega) &= \int_{-\infty}^{\infty}\int_{-\infty}^{\infty}\int_{-\infty}^{\infty} q(x, y, z, t)e^{-i(k_x x + k_z z - \omega t)}dxdzdt \\ q(x, y, z, t) &= \int_{-\infty}^{\infty}\int_{-\infty}^{\infty}\int_{-\infty}^{\infty} \hat{q}(y; k_x, k_z, \omega)e^{i(k_x x + k_z z - \omega t)}dk_x dk_z d\omega.\end{aligned} \tag{2.9}$$

2.3 Resolvent analysis

Begin with the incompressible, Newtonian Navier-Stokes equations. Time is nondimensionalized by δ/u_τ, spatial coordinates by δ, pressure by ρu_τ^2, and velocity by u_τ.

$$\begin{aligned}\frac{\partial u_i}{\partial t} + u_j\frac{\partial u_i}{\partial x_j} &= -\frac{\partial p}{\partial x_i} + \frac{1}{Re_\tau}\frac{\partial^2 u_i}{\partial x_j \partial x_j} \\ \frac{\partial u_i}{\partial x_i} &= 0.\end{aligned} \tag{2.10}$$

Apply the Reynolds decomposition $q(\mathbf{x}, t) = \langle\overline{q}\rangle(y) + q''(\mathbf{x}, t)$, and take the spatiotemporal average,

$$\begin{aligned}&\frac{\partial u_i''}{\partial t} + \langle\overline{u}_j\rangle\frac{\partial\langle\overline{u}_i\rangle}{\partial x_j} + u_j''\frac{\partial\langle\overline{u}_i\rangle}{\partial x_j} + \langle\overline{u}_j\rangle\frac{\partial u_i''}{\partial x_j} + u_j''\frac{\partial u_i''}{\partial x_j} \\ &= -\frac{\partial(\langle\overline{p}\rangle + p'')}{\partial x_i} + \frac{1}{Re_\tau}\frac{\partial^2(\langle\overline{u}_i\rangle + u_i'')}{\partial x_j \partial x_j}\end{aligned} \tag{2.11}$$

$$\left\langle \overline{u}_j \right\rangle \frac{\partial \left\langle \overline{u}_i \right\rangle}{\partial x_j} + \left\langle \overline{u''_j \frac{\partial u''_i}{\partial x_j}} \right\rangle = -\frac{\partial \left\langle \overline{p} \right\rangle}{\partial x_i} + \frac{1}{Re_\tau} \frac{\partial^2 \left\langle \overline{u}_i \right\rangle}{\partial x_j \partial x_j}. \tag{2.12}$$

Subtract the spatiotemporally averaged equation to obtain the equations for the fluctuations, assuming that $\langle \overline{v} \rangle = \langle \overline{w} \rangle = 0$,

$$\begin{aligned} \frac{\partial u''_i}{\partial t} + \langle \overline{u} \rangle \frac{\partial u''_i}{\partial x} + v'' \frac{d \left\langle \overline{u}_i \right\rangle}{dy} - \frac{1}{Re_\tau} \frac{\partial^2 u''_i}{\partial x_j \partial x_j} + \frac{\partial p''}{\partial x_i} &= -\left(u''_j \frac{\partial u''_i}{\partial x_j} - \left\langle \overline{u''_j \frac{\partial u''_i}{\partial x_j}} \right\rangle \right) \\ \frac{\partial u''_i}{\partial x_i} &= 0. \end{aligned} \tag{2.13}$$

Take the Fourier transform in time and the homogeneous spatial directions x and z of the NSE to obtain, noting that $\Delta \triangleq \frac{\partial^2}{\partial y^2} - k_x^2 - k_z^2$,

$$\begin{aligned} \left(-i\omega + ik_x \langle \overline{u} \rangle - \frac{1}{Re_\tau} \Delta \right) \hat{u} + \frac{d \langle \overline{u} \rangle}{dy} \hat{v} + ik_x \hat{p} &= \hat{f}_1 \\ \left(-i\omega + ik_x \langle \overline{u} \rangle - \frac{1}{Re_\tau} \Delta \right) \hat{v} + \frac{d\hat{p}}{dy} &= \hat{f}_2 \\ \left(-i\omega + ik_x \langle \overline{u} \rangle - \frac{1}{Re_\tau} \Delta \right) \hat{w} + ik_z \hat{p} &= \hat{f}_3 \\ ik_x \hat{u} + \frac{d\hat{v}}{dy} + ik_z \hat{w} &= 0, \end{aligned} \tag{2.14}$$

where

$$\hat{f}_i \triangleq -\widehat{\left(u''_j \frac{\partial u''_i}{\partial x} - u''_j \left\langle \overline{\frac{\partial u''_i}{\partial x}} \right\rangle \right)}. \tag{2.15}$$

Then, the resolvent formulation in primitive variables is written

$$\begin{bmatrix} \hat{\mathbf{u}} \\ \hat{p} \end{bmatrix} = \underbrace{\left(-i\omega \begin{bmatrix} \mathbf{I} & \\ & 0 \end{bmatrix} - \begin{bmatrix} \mathcal{L}_\mathbf{k} & -\nabla \\ \nabla^\top & 0 \end{bmatrix} \right)^{-1} \begin{bmatrix} \mathbf{I} \\ 0 \end{bmatrix}}_{\text{Resolvent } \mathcal{H} \in \mathbb{C}^{4N_y \times 3N_y}} \hat{\mathbf{f}}, \tag{2.16}$$

where

$$\begin{aligned} \mathcal{L}_\mathbf{k} &\triangleq \begin{bmatrix} -ik_x \langle \overline{u} \rangle + Re_\tau^{-1} \Delta & \partial_y \langle \overline{u} \rangle & \\ & -ik_x \langle \overline{u} \rangle + Re_\tau^{-1} \Delta & \\ & & -ik_x \langle \overline{u} \rangle + Re_\tau^{-1} \Delta \end{bmatrix} \\ \nabla &\triangleq \begin{bmatrix} ik_x \\ \frac{\partial}{\partial y} \\ ik_z \end{bmatrix}, \quad \hat{\mathbf{u}} \triangleq \begin{bmatrix} \hat{u} \\ \hat{v} \\ \hat{w} \end{bmatrix}, \quad \hat{\mathbf{f}} \triangleq \begin{bmatrix} \hat{f}_1 \\ \hat{f}_2 \\ \hat{f}_3 \end{bmatrix}, \end{aligned} \tag{2.17}$$

or in the shorter form

$$\begin{bmatrix} \hat{\mathbf{u}} \\ \hat{p} \end{bmatrix} = \mathcal{H}\hat{\mathbf{f}}. \tag{2.18}$$

Using the SVD $\mathcal{H} = \sum_{j=1}^{N} \sigma_j \psi_j \phi_j^{\dagger}$, a modal representation can be written for the velocity fluctuations,

$$\begin{bmatrix} \hat{\mathbf{u}} \\ \hat{p} \end{bmatrix} = \sum_{j=1}^{N} \sigma_j \psi_j \chi_j \quad \text{where} \quad \chi_j = \left\langle \phi_j, \hat{\mathbf{f}} \right\rangle. \tag{2.19}$$

2.4 SPOD

In this section, SPOD is derived following the procedure of Nekkanti and Schmidt, 2021. Calculating SPOD begins with a time series of data arranged into columns $\mathbf{q}_i = \mathbf{q}(t_i)$ where $i = 1, ..., n_t$. In this thesis, the data is already transformed in the spatial homogeneous directions, x and z. From this time series, a snapshot matrix is constructed,

$$\mathbf{Q} = \left[\mathbf{q}_1, \mathbf{q}_2, \ldots, \mathbf{q}_{n_t}\right]. \tag{2.20}$$

The energy of each snapshot is expressed in terms of a spatial inner product over the domain of interest Ω,

$$||\mathbf{q}||_x^2 = \langle \mathbf{q}, \mathbf{q} \rangle_x = \int_\Omega \mathbf{q}^*(x,t)\mathbf{W}(x)\mathbf{q}(x,t)\mathrm{d}x, \tag{2.21}$$

where W is a positive definite Hermitian weight matrix. SPOD determines optimal modes in the sense of the space-time inner product for statistically stationary data,

$$||\mathbf{q}||_{x,t}^2 = \langle \mathbf{q}, \mathbf{q} \rangle_{x,t} = \int_{-\infty}^{\infty} \int_\Omega \mathbf{q}^*(x,t)\mathbf{W}(x)\mathbf{q}(x,t)\mathrm{d}x\ \mathrm{d}t. \tag{2.22}$$

Then, blocks of the Fourier-transformed data are assembled,

$$\mathbf{Q}^{(k)} = \left[\mathbf{q}_1^{(k)}, \mathbf{q}_2^{(k)}, \ldots, \mathbf{q}_{n_{fft}}^{(k)}\right]. \tag{2.23}$$

Each block is considered to be a statistically independent realization of the flow. A Hamming window is applied to each block to reduce the spectral leakage,

$$w(i+1) = 0.54 - 0.46\cos\left(\frac{2\pi i}{n_{fft} - 1}\right) \qquad \text{for } i = 0, 1, \ldots, n_{fft} - 1. \tag{2.24}$$

Then, the discrete Fourier transform is taken on each windowed block,

$$\hat{\mathbf{q}}_j^{(k)} = \mathcal{F}\left\{w(j)\mathbf{q}_j^{(k)}\right\}, \tag{2.25}$$

to create the Fourier-transformed data matrix,

$$\hat{\mathbf{Q}}^{(k)} = \left[\hat{\mathbf{q}}_1^{(k)}, \hat{\mathbf{q}}_2^{(k)}, \ldots, \hat{\mathbf{q}}_{n_{fft}}^{(k)}\right], \tag{2.26}$$

where $\hat{\mathbf{q}}_i^{(k)}$ denotes the k-th Fourier realisation at the i-th discrete frequency. Then, for each frequency l, the matrix

$$\hat{\mathbf{Q}}_l = \left[\hat{\mathbf{q}}_l^{(1)}, \hat{\mathbf{q}}_l^{(2)}, \ldots, \hat{\mathbf{q}}_l^{(n_{blk})}\right] \tag{2.27}$$

is constructed. From this matrix, the SPOD modes, $\mathbf{\Phi}$, and energies, λ, can be computed as the eigenvectors and eigenvalues of the cross-spectral density (CSD) tensor $\mathbf{S}_l = \hat{\mathbf{Q}}_l \hat{\mathbf{Q}}_l^*$. The snapshot approach is taken for efficiency, since the number of spatial degrees of freedom n greatly exceeds the number of realizations,

$$\frac{1}{n_{blk}} \hat{\mathbf{Q}}_l^* \mathbf{W} \hat{\mathbf{Q}}_l \mathbf{\Upsilon}_l = \mathbf{\Upsilon}_l \mathbf{\Lambda}_l. \tag{2.28}$$

Then, the coefficients $\mathbf{\Upsilon}_l = \left[\upsilon_l^{(1)}, \upsilon_l^{(2)}, \ldots, \upsilon_l^{(n_{blk})}\right]$ that expand the SPOD modes in terms of the Fourier realizations are used to recover the SPOD modes,

$$\mathbf{\Phi}_l = \frac{1}{\sqrt{n_{blk}}} \hat{\mathbf{Q}}_l \mathbf{\Upsilon}_l \mathbf{\Lambda}_l^{-1/2}. \tag{2.29}$$

The matrices $\mathbf{\Lambda}_l = \operatorname{diag}\left(\lambda_l^{(1)}, \lambda_l^{(2)}, \ldots, \lambda_l^{(n_{blk})}\right)$, where by convention $\lambda_l^{(1)} \geq \lambda_l^{(2)} \geq \cdots \geq \lambda_l^{(n_{blk})}$, and $\mathbf{\Phi}_l = \left[\phi_l^{(1)}, \phi_l^{(2)}, \ldots, \phi_l^{(n_{blk})}\right]$ contain the SPOD energies and modes, respectively.

Reconstructing data in the frequency domain using SPOD

Then, SPOD can be used to reconstruct the data in the frequency domain. The original realizations of the Fourier transform at each frequency l can be written

$$\hat{\mathbf{Q}}_l = \mathbf{\Phi}_l \mathbf{A}_l, \tag{2.30}$$

where $\mathbf{A}_l$ is the matrix of expansion coefficients:

$$\mathbf{A}_l = \sqrt{n_{blk}} \mathbf{\Lambda}_l^{1/2} \mathbf{\Upsilon}_l^* = \mathbf{\Phi}_l^* \mathbf{W} \hat{\mathbf{Q}}_l. \tag{2.13}$$

The structure of A, dropping the l notation, is

$$\mathbf{A} = \begin{bmatrix} a_{11} & a_{12} & \cdots & a_{1n_{blk}} \\ a_{21} & a_{22} & \cdots & a_{2n_{blk}} \\ \vdots & \vdots & \ddots & \vdots \\ a_{n_{blk}1} & a_{n_{blk}2} & \cdots & a_{n_{blk}n_{blk}} \end{bmatrix}. \tag{2.14}$$

The coefficients in A cant be used to reconstruct a specific Fourier realization from the SPOD modes. Also, they can be used to expand an SPOD mode in terms of the Fourier realizations,

$$\mathbf{\Phi}_l = (1/n_{blk})\, \hat{\mathbf{Q}}_l \mathbf{A}_l^* \mathbf{\Lambda}_l^{-1}. \tag{2.31}$$

Then, the Fourier-transformed data of the k-th block can be reconstructed as

$$\hat{\mathbf{Q}}^{(k)} = \left[\left(\sum_i a_{ik} \phi^{(i)} \right)_{l=1}, \left(\sum_i a_{ik} \phi^{(i)} \right)_{l=2}, \ldots, \left(\sum_i a_{ik} \phi^{(i)} \right)_{l=n_{fft}} \right] \tag{2.32}$$

and the original data in the k-th blocks can be recovered using the inverse Fourier transform, accounting for the window weight,

$$\mathbf{q}_j^{(k)} = \frac{1}{w(j)} \mathcal{F}^{-1} \left\{ \hat{\mathbf{q}}_j^{(k)} \right\}. \tag{2.33}$$

Equivalence between SPOD and resolvent modes for uncorrelated forcing

For uncorrelated forcing, SPOD and resolvent modes are identical (Towne et al., 2018). This can be observed by writing the cross spectral density tensor at a given frequency, dropping the l notation,

$$\mathbf{S} = \mathbb{E}\left[\hat{\mathbf{q}}\hat{\mathbf{q}}^*\right]. \tag{2.34}$$

Expanding in terms of resolvent modes ψ, gains σ, and weights χ yields

$$\mathbf{S} = \sum_{j=1}^{\infty} \sum_{k=1}^{\infty} \psi_j \sigma_j \sigma_k \psi_k S_{\chi_j \chi_k}, \tag{2.35}$$

where

$$S_{\chi_j \chi_k} = \mathbb{E}\left[\chi_j \chi_k^*\right]. \tag{2.36}$$

Then,

$$\begin{aligned} \mathbf{S} &= \sum_{j=1}^{\infty} \lambda_j \phi_j \phi_j^* \\ &= \sum_{j=1}^{\infty} \sum_{k=1}^{\infty} \psi_j \sigma_j \sigma_k \psi_k S_{\chi_j \chi_k}. \end{aligned} \tag{2.37}$$

For the case where the resolvent weights are uncorrelated from one another, $S_{\chi_j \chi_k} = \mu_j \delta_{jk}$ where μ_j is a scalar. Then,

$$\begin{aligned} \mathbf{S} &= \sum_{j=1}^{\infty} \lambda_j \phi_j \phi_j^* \\ &= \sum_{j=1}^{\infty} \psi_j \psi_j^* \sigma_j^2 \mu_j. \end{aligned} \tag{2.38}$$

By orthogonality, the sets of SPOD and resolvent modes are identical when ranked in descending order by λ_j and $\sigma_j^2\mu_j$ respectively. If $\mu_j = 1$ for every j, then the ordering of the two sets is identical and $\sigma_j^2 = \lambda_j$ and $\psi_j = \phi_j$.

2.5 Datasets

Channel DNS with sand grain roughness in the fully rough regime

This dataset is extensively applied in Ch. 3, 4, and 5. The temporal average computed over 50 eddy turnover times from a DNS of a channel flow over sand grain roughness in the fully rough regime is provided by Hantsis and Piomelli, 2020. The code solves the Navier-Stokes equations using a second-order accurate central difference in space on a staggered mesh (Keating et al., 2004). A second-order accurate semi-implicit time advancement method is used, where Crank-Nicolson is used for the wall-normal diffusive terms and low-storage third-order Runge-Kutta is applied to the remaining terms. The Poisson equation is solved using an efficient Fourier transform solver. The roughness is modeled using an immersed-boundary method (IBM) based on the volume of fluid fraction (VOF) approach. The VOF φ takes on values between and including 0 and 1 in the solid and fluid regions respectively. Fractional values of φ are achieved when the surface intersects a grid cell. The form of the IBM force is given as

$$F_i(x, y, z) = -\frac{\hat{u}_i'(x, y, z)}{\Delta t}(1 - \varphi(x, y, z)), \tag{2.39}$$

where $\hat{u}_i'$ the predicted velocity, and Δt is the time step. This force is used to correct the velocity to 0 inside of the roughness.

The bottom and top roughness surfaces are mirrored across the channel centerline. The sand grain roughness consists of randomly oriented ellipsoids with semiaxes k, $1.4k$, and $2k$, where $k = 0.04\delta$ (Scotti, 2006). In the fully rough regime, $k_s \approx 1.6k$ for this geometry. The simulation is run at a constant $Re_b = 21{,}400$. The domain has dimensions $(L_x, L_y, L_z) = (6\delta, 2.064\delta, 3\delta)$, where the choice of $L_y = 2.064\delta$ instead of the conventional $L_y = 2\delta$ is made to account for blockage effects. The simulation parameters are documented in Table 2.1.

Type	Method	k/δ	Re_τ	u_τ	L_x/δ	L_y/δ	L_z/δ	N_x	N_y	N_z	Δx^+	Δy^+_{min}	Δz^+
Sand grain	DNS	0.04	1745	0.0814	6	2.064	3	1024	530	512	10.2	0.84	10.2

Table 2.1: Simulation parameters

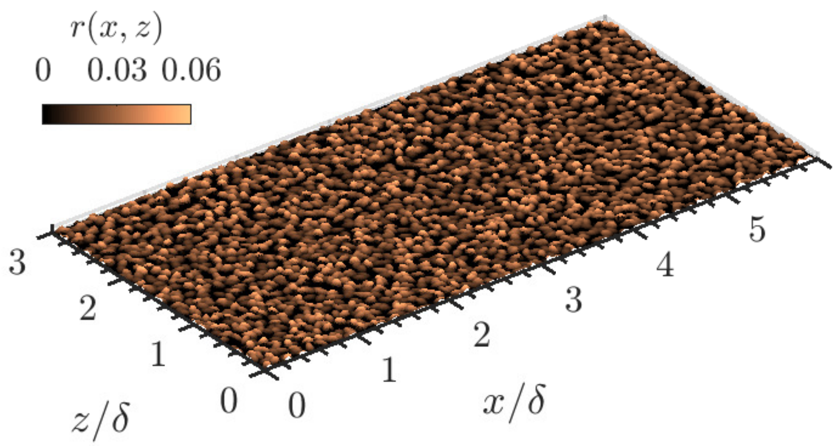

Figure 2.1: Surface roughness geometry.

2.6 Relating terms in the mean momentum balance to wake field fluctuations

In the mean momentum balance (here, velocity normalized by U_b, spatial coordinates by δ) for a smooth wall flow as depicted in Figure 2.2, the mean flow gradient is balanced by the Reynolds stress,

$$\underbrace{-\langle \Pi \rangle}_{\text{pressure gradient}} = \frac{d}{dy}\left[\underbrace{\nu \frac{d\langle \overline{u} \rangle}{dy}}_{\text{mean flow gradient}} - \underbrace{\langle \overline{u'v'} \rangle}_{\text{Reynolds stress}} \right]. \tag{2.40}$$

The mean momentum balance for rough wall flow, shown in Figure 2.3, adds addi-

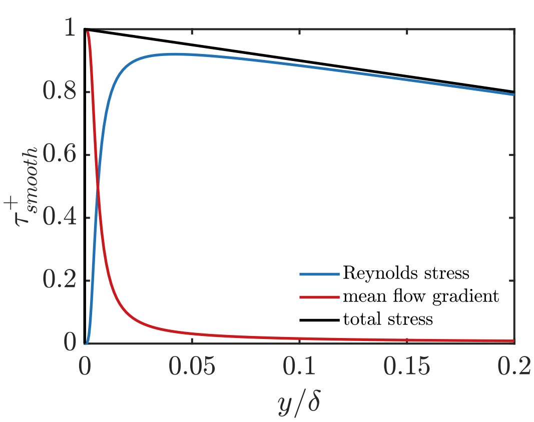

Figure 2.2: Mean momentum balance for smooth wall flow.

tional terms: pressure and viscous drag forces on the surface roughness elements, as well as a dispersive stress,

$$-\langle\Pi\rangle_s = \frac{d}{dy}\left[\nu\frac{d\langle\overline{u}\rangle_s}{dy} - \underbrace{\left\langle\overline{u'v'}\right\rangle_s}_{\text{stochastic stress}} - \underbrace{\langle\tilde{u}\tilde{v}\rangle_s}_{\text{dispersive stress}}\right] + \underbrace{f_p}_{\text{pressure force}} + \underbrace{f_v}_{\text{viscous force}}. \quad (2.41)$$

The pressure and viscous forces can be related to wake field fluctuations and the

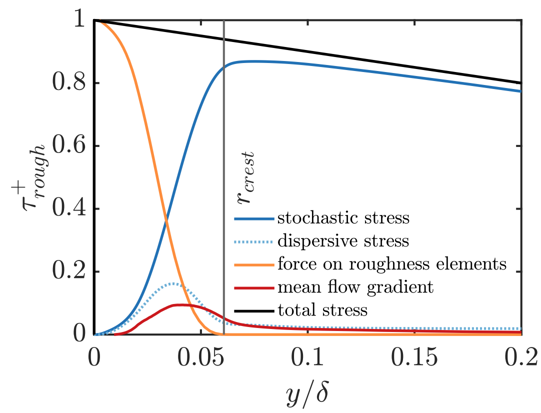

Figure 2.3: Mean momentum balance for rough wall flow for the case of sand grain roughness.

mean flow, using relations derived by taking the superficial average of the Navier-Stokes equations in a rough wall flow where the surface geometry is represented using the volume of fluid fraction (Yuan and Piomelli, 2014). The pressure force is calculated by

$$f_p = -\left\langle\frac{\partial\tilde{p}}{\partial x}\right\rangle_s, \quad (2.42)$$

and the viscous force by

$$f_v = \underbrace{\left\langle\frac{\partial}{\partial x_k}\left(\nu\frac{\partial\tilde{u}}{\partial x_k}\right)\right\rangle_s}_{f_{v_1}} \underbrace{-2\nu\frac{d\langle\overline{u}\rangle}{dy}\frac{d\Phi}{dy}}_{f_{v_2}} \underbrace{-\nu\langle\overline{u}\rangle\frac{d^2\Phi}{dy^2}}_{f_{v_3}}. \quad (2.43)$$

2.7 Relationship between the IBM force and the pressure and viscous drag forces

The sum of the viscous and pressure drag at a given location and time is equal to the streamwise body force imposed by the IBM Yuan, 2015. That body force is given by

$$f_d(x,z,t) = \int_0^1 F_1(x,y,z,t)dy \quad (2.44)$$

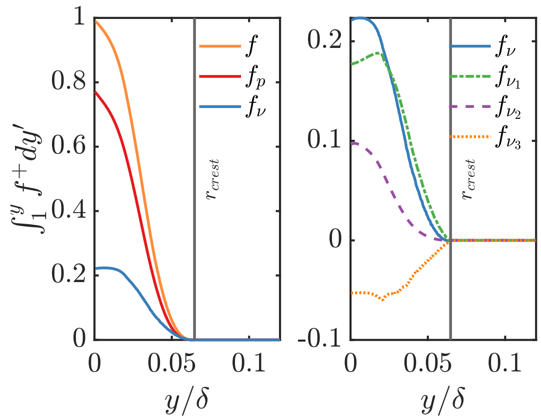

Figure 2.4: (left) The breakdown of the drag force f into the pressure f_p and viscous contributions f_v. (right) The components of the viscous drag f_v originating from the streamwise velocity wake field, f_{v_1} and two mean-dependent terms f_{v_2} and f_{v_3}.

for the channel flow considered in this thesis, given outer scaled spatial variables and velocities. Therefore,

$$\left\langle \overline{f_d} \right\rangle_{xz} = f_p + f_v. \tag{2.45}$$

Therefore, to calculate the plane- and time-averaged streamwise body force, f_p and f_v are calculated from the pseudopressure, the wake field, and the mean flow profile.

2.8 Calculation of the pressure wake field and drag forces from velocity source terms

The contributions to the time averaged pressure can be broken down into source terms in the Poisson equation.

$$\frac{\partial^2}{\partial x_i \partial x_i}\left(\langle \overline{p} \rangle + \tilde{p}\right) = -\frac{\partial^2}{\partial x_i \partial x_j}\left(\overbrace{\underbrace{\langle \overline{u_i} \rangle \tilde{u}_j + \tilde{u}_i \left\langle \overline{u_j} \right\rangle}_{\text{fast}} + \underbrace{\tilde{u}_i \tilde{u}_j}_{\text{dispersive}} + \underbrace{\overline{u_i' u_j'}}_{\text{stochastic}}}^{\text{velocity terms}}\right) - \underbrace{\frac{\partial \overline{F}_i}{\partial x_i}}_{\text{IBM force}}$$

There is a fast source that involves the interaction of the mean profile and fluctuations. There is also a source involving just the wake field fluctuations and another based on the time-averaged stochastic stress. The boundary forcing also contributes.

When the pressures associated with these quantities are plotted for the sand grain roughness in Figure 2.5, it is observed that the boundary force contribution dominates. Of the velocity terms, the major contribution comes from the dispersive source. All of the curves have the same shape, indicating that there is value to

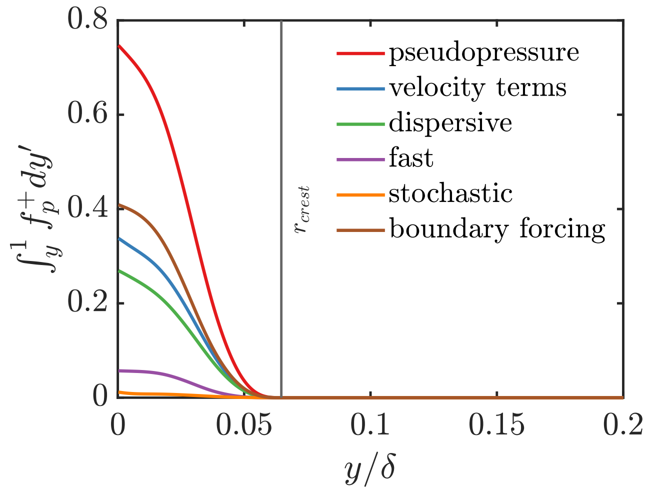

Figure 2.5: The drag force arising from the pseudopressure and contributions from the different source terms.

calculating the pressure from any known source, since it can lead to a full estimate of the force if the relative magnitude of that contribution can be predicted. The least contribution is from the stochastic source, which makes sense since the stochastic fluctuations do not have a strong presence within the roughness itself. The fast source also does not contribute much because the mean is small within the roughness.

The drag force from the pressure calculated from the dispersive source is denoted

$$f_{p_d} = -\left\langle \frac{\partial \tilde{p}_d}{\partial x} \right\rangle_s , \tag{2.46}$$

where $\tilde{p}_d = p_d - \langle \overline{p_d} \rangle$ and

$$\frac{\partial^2}{\partial x_i \partial x_i} p_d = -\frac{\partial^2}{\partial x_i \partial x_j} \left(\tilde{u}_i \tilde{u}_j \right) . \tag{2.47}$$

Chapter 3

LINEAR TRENDS IN MODAL RECONSTRUCTIONS OF WAKE FIELD TURBULENCE

3.1 Introduction

Surface roughness induces a spatial variation in the temporally averaged flow near the wall, known as the wake field. In this chapter, modal reconstructions of wake field turbulence over a sand grain roughness in channel flow are constructed using resolvent modes calculated with smooth and rough wall mean flows at the same friction Reynolds number, and weights computed to provide a best fit to the data. The modes are constructed using no-slip and no-penetration boundary conditions at the bottom and top of the domain, so that knowledge of the surface roughness geometry enters only through the weights and not into the resolvent mode basis. Inspired by the study of reduced representations of surface roughness by Mejia-Alvarez and Christensen, 2010, the effect of different truncations of the wave numbers most highly represented in the surface roughness and different numbers of retained resolvent modes are investigated to inform the choices made when calculating resolvent mode reconstructions. These reconstructions are analyzed to evaluate the efficacy of describing the wake field and forcing terms in the mean momentum balance using resolvent modes computed with and without knowledge of the rough wall mean flow. The ability of the wake field representations, in conjunction with the original mean, to represent the original roughness surface using isosurfaces of flow metrics is evaluated. Modes of the wake field and surface roughness are compared, revealing average magnitude and phase relationships which could inform modeling. Inspired by these observed trends, the validity of a linear ansatz which relates the roughness geometry and the weights is evaluated.

3.2 Wake field reconstructions using resolvent modes

Dataset

This analysis utilizes the wake field velocity, mean flow, and pressure data calculated from the temporal average of a DNS dataset of periodic channel flow with sand grain roughness on both walls at $Re_\tau = 1745$, documented in Sec. 2.5. The wake field is calculated by subtracting the intrinsic average ($\tilde{\mathbf{u}} = \overline{\mathbf{u}} - \langle \overline{\mathbf{u}} \rangle$), and averaging top and bottom. Since the wake field does not extend past the channel centerline, and the roughness surface is mirrored top and bottom, it is justifiable to treat the top and bottom temporally-averaged flows as independent instances of the same flow. The averaging operation used is

$$
\begin{aligned}
u(x,y,z) &= 0.5\left[u(x,y,z) + u(x, 2.064 - y, z)\right] \\
v(x,y,z) &= 0.5\left[v(x,y,z) - v(x, 2.064 - y, z)\right] \\
w(x,y,z) &= 0.5\left[w(x,y,z) + w(x, 2.064 - y, z)\right],
\end{aligned}
\tag{3.1}
$$

where the difference for averaging v accounts for the sign difference between the wall-normal fluctuations at the bottom and top (mirrored) surfaces.

Resolvent mode reconstructions

The wake field is Fourier-transformed in the homogeneous streamwise k_x and spanwise k_z directions. Each wake field Fourier mode, denoted $\hat{\mathbf{u}}(k_{x_r}, k_{z_r})$, is reconstructed using the sum of weighted resolvent modes computed to correspond to that wave number as documented in Table 3.1. The resolvent is computed on a 400 point Chebyshev grid defined on $y_{cheb} \in [-1, 1]$, which maps to $y/\delta \in [0, 2.064]$ by the equation

$$
\frac{y}{\delta} = \frac{2.064}{2}(y_{cheb} + 1). \tag{3.2}
$$

Base flows

The resolvent modes are calculated using two choices of base flow at $Re_\tau = 1745$; a smooth wall mean profile modeled using a Cess empirical eddy viscosity with parameters $A = 25.4$ and $\kappa = 0.426$ and a rough wall mean profile from the data, mapped to the domain using Eq. 3.2 (Cess, 1958). No-slip and no-penetration boundary conditions are enforced at the top and bottom of the domain. The choices of base flow and wave numbers considered are outlined in Table 3.1. For the case SM and RM, the wave number for which the resolvent is calculated matches the wave number of the wake field mode. For the case SMC, a choice is made to calculate the resolvent modes with a convecting velocity corresponding to the height where the dispersive stresses are expected to peak of $y/\delta = 0.04$. This choice localizes the peak amplitudes of the resolvent modes, and is investigated to determine whether this basis is more efficient at modeling the wake field data.

Choosing the rough wall mean is most consistent with the derivation of the resolvent analysis. Choosing the smooth wall mean is motivated by the desire to analyze and predict the wake field as the flow response given a surface roughness and the nominally smooth wall mean flow, without knowledge of the rough wall mean.

Designation	Description	Re_τ	Re_b	k_x	k_z	c
SM	Smooth wall mean	1745	36,940	k_{x_r}	k_{z_r}	0
RM	Rough wall mean	1745	21,400	k_{x_r}	k_{z_r}	0
SMC	Smooth wall mean + effective convecting velocity	1745	36,940	k_{x_r}	k_{z_r}	$\langle \overline{u} \rangle \, (y = 0.04)$

Table 3.1: Base flow and wave number choice for considered cases

Surface roughness wave number selection

In the study of Mejia-Alvarez and Christensen, 2010, the POD modes in a reduced representation of a surface roughness were included based on the variance captured in each POD mode. In a similar manner, the present study considers reduced representations of the surface geometry created by retaining the $N_{\mathcal{K}}$ wave numbers $\mathbf{k} = (k_{x_r}, k_{z_r})$ most strongly represented in the roughness $r(x, z)$ by mode amplitude $|\hat{r}(k_{x_r}, k_{z_r})|$, out of a maximum of $N_{total} = 2.6 \times 10^5$ wave numbers. That wave number set is denoted $\mathcal{K}$. In this analysis, only positive streamwise wave numbers are considered, while both positive and negative spanwise wave numbers are retained. The set is sorted in decreasing order of roughness mode amplitude and written as $\mathcal{K} = \left(\mathbf{k}_0, \mathbf{k}_1, \mathbf{k}_2, \cdots, \mathbf{k}_{N_{\mathcal{K}}}\right)$, where $|\hat{r}(\mathbf{k}_0)| \geq |\hat{r}(\mathbf{k}_1)| \geq \cdots \geq |\hat{r}(\mathbf{k}_{N_{\mathcal{K}}})|$.

Figure 3.1 depicts the actual appearance of the filtered surface for selected values of $N_{\mathcal{K}}$. As the number of wave numbers is increased, the filtered roughness start to more strongly resemble the original rough surface. Visually, $N_{\mathcal{K}} = 4 \times 10^4$ is nearly indistinguishable from the original surface.

To understand how these surfaces differ statistically, Figure 3.2 displays how the root-mean-squared (RMS) height k_{rms}, skewness S_{sk}, kurtosis S_{ku}, and effective slope ES statistics of the surface roughness defined in Eq. 3.5-3.8 vary with $N_{\mathcal{K}}$. The RMS height and effective slope of the roughness increase until approximately $N_{\mathcal{K}} = 10^4$ out of $N_{total} = 2.6 \times 10^5$ possible wave numbers before leveling off. The skewness is near 0 until around $N_{\mathcal{K}} = 10^3$, whereupon the skewness increases until around $N_{\mathcal{K}} = 4 \times 10^3$ before relaxing to a final value near $N_{\mathcal{K}} = 10^5$. This suggests that there is a band of wave numbers from $N_{\mathcal{K}} = 10^3 - 4 \times 10^3$ that make the major contribution to the skewness metric. Meanwhile, the kurtosis peaks before reaching $N_{\mathcal{K}} = 10^2$, and then gradually decreases to a final value near $N_{\mathcal{K}} = 10^5$. This suggests that different scales destructively interfere to determine the kurtosis of the full surface. The correlation coefficient computed between the two surfaces, calculated as

$$\mathrm{Corr}(r_f, r) = \frac{\mathrm{Cov}(r, r_f)}{\sigma_r \sigma_{r_f}}, \tag{3.3}$$

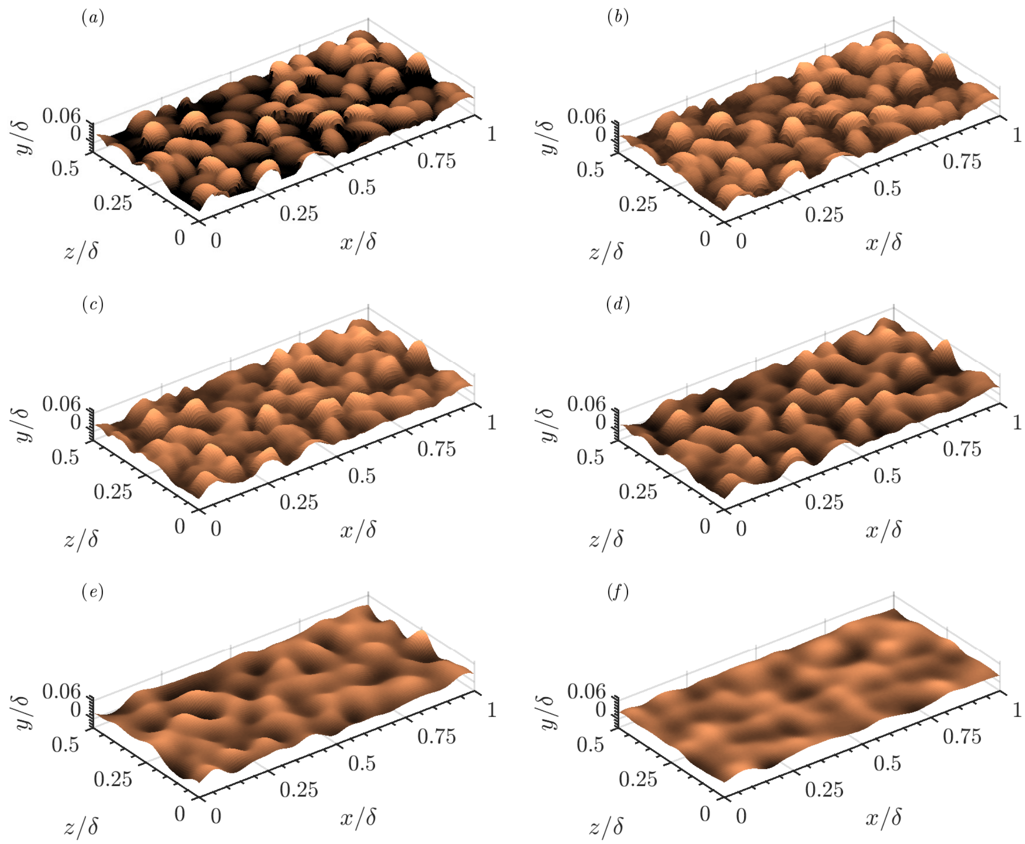

Figure 3.1: Zoomed views of (a) original roughness geometry and filtered versions where $N_{\mathcal{K}}$ is (b) 4×10^4, (c) 10^4, (d) 5×10^3, (e) 10^3, and (f) 10^2.

increases to approximately 1 at $N_{\mathcal{K}} = 10^4$. The 2-norm error, calculated as

$$\mathrm{Err}(r_f, r) = \frac{\sqrt{\langle r - r_f \rangle_{xz}}}{\sqrt{\left\langle r_f^2 \right\rangle_{xz}}}, \tag{3.4}$$

decreases to roughly 10% at $N_{\mathcal{K}} = 10^4$, but takes until $N_{\mathcal{K}} \approx N_{total}$ to achieve 1% error.

When the statistics for the filtered surface that most resembles the original surface, $N_{\mathcal{K}} = 4 \times 10^4$, are considered in Figure 3.2, it is notable that this surface falls in the region where the k^+_{rms}, S_{sk}, S_{ku} and ES statistics have either leveled off or are relaxing to the values of the unfiltered surface. The $N_{\mathcal{K}} = 10^4$ and $N_{\mathcal{K}} = 5 \times 10^3$ surfaces still visually and statistically resemble the unfiltered surface. The $N_{\mathcal{K}} = 10^3$ and $N_{\mathcal{K}} = 10^2$ surfaces do not match visually, and in particular their skewness values are not close to the original surface. The trends observed with $N_{\mathcal{K}}$ suggest that at least $N_{\mathcal{K}} = 10^4$ wave numbers are required to capture the character and statistics of the surface. Also, different different bands of wave numbers contribute to different surface statistics; major contributions to the skewness occur between $N_{\mathcal{K}} = 10^3$ and 10^4, while wave numbers less than 10^3 make contributions to the RMS height, kurtosis, and effective slope. For further analysis, cases for $N_{\mathcal{K}} = 4 \times 10^4$ and $N_{\mathcal{K}} = 10^4$ are considered.

$$k_{rms} = \sqrt{\left\langle \left(r - \langle r \rangle_{xz}\right)^2 \right\rangle_{xz}} \tag{3.5}$$

$$S_{sk} = \frac{1}{k_{rms}^3} \left\langle \left(r - \langle r \rangle_{xz}\right)^3 \right\rangle_{xz} \tag{3.6}$$

$$S_{ku} = \frac{1}{k_{rms}^4} \left\langle \left(r - \langle r \rangle_{xz}\right)^4 \right\rangle_{xz} \tag{3.7}$$

$$ES = \left\langle \left| \frac{\partial r}{\partial x} \right| \right\rangle_{xz} . \tag{3.8}$$

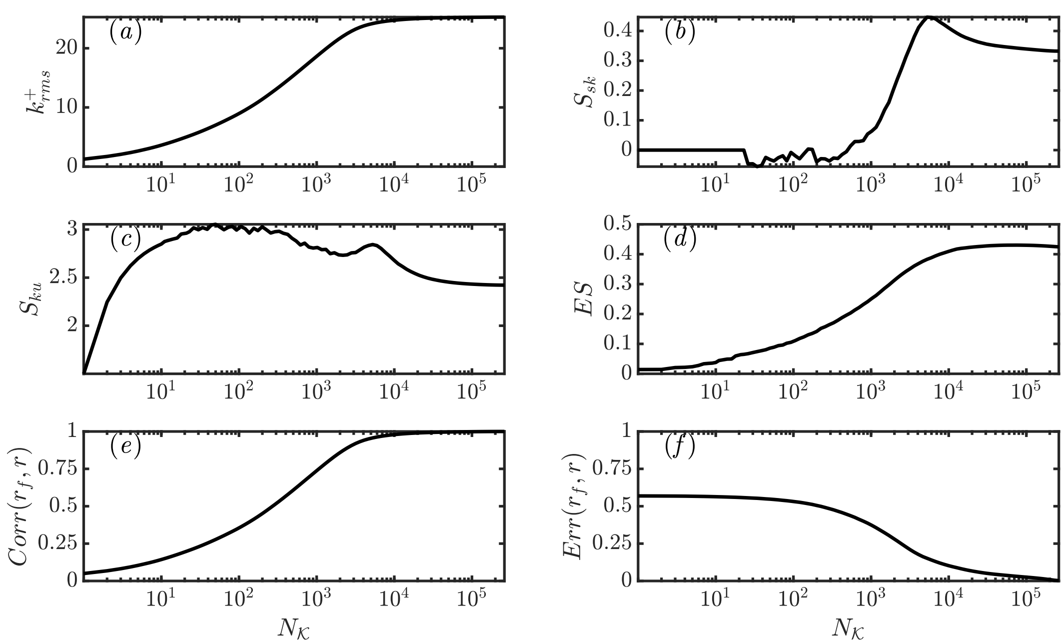

Figure 3.2: Statistics of filtered roughness as a function of number of modes retained $N_{\mathcal{K}}$. The statistics are (a) RMS height, (b) skewness, (c) kurtosis, (d) effective slope, (e) correlation coefficient between the unfiltered and filtered roughness, and (f) normalized error computed between the unfiltered and filtered roughness.

Figure 3.3 depicts the variation in k_s^+ predicted for filtered surfaces using several correlations from the literature, as well as the reference value for the unfiltered surface, $1.6k^+ = 112$. These plots suggest that the band of wave numbers between $N_{\mathcal{K}} \approx 10^3$ to 10^4 contribute strongly to the predicted k_s^+. This can be likely attributed

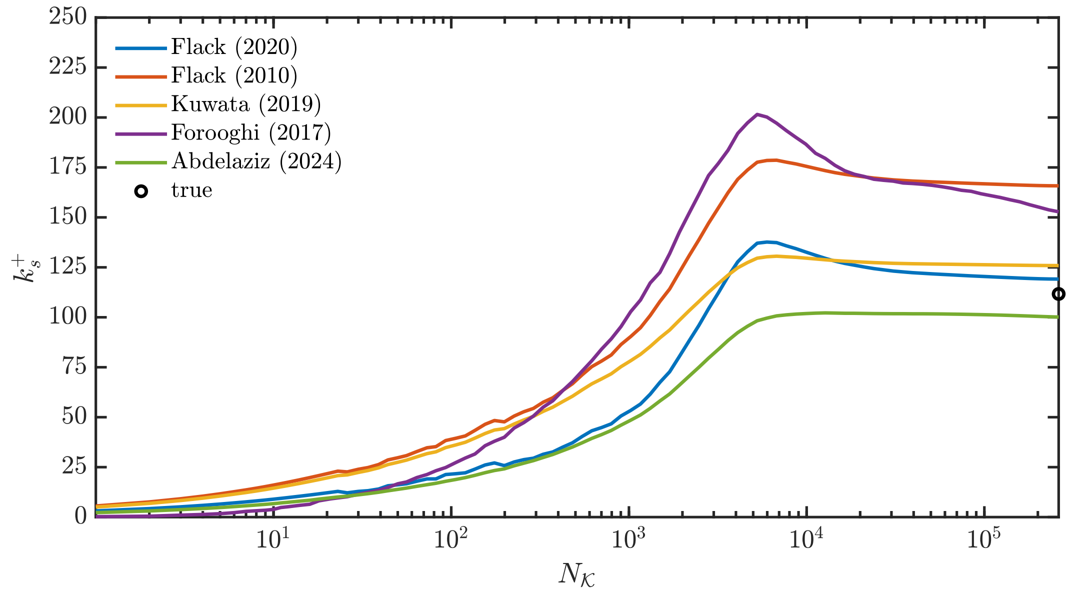

Figure 3.3: Equivalent sand grain roughness values predicted for filtered surfaces using various correlations from literature (Abdelaziz et al., 2024; Flack and Schultz, 2010; Flack, Schultz, and Barros, 2020; Forooghi et al., 2017; Kuwata and Kawaguchi, 2019).

to their functional dependence on skewness, which has principal contributions from this same band of wave numbers. The correlations of (Flack, Schultz, and Barros, 2020) and (Abdelaziz et al., 2024) are particularly interesting, since they match the reference value most closely while having different functional forms. The Flack correlation depends on RMS height and skewness, and is written as

$$\frac{k_s}{k_{rms}} = 2.48(1 + S_{sk})^{2.24}, \tag{3.9}$$

for surfaces with $S_{sk} > 0$. The Abdelaziz correlation depends on skewness, RMS height, and effective slope, and is written as

$$\frac{k_s}{k_{rms}} = -7.65 - 0.0013 S_{sk} + 2.90 ES + 9.40 e^{0.705 S_{sk} ES}. \tag{3.10}$$

Here, it seems that $N_\mathcal{K} \approx 10^4$ captures the drag-contributing scales, so the k_s^+ value predicted for the filtered surface matches that of the full surface, with the exception of the Forooghi case. In these regions, the correlations have flattened out in this regime, and adding more wave numbers does not change the predicted result.

Figure 3.4 depicts the dispersive stresses, calculated by filtering the wake field by retaining the same wave numbers as in the filtered roughness. Of particular interest is the $\langle \tilde{u}\tilde{v} \rangle$ stress due to its contribution to the mean momentum balance, and it is accurately captured with $N_{\mathcal{K}} = 10^4$. This is affected by the counteracting trends observed in the streamwise and wall normal velocities with $N_{\mathcal{K}}$; at some values of $N_{\mathcal{K}} < N_{total}$, the dispersive $\langle\tilde{u}\tilde{u}\rangle$ actually exceeds the total contribution while the $\langle\tilde{v}\tilde{v}\rangle$ stress is under-represented. It is worth noting that this does not necessarily depict the response observed in a channel flow over such a filtered surface. This analysis is simply a way to determine how many wave numbers are required to represent a statistic of interest.

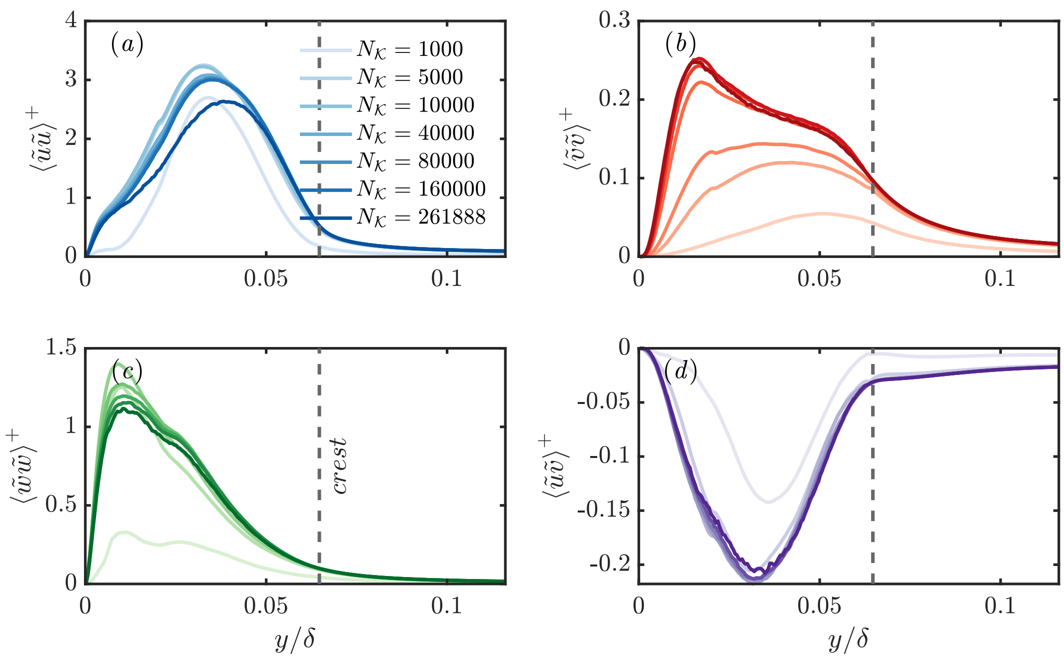

Figure 3.4: Dispersive (a) streamwise, (b) wall-normal, (c) spanwise, and (d) shear stresses for wake fields filtered to retain different $N_{\mathcal{K}}$ wave numbers.

Number of retained resolvent modes

At each wave number, the resolvent modes form a complete basis for the velocity response observed at that wave number. With increasing number of resolvent modes retained at each wave number, the quality of reconstruction should improve since the resolvent modes are orthogonal. Since it remained computationally practical to retain as many as 50 SVD modes out of 400 possible, the number of modes retained in the analysis is 50. Also, since the wake field is symmetric top and bottom, and channel resolvent modes exist in symmetric and anti-symmetric pairs, the anti-symmetric modes are disregarded in this analysis, so effectively 25 resolvent modes per wave number are used.

Determining weights

The weights for the modes are computed such that the reconstruction best matches the Fourier coefficients of the wake field with respect to the spatial inner product,

$$\mathbf{X}_{\mathbf{k}}^{\star} = \underset{\mathbf{X}_{\mathbf{k}}}{\arg\min} \, \|\hat{\mathbf{u}} - \mathbf{\Psi}_{\mathbf{k}}\mathbf{\Sigma}_{\mathbf{k}}\mathbf{X}_{\mathbf{k}}\|_{\mathbf{W}}^{2}, \tag{3.11}$$

where The reconstruction for the wake field is computed as

$$\tilde{\mathbf{u}}^{\star} = \sum_{\mathbf{k}\in\mathcal{K}} \Psi_{\mathbf{k}}\Sigma_{\mathbf{k}}\mathbf{X}_{\mathbf{k}}^{\star}. \tag{3.12}$$

The approach for reconstructing the wake field over sand grain roughness is presented graphically in Figure 3.5.

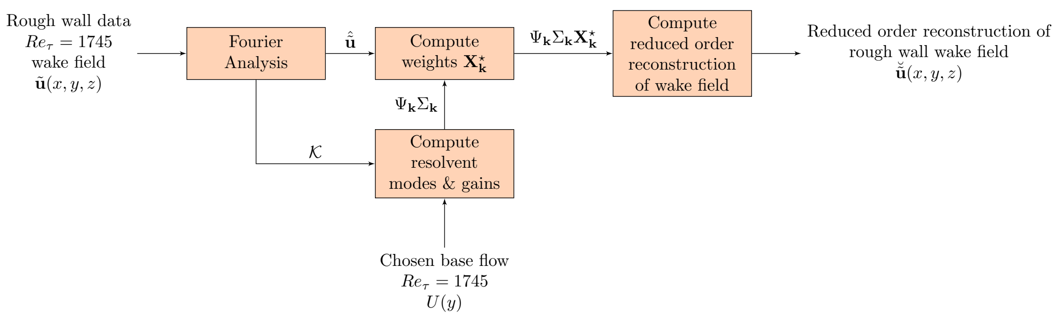

Figure 3.5: The process for computing a reduced order reconstruction of the wake field using resolvent modes given a choice of base flow and the data wake field.

3.3 Statistics, error analysis, and physical appearance of wake field reconstructions

In Figure 3.6, the velocity components of the data wake field, filtered components, and the SMC resolvent mode reconstruction are compared for $N_{\mathcal{K}} = 10{,}000$. The reconstructions reproduce the general magnitude and spatial variation in the fluctuations. The streamwise and spanwise velocities from the filtered data and resolvent mode reconstructions agree well. The resolvent mode reconstructions somewhat underestimate the magnitude of the wall-normal velocity fluctuations, and there are areas where the sign of the fluctuations differs between the filtered and resolvent mode reconstructions. An example is near $(x/\delta, z/\delta) = (0.25, 0.5)$. The resolvent mode reconstructions also capture areas of recirculation where the velocity behind roughness elements is higher near the roughness crest but lower near $y = 0$, which are important form drag-inducing features.

Correlation and error metrics are defined to measure how well the reconstructions reproduce the wake field filtered data. Figure 3.7 shows the correlation coefficient

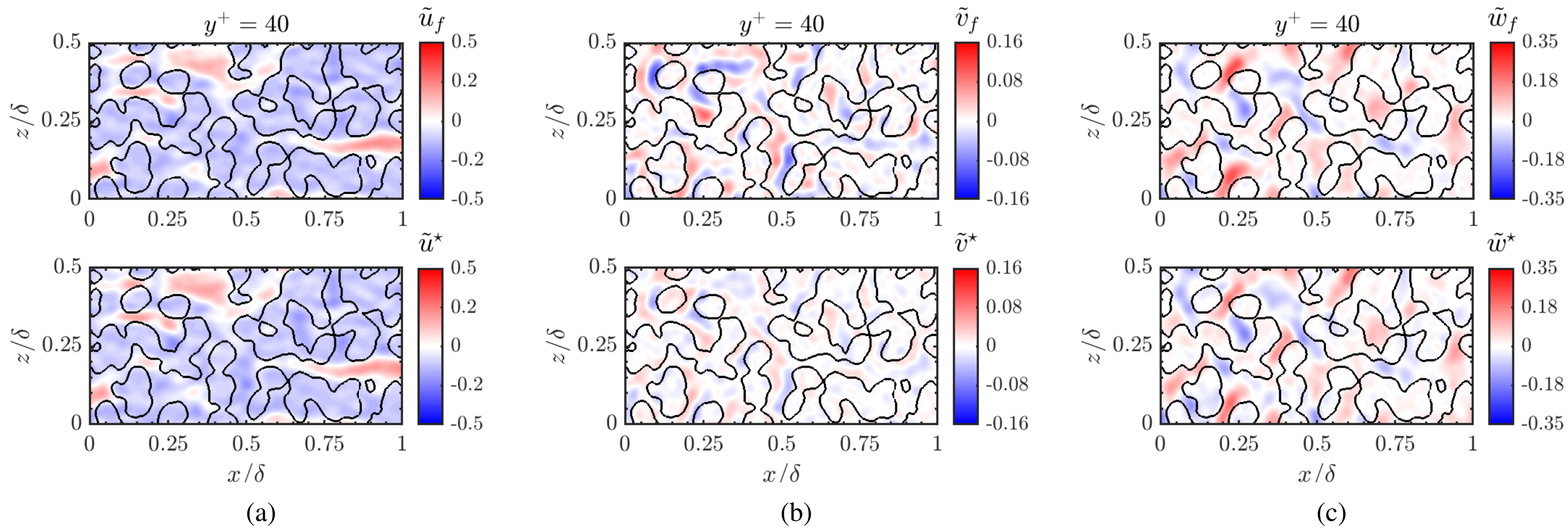

Figure 3.6: A comparison at $y^+ = 40$ between the filtered (top) and resolvent mode reconstructions (bottom) of the wake field velocity components (a) $\tilde{u}$, (b) $\tilde{v}$, and (c) $\tilde{w}$.

computed using Eq. 3.13 between the filtered wake field data and the reconstructions for the velocity components and dispersive shear stress as those quantities vary with y/δ, computed over all fluid points.

$$\text{Corr}(y; \tilde{u}_f, \tilde{u}^\star) = \frac{\text{Cov}(\tilde{u}_f(y), \tilde{u}^\star(y))}{\sigma_{\tilde{u}_f}(y)\sigma_{\tilde{u}^\star}(y)}. \tag{3.13}$$

The value of the correlation coefficient is high below the roughness crest for the SM and RM cases. The SMC case does not correlate well below $y/\delta = 0.02$, which can be attributed to the localization of these modes due to the imposed convecting velocity. The correlation coefficient decreases away from the wall for all cases.

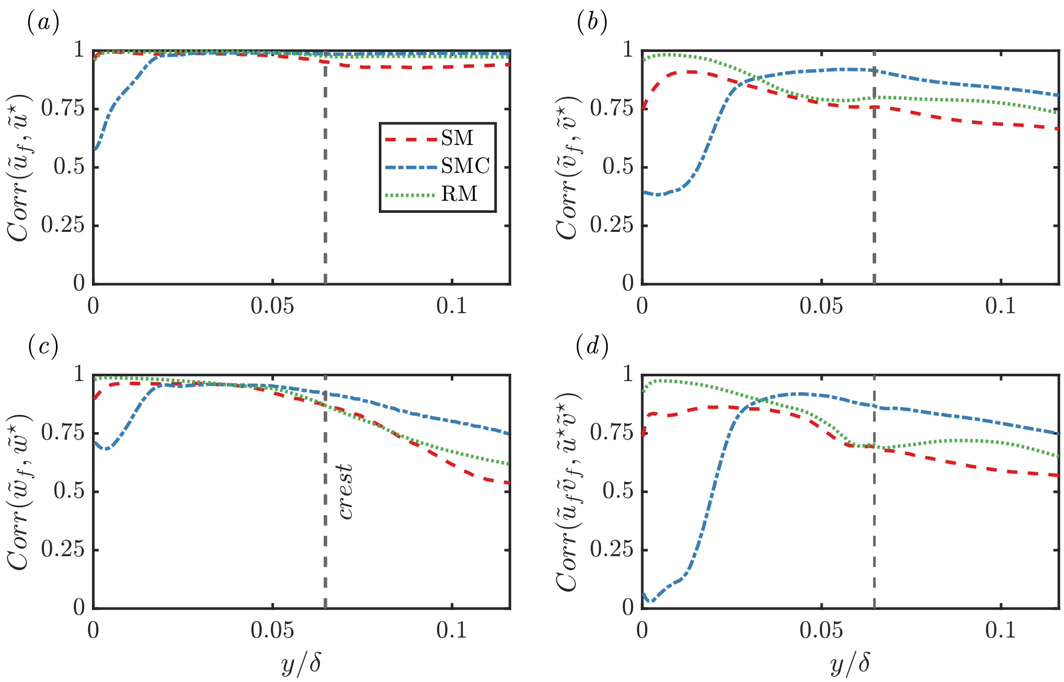

Figure 3.7: Correlation coefficient between filtered wake field and resolvent reconstructions for (a) streamwise velocity, (b) wall-normal velocity, (c) spanwise velocity, and (d) shear stress.

$$\text{Err}_{rms}(y; \tilde{u}_f, \tilde{u}^\star) = \frac{\sqrt{\left\langle \left(\tilde{u}_f(y) - \tilde{u}^\star(y)\right)^2 \right\rangle}}{\sqrt{\left\langle \tilde{u}_f^2(y) \right\rangle}}. \tag{3.14}$$

Figure 3.8 depicts the intrinsically-averaged error normalized by the root-mean-square (RMS) of the fluctuations computed using Eq. 3.14 varying with wall-normal location y/δ. It is observed that the RMS-normalized error metric is a relatively unforgiving metric, as it takes on large values between 10% to around

90% even though the reconstructions match the data well in magnitude, qualitative appearance, and by correlation coefficient. The RMS-normalized error generally takes on minimum values beneath the roughness crest before increasing above the roughness. The RMS-normalized error can be large when the RMS of the fluctuations is low, which results in high error values above the roughness crest where the dispersive stresses are small. The RMS-normalized error is relatively low for the streamwise component within the roughness crest for the SM and RM cases, but higher near $y = 0$ for the SMC case, which agrees with the trends observed in the correlation coefficient. The RMS-normalized errors for the spanwise and wall-normal velocity components are higher, since their fluctuation magnitudes are smaller.

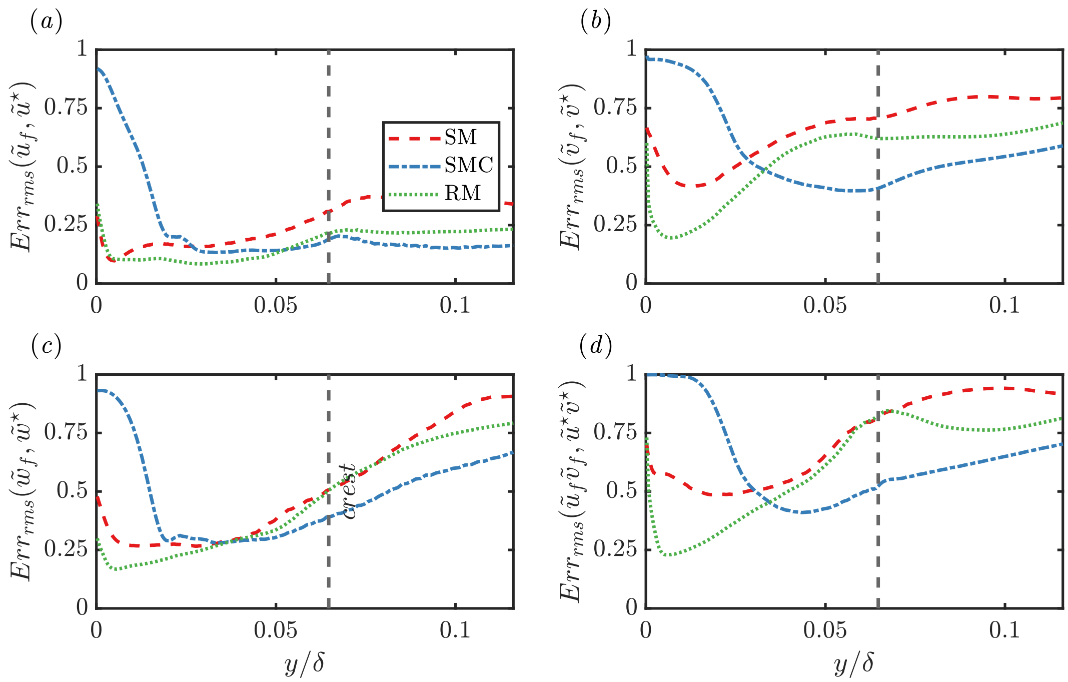

Figure 3.8: Error normalized by RMS between filtered wake field and resolvent reconstructions for (a) streamwise velocity, (b) wall-normal velocity, (c) spanwise velocity, and (d) shear stress.

$$\mathrm{Err}_{pp}(y; \tilde{u}_f, \tilde{u}^\star) = \frac{\sqrt{\left\langle \left(\tilde{u}_f(y) - \tilde{u}^\star(y)\right)^2 \right\rangle}}{\max(\tilde{u}_f(y)) - \min(\tilde{u}_f(y))}, \tag{3.15}$$

Figure 3.9 depicts the intrinsically-averaged error normalized by difference between the maximum and minimum value (peak-to-peak value) of the fluctuations, computed using Eq. 3.15. This metric appears to be more forgiving, taking on values of 10% or less, and better reflects the reasonable correlation and agreement between the data and the reconstructions. The max-min normalized error is small throughout the domain, though the SMC case shows higher error than the SM and RM cases close to $y = 0$. The max-min normalized error trends slightly upwards above the roughness crest, but far less than in the RMS-normalized error. The error observed in the SMC case is slightly higher than for the other modal bases close to $y = 0$, matching the trend observed in the RMS-normalized error and the correlation coefficent.

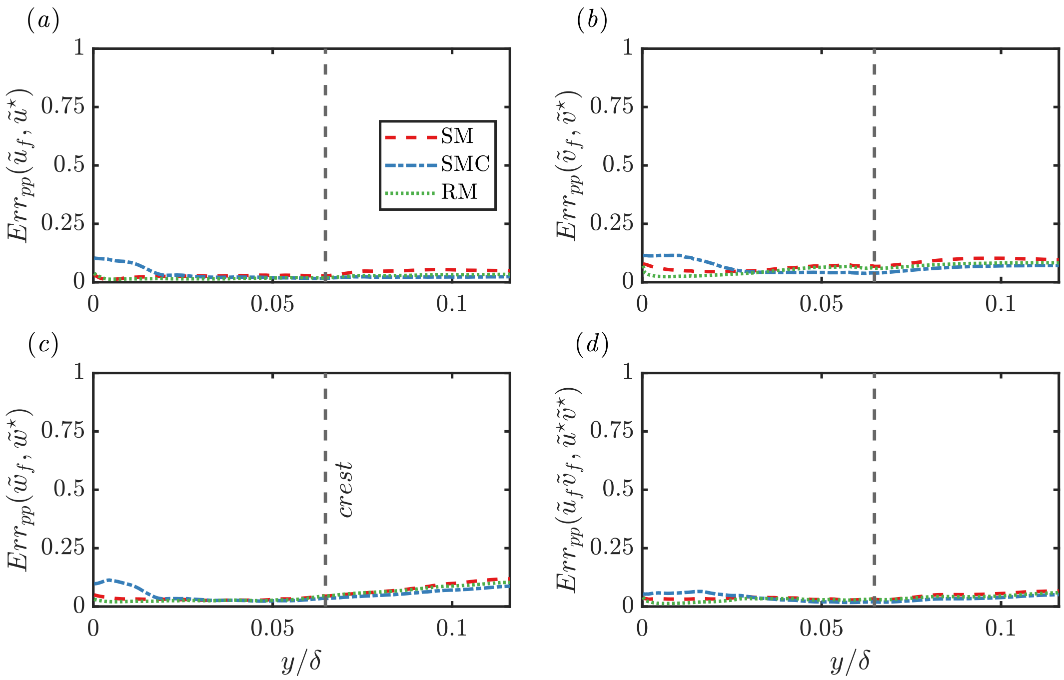

Figure 3.9: Error with max-min normalization between filtered wake field and resolvent reconstructions for (a) streamwise velocity, (b) wall-normal velocity, (c) spanwise velocity, and (d) shear stress.

Figure 3.10 depicts the statistics of the wake field reconstructions. The reconstructions reproduce the streamwise dispersive stress well in all cases. The SMC case underestimates the data close to $y = 0$ due to the localization of the modes induced by the imposed convecting velocity, in agreement with the trend observed in the correlation and error metrics. For the wall-normal dispersive stress, the best reconstruction is given by the SM modes, while the RM and SMC modes underestimate this component. For the spanwise dispersive stress, the SMC reconstruction is near 0 where the peak of the filtered stress is located, while the other reconstructions approximate the data more closely. The $\langle \tilde{u}\tilde{v} \rangle_s$ term, which contributes to the mean momentum balance, is reasonably well captured by all three reconstructions, though with a slight underestimation. This can be rationally attributed to the underestimation of the $\tilde{v}$ component since the $\tilde{u}$ component is generally reconstructed well. The relative success in capturing $\langle \tilde{u}\tilde{v} \rangle_s^+$ means that a resolvent mode basis can capture at least part of the contribution to the mean stress balance, which is promising for resolvent mode-based reduced order models.

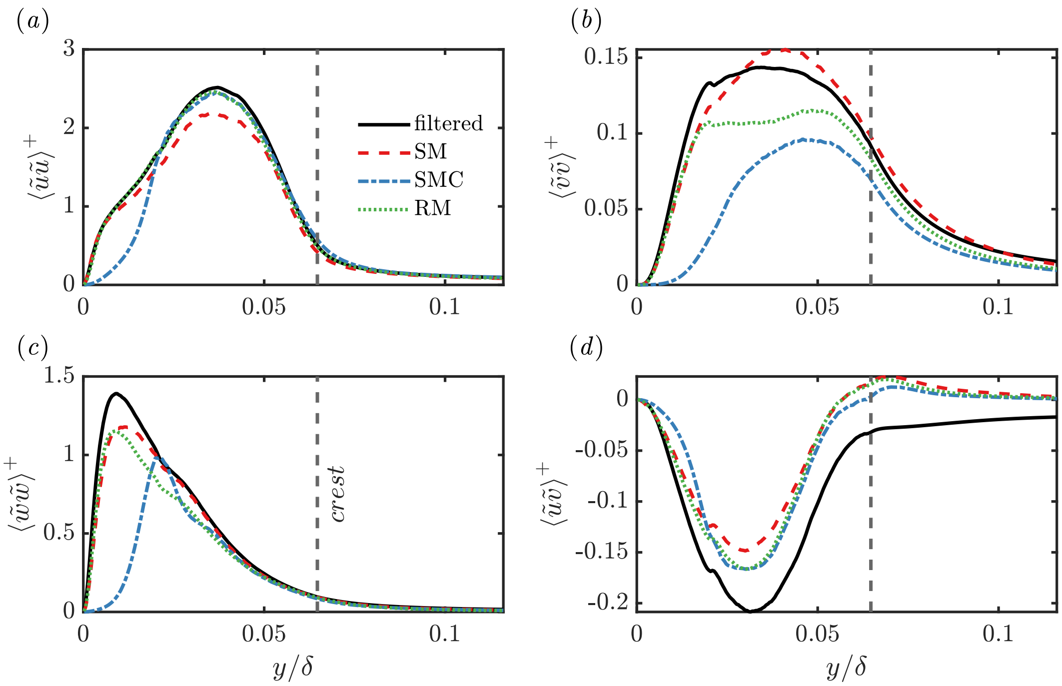

Figure 3.10: Dispersive stresses from filtered wake field and resolvent reconstructions for (a) streamwise, (b) wall-normal, (c) spanwise, and (d) shear components.

3.4 Representation of wake field forcing terms in mean momentum balance

The wake field pressure and velocity contribute strongly to the pressure and viscous drag forces in the mean momentum balance. The wall-normal integrals of the forcing components computed from the filtered data and resolvent reconstructions are compared in Figure 3.11. The forcing components originating from the dispersive source term, f_{p_d}, and the wake field u velocity, f_{ν_1} are reasonably well represented by the resolvent mode reconstructions, as calculated in Sec. 2.8 and Sec. 2.6, respectively. The peak forcing term magnitudes from the resolvent reconstructions are somewhat underestimated, but the profile shapes match reasonably well. To improve these estimations, a multiplicative factor could be employed.

3.5 Surface representations from wake field representations + the rough wall mean

The wake field reconstructions are built using resolvent modes which respect the no-slip condition at the bottom and top planes of the domain, and information about

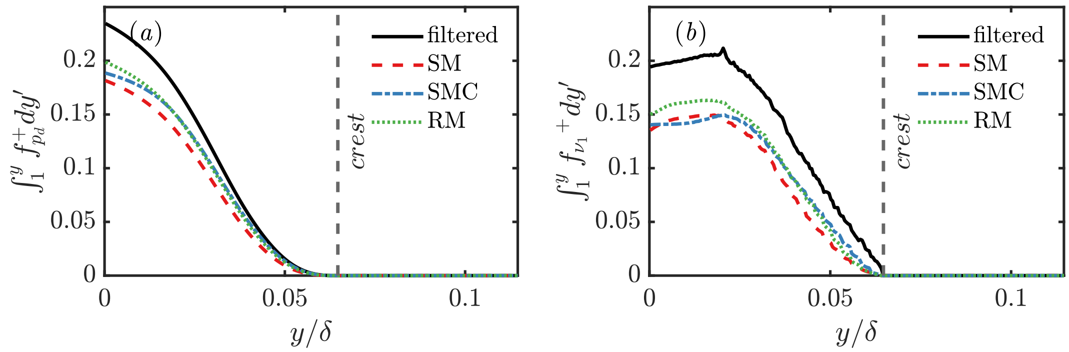

Figure 3.11: Forcing terms reproduced by the resolvent mode reconstructions of the wake field.

the surface roughness enters through the mode weights, which are determined by projecting wake field data onto the modes. The wake field has values throughout the domain, including where the volume fraction of fluid is 0, i.e. within the roughness geometry, which makes this possible. Therefore, it is important to evaluate how well the spatially varying time average reconstructions, constructed by summing the rough wall mean and the wake field reconstructions, reproduce the location of the surface geometry.

Here, three methods for defining a surface using isosurfaces of flow data metrics are defined and tested on the unfiltered temporal average for different isovalues. Then, the performance of the metrics for the $N_{\mathcal{K}} = 10{,}000$ case are tested. Finally, the performance of the isosurfaces from resolvent reconstructions is evaluated.

Isosurfaces of time averaged data

There are several physically justifiable metrics of the time averaged velocity for which isosurfaces provide reasonable estimates for the surface geometry. The most intuitive conditions are $\overline{u} = \overline{v} = \overline{w} = 0$, since there should be no-slip and no-penetration at the surface. In practice, a small positive isovalue of the metric, such as $\overline{u}^+ = \epsilon$ where $\epsilon \approx O(1)$ in inner units, works better than taking $\overline{u} = 0$, as the resulting surface geometries become more noisy. Furthermore, $\overline{v}^+ = \epsilon$ or $\overline{w}^+ = \epsilon$ do not produce meaningful results since the wall normal and spanwise-varying velocity data are highly multivalued, taking on near-zero values at possibly many y-coordinates for each (x,z) location. Taking the lowest y-coordinate corresponding to $\overline{u}^+ = 1$, by contrast, yields a meaningful result. It depicts an isosurface which rides over the top of the roughness geometry and over recirculation regions in the flow, as depicted in the side view of Figure 3.12. This analysis is similar to the blanketing layer analysis of Busse et al., 2017, which considers a higher isovalue of $\overline{u}^+ = 5$. The present study considers only lower values of ϵ which give isosurfaces that more closely approximate the roughness geometry, while Busse et al., 2017 considers the effective flow response felt slightly above the roughness.

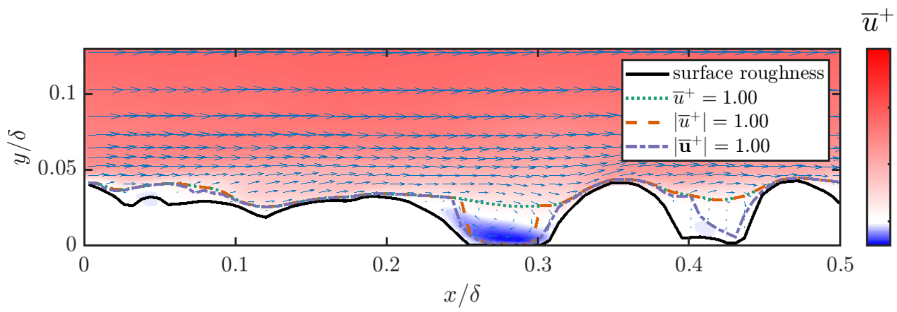

Figure 3.12: An xy slice of the temporal average and surface roughness. The quivers indicate the streamwise and spanwise flow directions. The color contour depicts where the time averaged streamwise velocity is positive (red) and negative (blue). The isosurface contour in this particular xy slice is also plotted.

The presence of recirculation regions motivates the evaluation of an alternative choice of velocity metric. While using the isosurface of $\overline{u}^+ = \epsilon$ is limited to capturing the y-coordinates where flow is moving slowly in the positive streamwise direction, using an isosurface of $|\overline{u}^+| = \epsilon$ theoretically permits the discovery of points where flow is moving slowly in the negative streamwise direction, as is possible at the bottom of recirculation bubbles, closer to the original roughness surface. This could give an isosurface that hugs the surface geometry more closely.

Another interesting metric is velocity magnitude, $|\overline{\mathbf{u}}^+| = \sqrt{u^{+^2} + v^{+^2} + w^{+^2}} = \epsilon$. This metric provides a way of incorporating the information provided by the spanwise and wall-normal velocities into a metric dominated by the streamwise velocity. The velocity magnitude also has the capacity to position an isosurface where the flow is moving weakly in the negative streamwise and negative wall-normal directions, which should be closer to the original roughness surface. This is reflected in Figure 3.12.

Figure 3.13 shows zoomed-in 3D views of the corresponding surfaces, which qualitatively supports the assertion that the $|\overline{u}^+| = 1$ and $|\overline{\mathbf{u}}^+| = 1$ surfaces reproduce the original surface roughness more closely than $|\overline{u}^+| = 1$, which renders the smoothest surface by riding over the recirculation regions.

Figure 3.14 (a-d) compares the rms height, skewness, kurtosis, and effective slope statistics for the roughness surface with the values calculated for the isosurfaces as a

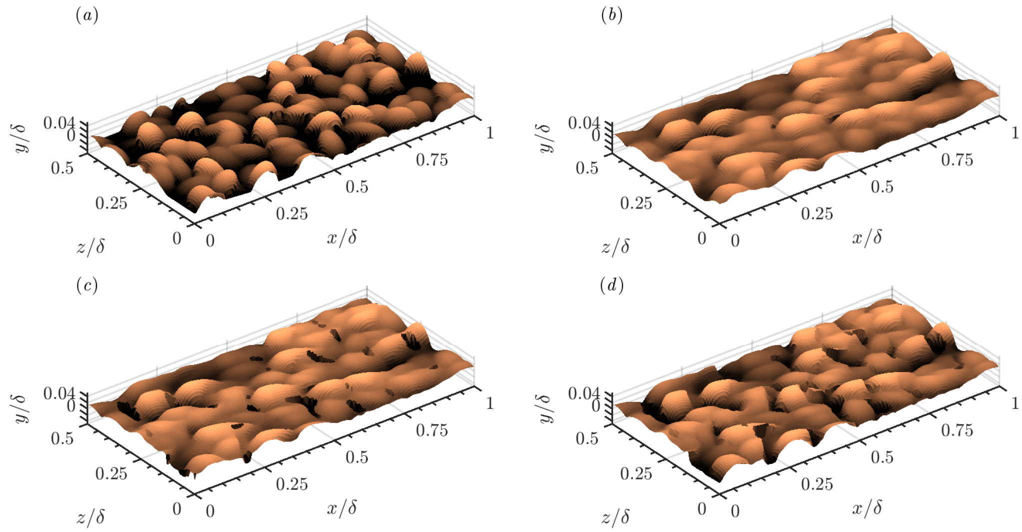

Figure 3.13: (a) Original roughness surface compared with isosurfaces of (b) $\overline{u}^+ = 1$, (c) $|\overline{u^+}| = 1$, and (d) $|\overline{\mathbf{u}}^+| = 1$.

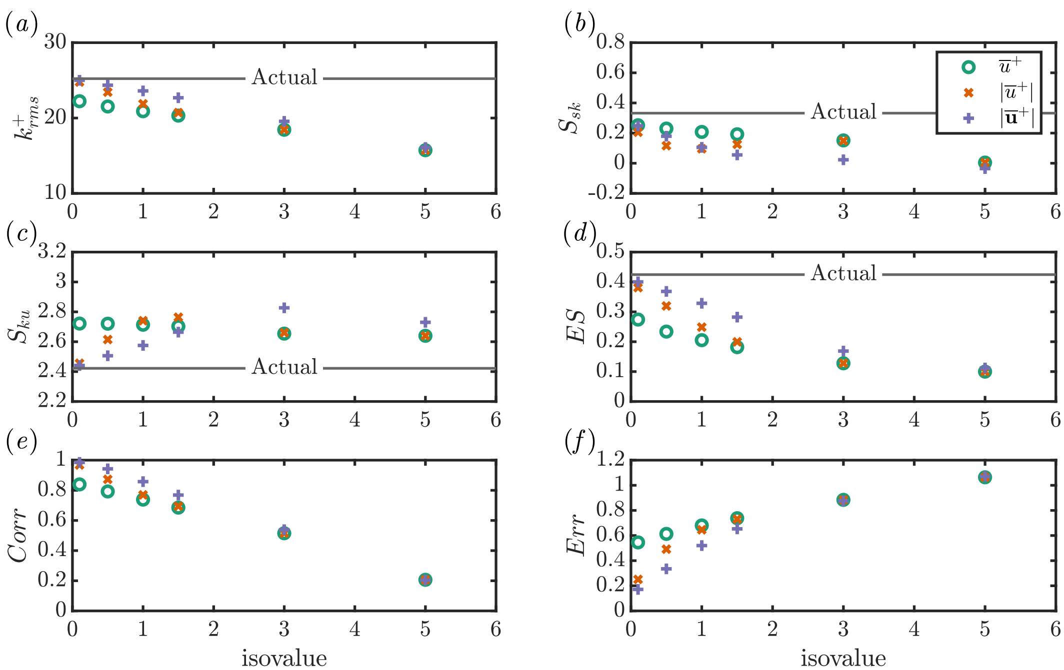

Figure 3.14: Statistics of isosurfaces of metrics from original time averaged data, compared with those of the original roughness surface. The statistics are (a) RMS height, (b) skewness, (c) kurtosis, (d) effective slope, (e) correlation coefficient between the isosurfaces and original roughness, and (f) normalized error computed between the isosurfaces and original roughness.

function of the metric isovalue. Generally, with decreasing value of the isovalue, the statistics of the isosurfaces approach the actual values from the original roughness. Isovalues as low as 0.1 in plus units generate meaningful isosurfaces. At higher values of the isovalue, the isosurfaces generally align with each other. This makes sense because there should no longer be recirculation regions at the wall-normal locations which correspond to these isovalues. Moreover, the contributions of spanwise and wall-normal velocities ought to be dominated by that of the streamwise velocity at this height as well, so the actual values of the metrics themselves should collapse. The statistics of isosurfaces calculated using the $|\overline{\mathbf{u}}^+|$ approach the statistics of the original roughness more quickly than the $|\overline{u}^+|$ metric. Both of the magnitude metrics outperform the $\overline{u}^+$ metric in this regard. The k_{rms} statistic is recovered almost exactly at low isovalues. The skewness is best represented with the $\overline{u}^+$ metric up until the lowest isovalue plotted. The kurtosis is represented less well by the $\overline{u}^+$ metric at low isovalues, while the magnitude metrics approximately recover the original surface value. It seems that the magnitude isosurfaces can capture the rms height, kurtosis, and effective slope reasonably well, while skewness is more challenging. Figure 3.14 (e-f) plots the correlation coefficient and normalized error calculated by comparing the original surface and the isosurfaces. The $|\overline{\mathbf{u}}^+|$ isosurfaces most closely correlate to the original roughness and show the least error for low isovalues. In this regard, the isosurfaces of $|\overline{u}^+|$ show a similar but slower trend towards matching the original roughness well, though the performance of the two magnitude metrics is similar at the lowest isovalue. The $\overline{u}^+$ metric does not go towards a high correlation coefficient or low error value, because it cannot account for even a small negative value as seen in recirculation regions.

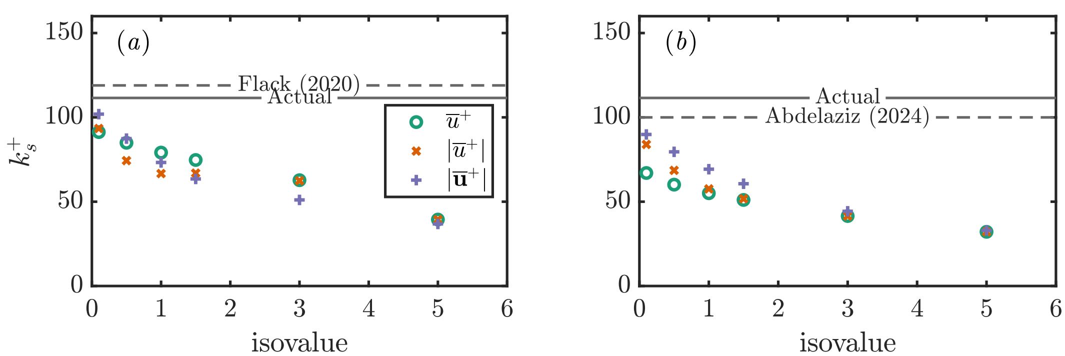

Figure 3.15: Equivalent sand grain roughness predicted for original roughness and isosurfaces of time averaged data by (a) Flack, Schultz, and Barros, 2020 and (b) Abdelaziz et al., 2024 correlations.

Figure 3.15 plots the predicted values of sand grain roughness for the surfaces using the correlations given by (Flack, Schultz, and Barros, 2020) and (Abdelaziz et al., 2024). For both correlations at the the lowest isovalue, the prediction for sand grain roughness given by the magnitude isosurfaces is higher and closer to the original surface value than that of the $\overline{u}^+$ isosurfaces. The (Abdelaziz et al., 2024) correlation seems to approach the prediction for the original surface more quickly than the (Flack, Schultz, and Barros, 2020) correlation. This is attributable to the dependence on effective slope explicitly contained in the (Abdelaziz et al., 2024) correlation, which is not captured in the (Flack, Schultz, and Barros, 2020) correlation. It is likely that in this fully rough regime, since pressure drag dominates and effective slope increases with frontal area, the effective slope is a good metric for inclusion in a drag correlation. The fact that the isosurfaces capture statistics including the effective slope as well as the equivalent sand grain roughness reasonably well raises hope that the surfaces represented by the isosurfaces could be useful surrogates for the actual roughness.

Isosurfaces of filtered time average

Then, these metrics are tested in the filtered case, to evaluate the importance of small scales in calculating the isosurfaces, and plots are shown for $N_{\mathcal{K}} = 40{,}000$. Figures 3.16 and 3.17 show side and zoomed 3D views of the surface, demonstrating that the appearance of the different isosurfaces in the filtered case is similar to that observed for the unfiltered case. The trends observed in the statistics and predicted sand grain roughness identified in the unfiltered case are mostly replicated for a sufficiently large $N_{\mathcal{K}}$. Here, $N_{\mathcal{K}} = 40{,}000$, which is still only 15% of the original wave numbers. It is further noted that the isovalues chosen cannot be as small when computing isosurfaces of the filtered data as those chosen for the unfiltered data. This indicates that the fidelity of capturing very small velocity values is not as good in the filtered case. This is demonstrated in Figure 3.18 (e-f), where it is observed that at the smallest isovalue of 0.1 in inner units, the correlation between the isosurfaces and the filtered roughness surface suddenly drops while the normalized error is near 1. Therefore, a choice is made not to plot the statistics in Figure 3.18 (a-d) for that isovalue, since they are spurious. The magnitude isosurfaces once again capture the trends in rms height, kurtosis, and effective slope reasonably well, but the issues with recovering the skewness are exacerbated.

Isosurfaces of resolvent reconstructions

Finally, the ability of the resolvent reconstructions to replicate the trends observed in the isosurfaces of metrics calculated from the filtered and original temporal averages is evaluated. The trends can be summarized by comparing the isosurfaces from the filtered data and the resolvent reconstructions.

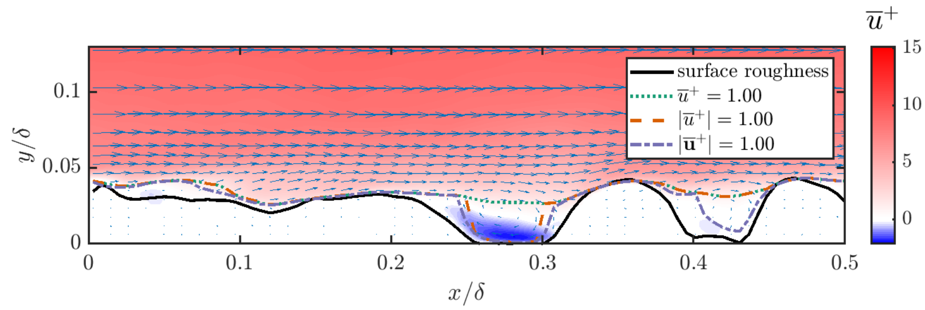

Figure 3.16: An xy slice of the filtered temporal average and filtered roughness for $N_{\mathcal{K}}$ = 40,000. The quivers indicate the streamwise and spanwise flow directions. The color contour depicts where the time averaged streamwise velocity is positive (red) and negative (blue). The isosurface contour in this particular xy slice is also plotted.

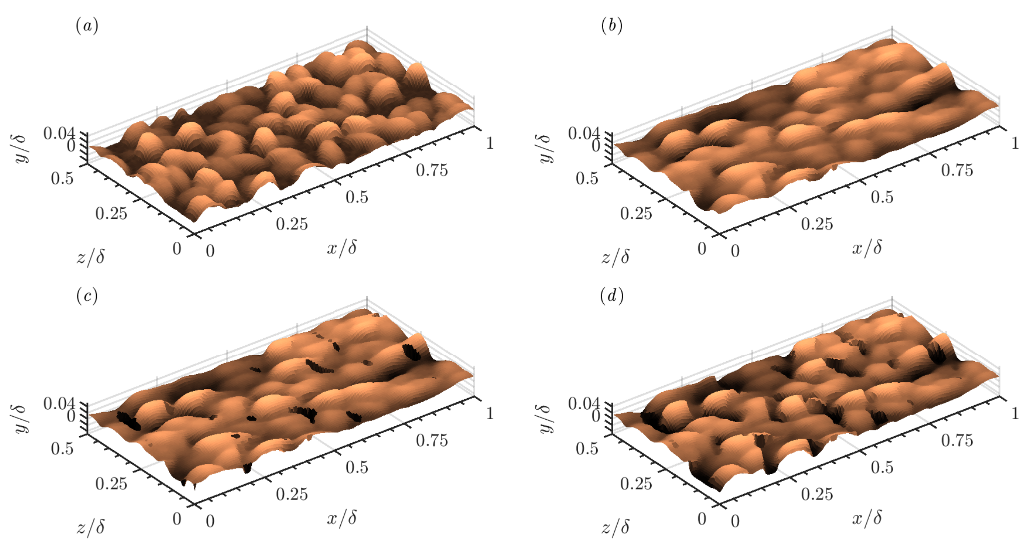

Figure 3.17: (a) Filtered roughness surface compared with isosurfaces of filtered velocity data (b) $\overline{u}^+ = 1$, (c) $\left|\overline{u}^+\right| = 1$, and (d) $\left|\overline{\mathbf{u}}^+\right| = 1$.

In Figure 3.20, the zoomed views are provided for the $\overline{u}^+ = 1$ isosurfaces. All three resolvent reconstructions reproduce the appearance of the reference isosurface from the filtered data reasonably well. In Figure 3.21, the statistics, correlation coefficient, and normalized error between the isosurfaces from the filtered data and the resolvent reconstructions are plotted. The RM statistics match those of the reference best. The SM statistics also behave well except at the lowest isovalue plotted. The SMC statistics demonstrate high error particularly at low isovalues. In Figure 3.22, the expected equivalent sand grain roughness is compared. Intuitively, the SM and RM predicted k_s^+ shows good agreement with the reference, while the SMC case shows poor agreement because of the disagreement in the statistics.

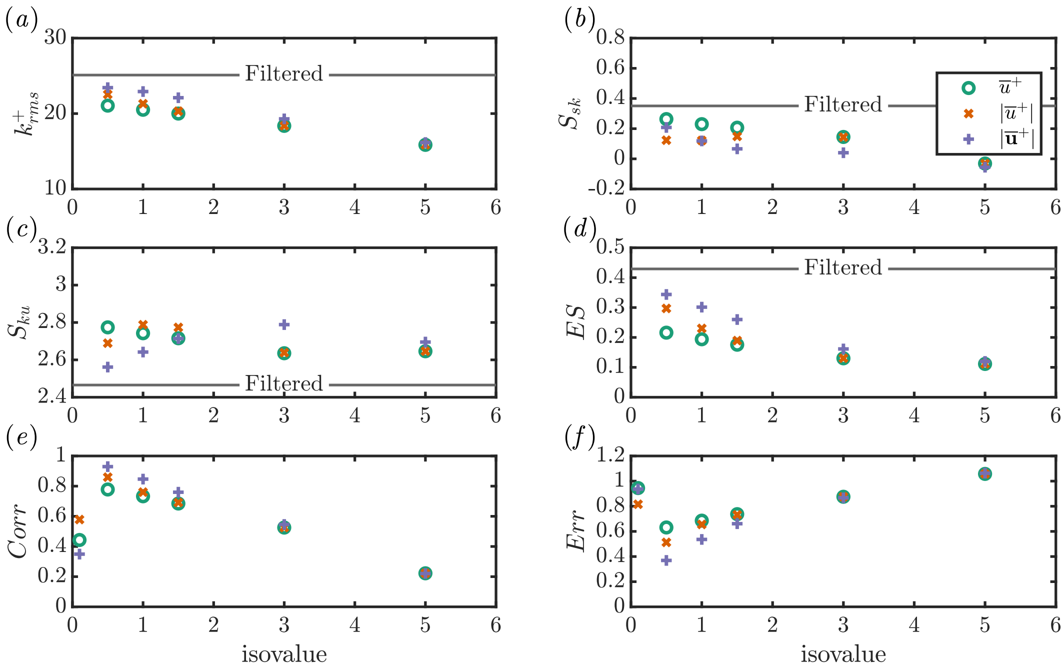

Figure 3.18: Statistics of isosurfaces of metrics calculated from filtered data, compared with that of the filtered roughness surface. The statistics are (a) RMS height, (b) skewness, (c) kurtosis, (d) effective slope, (e) correlation coefficient between the isosurfaces and filtered roughness, and (f) normalized error computed between the isosurfaces and filtered roughness.

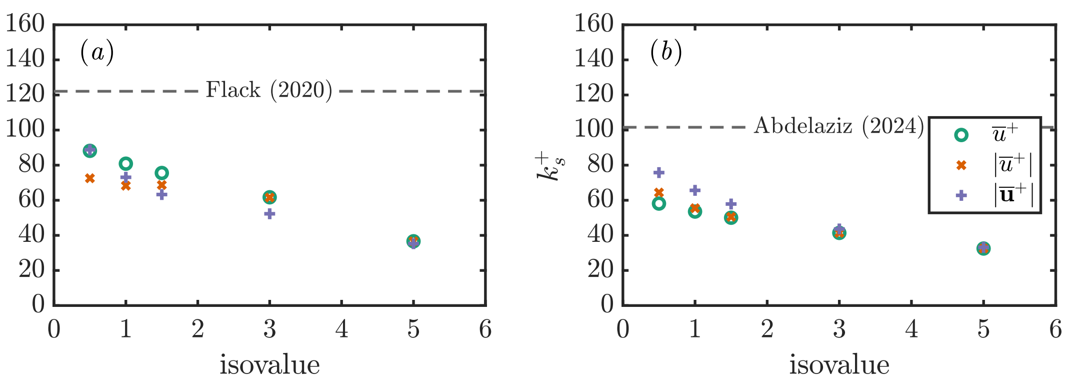

Figure 3.19: Equivalent sand grain roughness predicted for isosurfaces of filtered velocity and filtered surface by (a) Flack, Schultz, and Barros, 2020 and (b) Abdelaziz et al., 2024 correlations.

3.6 Linear trends observed in the wake field representations

In this section, the wake field velocity Fourier modes and surface roughness Fourier modes are compared, to determine if there are trends observable across wavenumber space which can inform modeling. The analysis is focused on the wavenumbers in the set K which are most represented in the roughness by magnitude. The circular mean of the phase difference between a wake field mode velocity component $\hat{u}_i(y, \mathbf{k})$ and

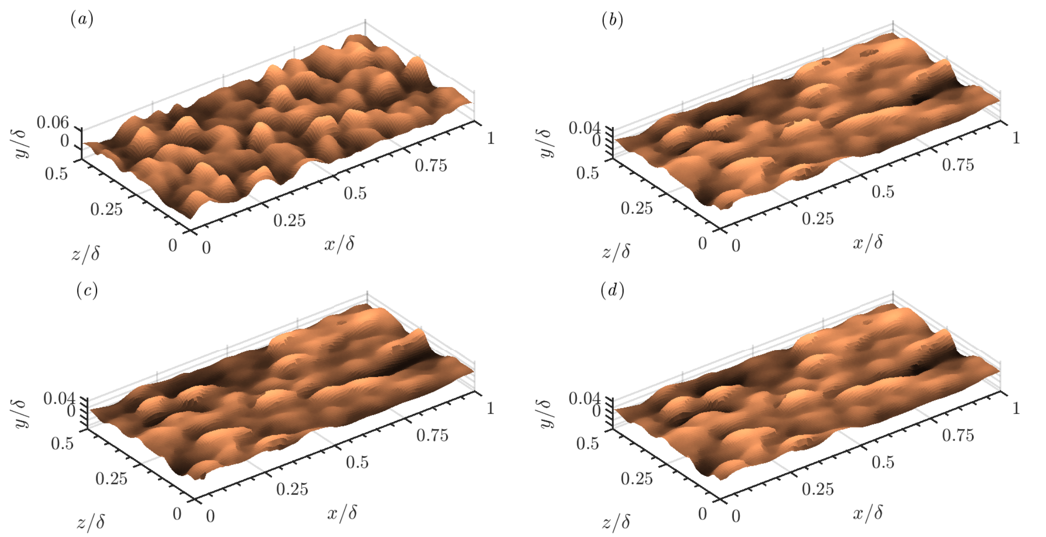

Figure 3.20: $\overline{u}^+ = 1$ isosurfaces for (a) filtered data, (b) SM reconstruction, (c) SMC reconstruction, and (d) RM reconstruction.

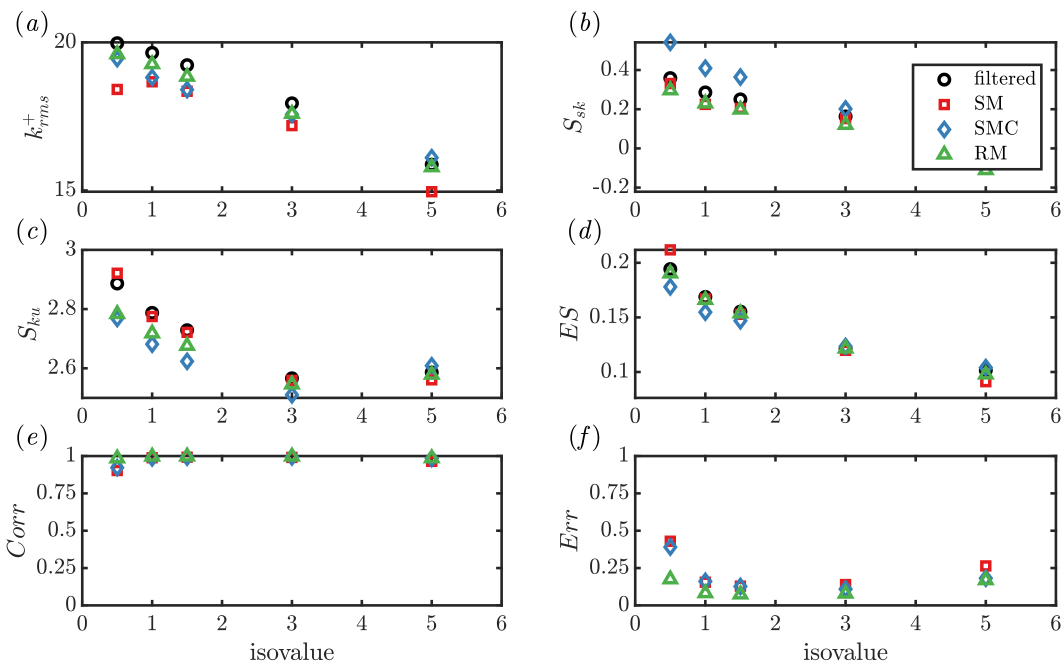

Figure 3.21: Statistics of isosurfaces of metrics calculated from the filtered data and resolvent mode reconstructions. The statistics are (a) RMS height, (b) skewness, (c) kurtosis, (d) effective slope, (e) correlation coefficient between the isosurfaces and filtered roughness, and (f) normalized error computed between the isosurfaces and filtered roughness.

the corresponding roughness mode $\hat{r}(\mathbf{k})$ is written as the argument of the resultant

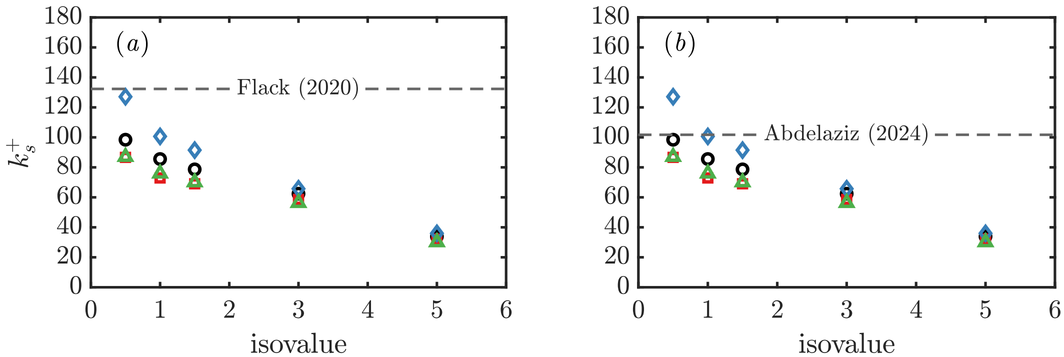

Figure 3.22: Equivalent sand grain roughness predicted for isosurfaces of the filtered data and resolvent mode reconstructions by (a) Flack, Schultz, and Barros, 2020 and (b) Abdelaziz et al., 2024 correlations.

$R = \exp\left(i\left[\angle \hat{u}_i(y;\mathbf{k}) - \angle \hat{r}(\mathbf{k})\right]\right),$

$$\Delta\theta_i(y) = \arg\left(\sum_{\mathbf{k}\in K} \exp\left(i\left[\angle \hat{u}_i(y;\mathbf{k}) - \angle \hat{r}(\mathbf{k})\right]\right)\right). \tag{3.16}$$

Its variance, defined as $1 - |R|$, is written

$$\mathrm{Var}\left[\Delta\theta_i(y)\right] = 1 - \left|\sum_{\mathbf{k}\in K} \exp\left(i\left[\angle \hat{u}_i(y;\mathbf{k}) - \angle \hat{r}(\mathbf{k})\right]\right)\right|. \tag{3.17}$$

The average magnitude ratio between $|\hat{u}_i(y;\mathbf{k})|$ and $\hat{r}(\mathbf{k})$ is defined as

$$M_i(y) = \frac{1}{N_K}\sum_{\mathbf{k}\in K}\frac{|\hat{u}_i(y;\mathbf{k})|}{|\hat{r}(\mathbf{k})|}. \tag{3.18}$$

In Figure 3.23(a), $\Delta\theta_i$ and its standard deviation are plotted as functions of y. The streamwise velocity mode is out of phase with the roughness mode below the roughness crest, and approximately in phase above the roughness crest. The physical analogy is having a faster streamwise velocity fluctuation between bumps. The wall-normal velocity switches between being roughly $-\pi/2$ and $\pi/2$ out of phase with the roughness at $y^+ \approx 60$. This is akin to a slight upwards velocity fluctuation upstream of a bump, and a slight negative velocity fluctuation downstream of the bump. The spanwise velocity is in phase if $\mathbf{k}$ has positive spanwise wavenumber k_z, and out of phase if k_z is negative. Essentially, if a (k_x, k_z) wave is canted towards the first quadrant on a (x, z) grid, then the spanwise velocity wave is positive, and if the wave is canted towards the fourth quadrant then the spanwise velocity wave is positive.

In Figure 3.23(b), M_i and its interquartile range are plotted. Once again, distinct mean trends are detectable, although the interquartile range is large particularly in the case of the streamwise component.

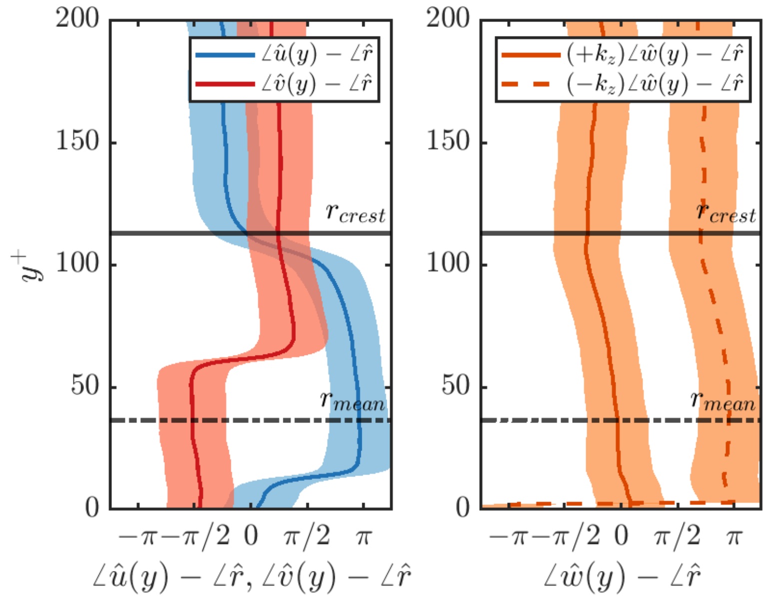

(a)

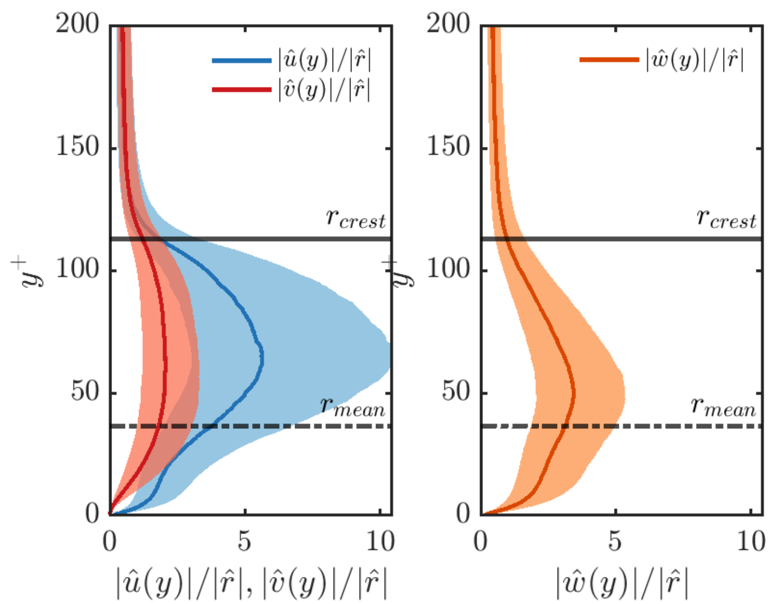

(b)

Figure 3.23: (a) Phase of $\hat{u}$, $\hat{v}$, $\hat{w}$ relative to $\hat{r}$, $N_{\mathcal{K}}$ = 10,000 (4%). (b) Magnitude of $\hat{u}$, $\hat{v}$, $\hat{w}$ relative to $\hat{r}$.

The existence of these linear trends, which seem to hold on a wavenumber-by-wavenumber basis in a multiscale roughness geometry, suggests that a linear modeling framework for the wake field is potentially useful.

3.7 Proposed modeling methodology using resolvent modes and its challenges

The average linear relationships identified between the roughness and wake field velocity modes suggest that a linear ansatz for modeling the wake field fluctuations could be useful. One possible linear model for the wake field fluctuations is formed as

$$u_i(y) = \sum_{\mathbf{k}\in K} M_i \hat{r}(\mathbf{k}) \exp\left(i\Delta\theta_i\right). \tag{3.19}$$

This model form assumes that the average linear relationships are sufficient to give predictions of the wake field mode shape (magnitude and wall-normal phase variation) and phase alignment (phase with respect to a reference) when applied across the included wavenumbers.

The resulting wake field from this model form is not necessarily physical; it is not divergence-free by construction. An improvement to the modeling methodology is made by determining the mode shape using the sum of weighted resolvent modes, which is divergence-free by construction. Here, a linear ansatz is developed that permits the building of a model using resolvent modes, leveraging the interpretation that the resolvent mode weights contain the influence of the roughness.

For each wave number, the resolvent mode gains and singular values are written as linearly related to the roughness through a complex coefficient ξ_j, as in

$$\begin{bmatrix} \sigma_1\chi_1 \\ \vdots \\ \sigma_N\chi_N \end{bmatrix} = \begin{bmatrix} \xi_1 \\ \vdots \\ \xi_N \end{bmatrix} \hat{r}, \tag{3.20}$$

then the wake field can be represented as

$$\begin{bmatrix} \hat{\hat{u}} \\ \hat{\hat{p}}_{fast} \end{bmatrix} = \sum_{j=1}^{N} \psi_j \xi_j \hat{r}. \tag{3.21}$$

This linear ansatz reduces the problem of modeling the wake field using resolvent modes to modeling ξ_j, which captures how strongly each resolvent mode is forced by the roughness and the phase alignment of the modes with respect to the roughness modes.

To investigate this modeling methodology, the values of ξ_j are calculated from the best fit weights determined for the resolvent mode reconstructions,

$$\xi_j^\star = \frac{\sigma_j \chi_j^\star}{\hat{r}}, \tag{3.22}$$

and the $|\hat{r}|$-weighted average computed over the wave number set $\mathcal{K}$ is used for the model, $\xi_j^\odot$. The weighted average and standard deviations of the magnitude and phase of $\xi_j^\odot$ for each resolvent mode is plotted in Figure 3.24 for the RM case. These plots show a promising strong collapse of the magnitude with small standard deviation, but relatively large standard deviation for the phase, which poses issues for modeling. Also, while the trend in the magnitudes with j appears to be a curve which could be modeled, there is not a clearly discernable trend in the phase with j. To investigate the linear ansatz in the case of the smooth wall mean, Figure 3.25

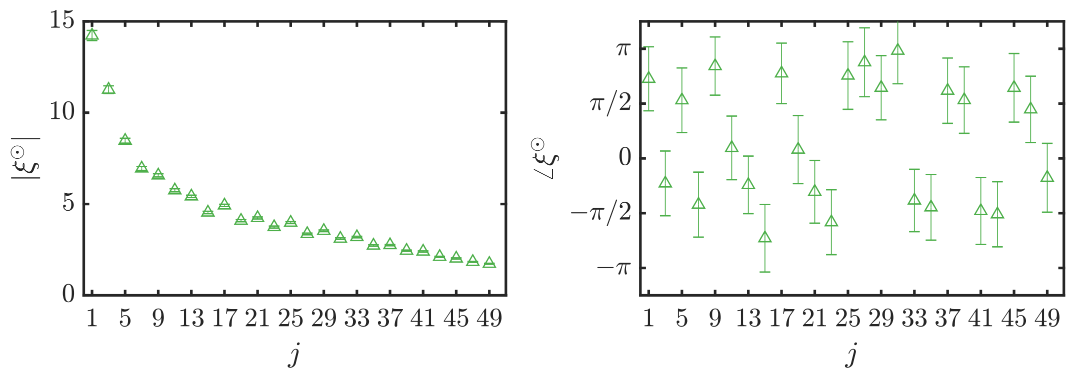

Figure 3.24: $|\hat{r}|$-weighted mean and standard deviation of ξ values obtained from $\chi^\star$ fit to data for RM case.

shows the trend in ξ_j for the SM case. In this case, the magnitude and phase are scattered and do not necessarily show an organized trend. For the SM and RM cases, it might be possible to model the phase by considering alternating values of $\pm\pi/2$, though this is not explored in the present work. This suggests that to reconstruct wake field modes, additional resolvent modes act in a constructive and destructive manner, leveraging the opposing phase angles to generate the correct mode shape. It is also noted that while the magnitude of ξ_j in the RM case approaches 0 quickly with increasing j, that favorable trend is not as strong in the SM case. In the SMC case, the magnitude and phase of ξ_j appears more organized and amenable to modeling than those of the RM or SM cases, with the magnitude going to 0 with increasing j and a smaller alternating trend in the phase. This is due to the wall-normal localization of the SMC modes, which is artificially imposed by the effective convecting velocity. This wall-normal localization reduces the need for resolvent

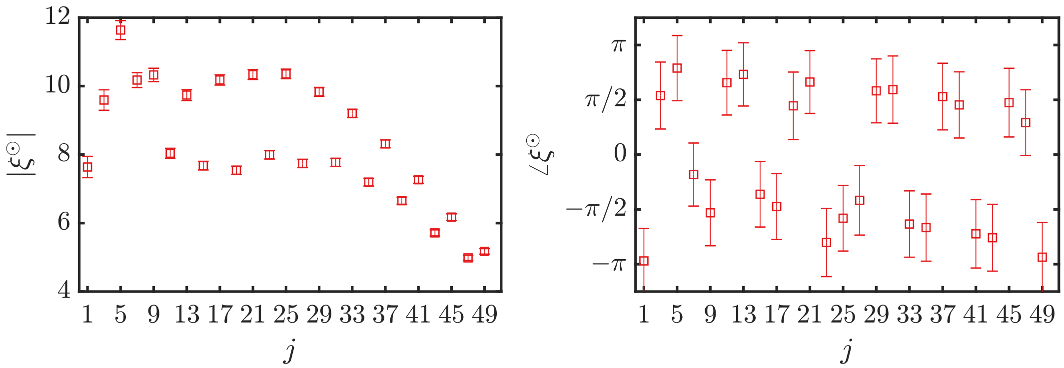

Figure 3.25: $|\hat{r}|$-weighted mean and standard deviation of ξ values obtained from $\chi^{\star}$ fit to data for SM case.

modes to add destructively and constructively when optimally reconstructing the wake field modes. This highlights that the SMC basis may be desirable from a modeling perspective, even though the SMC basis does not necessarily provide a superior reconstruction to the SM and RM cases.

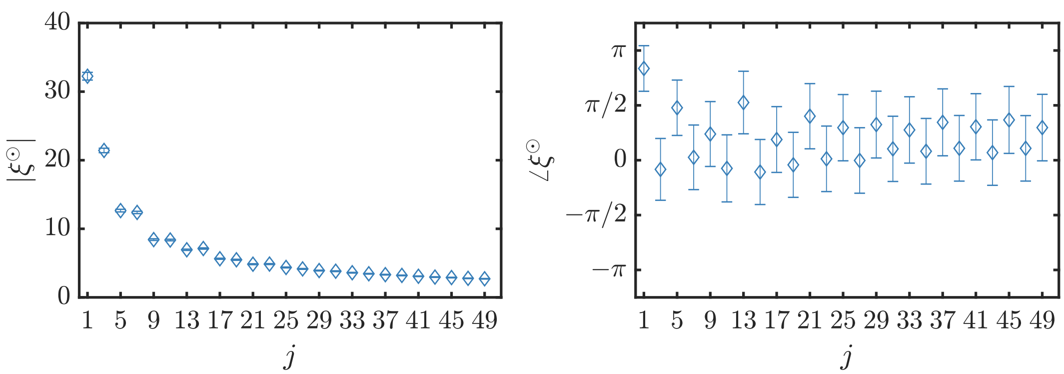

Figure 3.26: $|\hat{r}|$-weighted mean and standard deviation of ξ values obtained from $\chi^{\star}$ fit to data for SMC case.

For each of these cases, the model based on $\xi^{\odot}$ values is calculated to evaluate whether these trends are sufficient to model the wake field. The correlation coefficient between the filtered and modeled wake field is plotted in Figure 3.27. The correlation coefficient always has a low value of less than 0.4, indicating that the modeled wake field does not correlate well with the filtered wake field at any wall-normal location. Figure 3.28 plots the RMS-normalized error, which is on the order of 100% between the modeled and filtered wake fields, suggesting that the agreement between the model and data is poor. Figure 3.29 plots the max-min normalized error. This error metric takes on values of 5% to 30%, but generally exceeds 10%. This is notable because the best fit reconstructions from Sec. have max-min normalized error values of less than 10%, suggesting that values for this

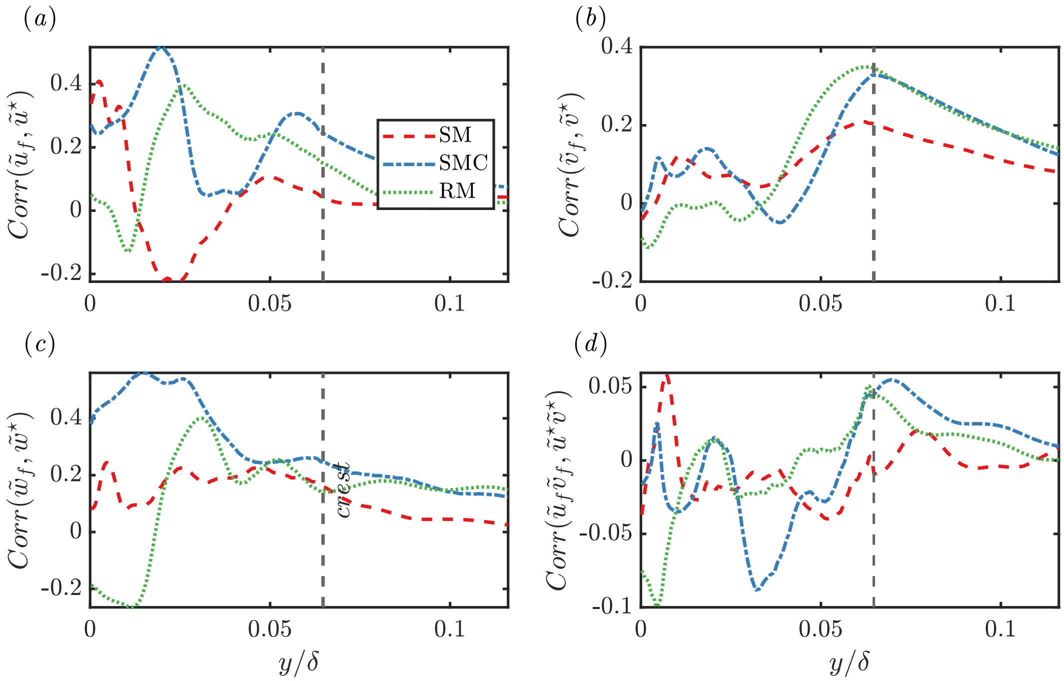

Figure 3.27: Correlation coefficient between the filtered and modeled wake fields for the (a) streamwise velocity, (b) wall-normal velocity, (c) spanwise velocity, and (d) shear stress.

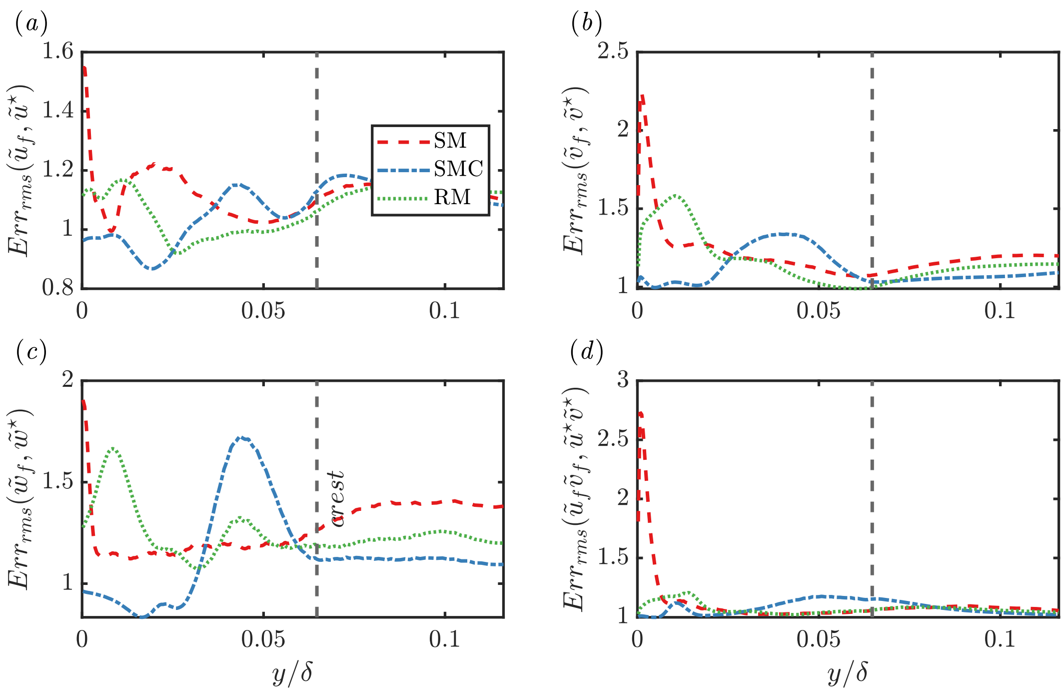

Figure 3.28: Error normalized by RMS between the modeled and filtered wake fields for the (a) streamwise velocity, (b) wall-normal velocity, (c) spanwise velocity, and (d) shear stress.

error metric of above 10% suggest poor agreement. Figure 3.30 shows that the

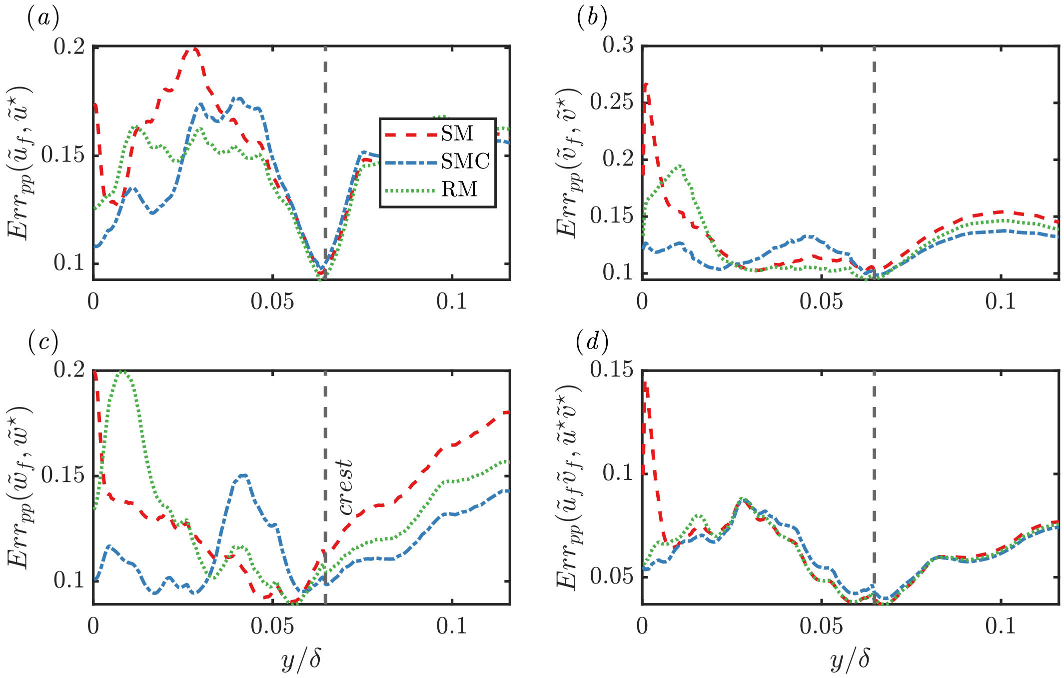

Figure 3.29: Error with max-min normalization between the modeled and filtered wake fields for the (a) streamwise velocity, (b) wall-normal velocity, (c) spanwise velocity, and (d) shear stress.

wake field statistics are generally not well captured by the model. The models for the wall-normal dispersive stress show some qualitative agreement, with the SMC model qualitatively capturing the shape reasonably well. However, the magnitude is underestimated. The agreement for the streamwise velocity component is poor, so the shear dispersive stress is not predicted well. The shape of the spanwise stress is somewhat predicted by the SM and RM models, and the peak agreement is reasonable for the RM model. The SMC model does not perform well for the spanwise stress. Overall, while the modeling framework is logical and produces a divergence-free field by construction, a successful model closure for generating usable predictions of fluctuations and dispersive stresses has not been achieved here. One challenging aspect is that the model depends on training a large number of ξ_j parameters. While mean trends in the ξ_j parameters across wave number space are easily recognized, using average values of the ξ_j parameters proves insufficient in this analysis to model the fluctuations effectively. It is possible that there are trends across wave number space which could be incorporated to improve the model form. To successfully close this modeling framework, improvements to the modeling method for the weights must be found from the data analysis. It is also unclear

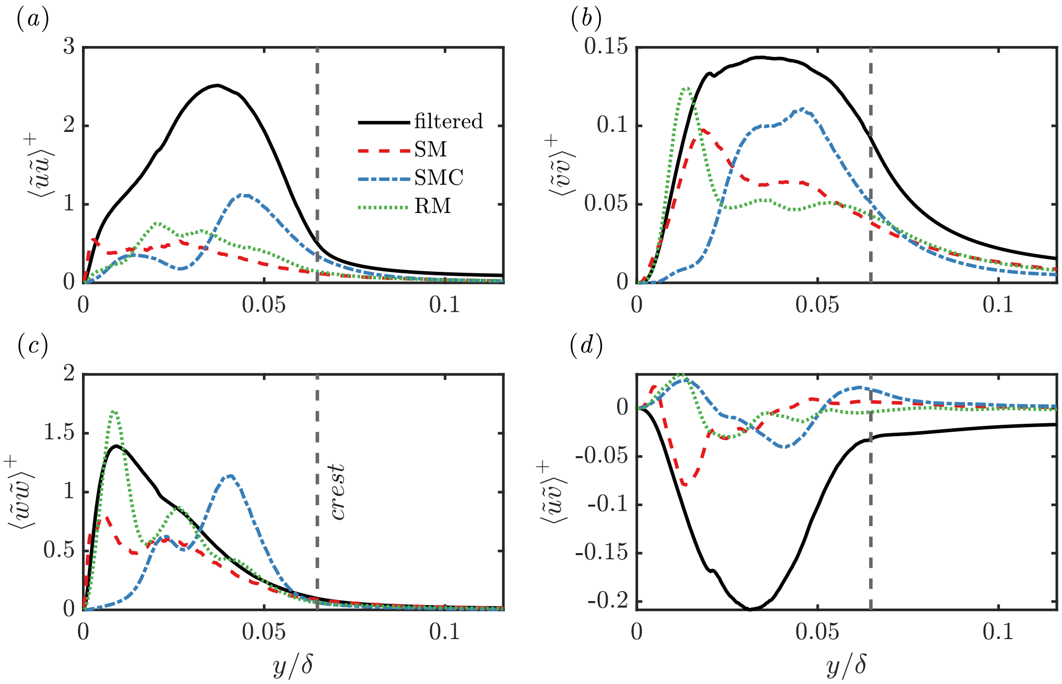

Figure 3.30: Dispersive stresses of the modeled and filtered wake fields.

how trends learned from analysis of the sand grain roughness hold in the turbulent flows over other surface geometries. Therefore, it is unclear how to improve this modeling approach to predict wake field and dispersive fluctuations over other surface geometries.

3.8 Summary

In this chapter, modal reconstructions of the wake field using resolvent modes are analyzed for their capacity to serve as surrogates for the original wake field and roughness geometry. The resolvent mode bases (SM, SMC, and RM) are constructed using smooth and rough wall mean profiles, in which the effect of the roughness enters only through the mode weights. All three reconstructions reproduce the general appearance of the wake field velocities, dispersive statistics of velocity and pressure, and the shapes of the forcing terms in the mean momentum equation. When the rough wall mean is added to the reconstructions, isosurfaces of metrics computed from the resulting temporal average reconstruction are shown to be similar to the original roughness. These results demonstrate that a resolvent mode representation built using modes calculated with standard boundary conditions and a different mean than in the original data, with information about the roughness entering through the weights, can still reproduce information about the original rough surface.

Comparison of the wake field and surface roughness modes reveals a phase alignment in the flow induced by the roughness. This demonstrates that linear trends exist in the data which can inform modeling approaches. Inspired by this, a linear ansatz is taken to relate the resolvent mode weights and the roughness through a complex coefficient $\xi_j^{\odot}$ learned from data. The trends in $\xi_j^{\odot}$ are analyzed and used to evaluate the resulting modeling framework. However, the wake field model does not provide usable estimates of wake field fluctuations and dispersive stresses, indicating that the average trends identified from the data are insufficient to model the flow response.

The difficulties associated with this modeling approach suggest that an alternative to data-driven methods for analyzing the weights is desirable, which is the subject of the next chapter.

Chapter 4

REDUCED ORDER MODEL FOR ROUGHNESS SUBLAYER FLUCTUATIONS OVER MULTISCALE ROUGHNESS USING RESOLVENT ANALYSIS

4.1 Introduction

In this chapter, a reduced order modeling method for roughness sublayer turbulent fluctuations over engineering-relevant multiscale roughness is formulated using resolvent analysis with volume penalization (RAVP). The model accepts an inner-scaled mean flow profile and a scan of the roughness geometry as inputs, and outputs quantitatively useful predictions of spatiotemporal fluctuations and dispersive stresses. The key innovations in this development are a drag-scaled approach for determining the magnitude of the penalizing term required to produce physically meaningful fluctuations, and the Reynolds decomposition of the volume penalizing term that allows the model to be evaluated inexpensively on a wave number by wave number basis. The volume penalization model results in good agreement between leading resolvent modes and data, and introduces a geometry-dependent forcing term which determines mode weights. Here, the method is applied to model the wake field fluctuations observed in fully rough turbulent channel flows over sand-grain roughness as a proxy for engineering-type roughness at different Reynolds numbers, and compared with results from DNS and LES.

4.2 Mathematical description of RAVP

Governing equations

RAVP is developed from the Navier-Stokes equations formed with a drag term $-D\mathbf{u}$ which depends on an encoding of the roughness geometry D and the fluid velocity $\mathbf{u}$. D depends on the roughness geometry expressed as the volume of fluid fraction (VOF) $\varphi(x, y, z)$ and a real-valued magnitude parameter D_{max}, which is closed to normalize the integral of the drag term.

With physical variables denoted by the superscript *, the governing equations are formed as:

$$\begin{aligned}\frac{\partial \mathbf{u}^*}{\partial t^*} + \mathbf{u}^* \cdot \nabla^* \mathbf{u}^* &= -\frac{1}{\rho}\nabla^* p^* + \nu \nabla^{*2}\mathbf{u}^* - \frac{1}{\rho} D^* \mathbf{u}^* \\ \nabla^* \cdot \mathbf{u}^* &= 0 \\ D^* &= D^*_{max}[1-\varphi].\end{aligned} \tag{4.1}$$

Then, the governing equations are nondimensionalized such that velocity is normalized by u_τ, spatial dimensions by δ, time by δ/u_τ, pressure by ρu_τ^2, and D by $\rho u_\tau/\delta$,

$$\begin{aligned}\frac{\partial \mathbf{u}}{\partial t} + \mathbf{u} \cdot \nabla \mathbf{u} &= -\nabla p + \frac{1}{Re_\tau}\nabla^2 \mathbf{u} - D\mathbf{u} \\ \nabla \cdot \mathbf{u} &= 0 \\ D &= D_{max}[1-\varphi].\end{aligned} \tag{4.2}$$

The volume fraction of fluid representation of a roughness surface

Any surface specified as a height function which depends on spatial coordinates, e.g. $r(x,z)$ in a Cartesian grid, has a unique VOF representation, $\varphi(x,y,z)$. In a continuous 3D space, this is expressed mathematically that for any point,

$$\varphi(x,y,z) = \begin{cases} 0 & y(x,z) \leq r(x,z) \\ 1 & y(x,z) > r(x,z). \end{cases} \tag{4.3}$$

The discretization of a computational grid means that the VOF of a grid cell centered at (x_i, y_i, z_i) can be between 0 and 1, depending on how the roughness surface $r(x,z)$ intersects the grid cell. The grid cells which have a VOF between 0 and 1 are important when solving the DNS with IBM which generated the reference dataset (Hantsis and Piomelli, 2020). However, when computing statistics on the fluid domain only, a strict VOF approach is used, where any cell with $\varphi < 1$ is set to $\varphi = 0$, such that when an average is taken over a fluid quantity multiplied by φ, only data in cells which do not contain any of the solid are considered. The strict VOF approach is also taken for the results presented for RAVP in this chapter.

Using the mean momentum equation to close the magnitude parameter

The driving principle for closing the magnitude parameter is that the integral in y of the resulting double-averaged drag term in the mean momentum equation should approach 1 in inner units. For the IBM scheme of the reference data, written with the spatial variables in outer units and velocities in inner units, this results in

$$\frac{1}{Re_\tau}\frac{d\langle \overline{u} \rangle_s}{dy} - \left\langle \overline{u'v'} \right\rangle_s - \langle \tilde{u}\tilde{v} \rangle_s + \int_y^1 \left\langle \overline{f_d} \right\rangle_{xz} dy' = y - 1, \tag{4.4}$$

where f_d is the IBM force (Brereton and Yuan, 2018). As $y \to 0$, the following trends are observed:

$$\begin{aligned} \frac{d\left\langle \overline{u} \right\rangle_s}{dy} &\to 0 \\ \left\langle \overline{u'v'} \right\rangle_s &\to 0 \\ \left\langle \tilde{u}\tilde{v} \right\rangle_s &\to 0. \end{aligned} \tag{4.5}$$

This is because near the bottom and top of the domain, roughness occupies most of the grid so that the fluid is nearly static. With these trends, the mean momentum equation can simplify at $y = 0$ to

$$\int_0^1 \left\langle \overline{f_d} \right\rangle_{xz} dy' = -1. \tag{4.6}$$

The mean momentum equation of RAVP computed by plane averaging is

$$\frac{1}{Re_\tau}\frac{d\left\langle \overline{u} \right\rangle_s}{dy} - \left\langle \overline{u'v'} \right\rangle_s - \left\langle \tilde{u}\tilde{v} \right\rangle_{xz} - \int_y^1 \left\langle D\overline{u} \right\rangle_{xz} dy' = y - 1, \tag{4.7}$$

taking into account that the plane average of a flow quantity is equal to the superficial average when that quantity is 0 inside the roughness, so $\left\langle \overline{u} \right\rangle_{xz} = \left\langle \overline{u} \right\rangle_s$ and $\left\langle \overline{u'v'} \right\rangle_{xz} = \left\langle \overline{u'v'} \right\rangle_s$. This gives the similar condition that

$$\int_0^1 \left\langle D\overline{u} \right\rangle_{xz} dy' = 1. \tag{4.8}$$

Taking the form of D in Eq. 4.2 yields the condition that

$$D_{max} \int_y^1 \left[\left\langle 1 - \varphi \right\rangle_{xz} \left\langle \overline{u} \right\rangle_s - \left\langle \tilde{\varphi}\tilde{u} \right\rangle_{xz} \right] dy' = 1. \tag{4.9}$$

While the mean $\left\langle \overline{u} \right\rangle_s$ and φ are inputs to the analysis, $\tilde{u}$ remains unknown. However, if $\left\langle \tilde{\varphi}\tilde{u} \right\rangle_{xz}$ is considered small, then a simplified condition can be written for a scalar D_{max},

$$D_{max} = \frac{1}{\int_y^1 \left\langle 1 - \varphi \right\rangle_{xz} \left\langle \overline{u} \right\rangle_s dy'}. \tag{4.10}$$

For a D_{max} which varies with y, tuned such that the plane-averaged profile matches the IBM profile from the reference data $\left\langle \overline{f_d} \right\rangle_{xz}$, the D_{max} parameter can be determined by

$$D_{max}(y) = -\frac{\left\langle \overline{f_d} \right\rangle_{xz}}{\left\langle 1 - \varphi \right\rangle_{xz} \left\langle \overline{u} \right\rangle_s}. \tag{4.11}$$

By definition, this version of the parameter also normalizes the magnitude achieved by the drag term integral at $y = 0$. The resulting force profiles for a scalar D_{max} and $D_{max}(y)$ are compared to the IBM force in Figure 4.1.

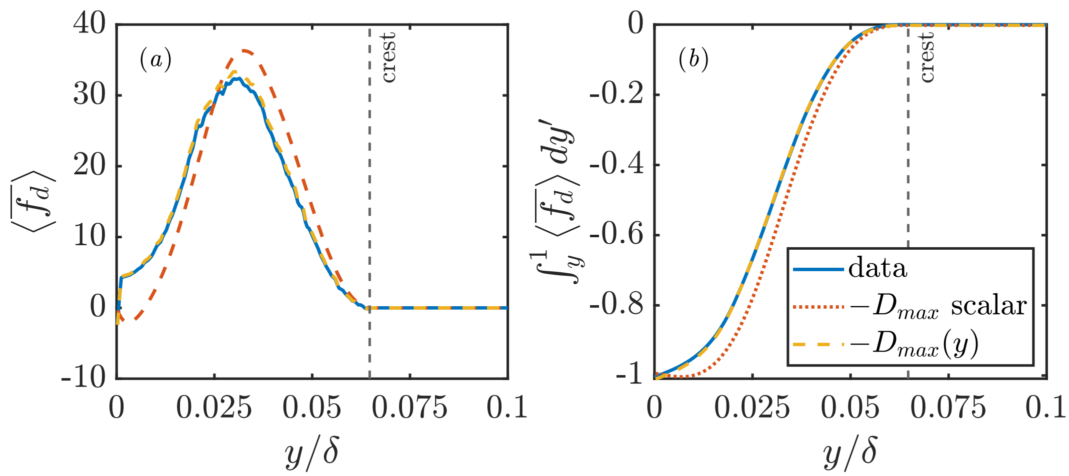

Figure 4.1: (a) The plane-averaged drag term from the IBM simulation, RAVP with a scalar D_{max}, and RAVP with a $D_{max}(y)$ tuned to match the IBM force. (b) Drag terms integrated in y normalize to 1 at the bottom and top of the domain.

Derivation of RAVP

The fluctuations and volume penalization term are Reynolds-decomposed with respect to the plane average. This is consistent with taking the Fourier analysis of the data over all values within the domain, including inside cells where the volume fraction is 0.

$$\begin{aligned} \tilde{D} &= D - \langle D \rangle_{xz} \\ \mathbf{u}'' &= \mathbf{u} - \langle \overline{\mathbf{u}} \rangle_s , \end{aligned} \tag{4.12}$$

so the equations for the fluctuations are written,

$$\begin{aligned} \frac{\partial \mathbf{u}''}{\partial t} + \langle \overline{\mathbf{u}} \rangle_s \cdot \nabla \mathbf{u}'' + \mathbf{u}'' \cdot \nabla \langle \overline{\mathbf{u}} \rangle_s - \frac{1}{Re_\tau} \nabla^2 \mathbf{u}'' + \nabla p'' + \langle D \rangle_{xz} \mathbf{u}'' &= \mathbf{f} - \tilde{D} \langle \overline{\mathbf{u}} \rangle_s - \mathbf{d} \\ \mathbf{f} &= -\left(\mathbf{u} \cdot \nabla \mathbf{u} - \left\langle \overline{\mathbf{u}'' \cdot \nabla \mathbf{u}''} \right\rangle_{xz} \right) \\ \mathbf{d} &= -\left(\tilde{D} \mathbf{u}'' - \left\langle \tilde{D} \tilde{\mathbf{u}} \right\rangle_{xz} \right) \\ \nabla \cdot \mathbf{u}'' &= 0. \end{aligned} \tag{4.13}$$

Then, assuming that $\langle \overline{v} \rangle_s = \langle \overline{w} \rangle_s = 0$, RAVP is written

$$\begin{bmatrix} \hat{\mathbf{u}} \\ \hat{p} \end{bmatrix} = \underbrace{\left(-i\omega \begin{bmatrix} \mathbf{I} & \\ & 0 \end{bmatrix} - \begin{bmatrix} \mathcal{L}_\mathbf{k} - \mathcal{D} & -\nabla \\ \nabla^\top & 0 \end{bmatrix} \right)^{-1}}_{\text{Resolvent } \mathcal{H} \in \mathbb{C}^{4N_y \times 3N_y}} \begin{bmatrix} \mathbf{I} \\ 0 \end{bmatrix} \left(\hat{\mathbf{f}} - \hat{D} \langle \overline{\mathbf{u}} \rangle_s + \hat{\mathbf{d}} \right), \tag{4.14}$$

where

$$\mathcal{L}_{\mathbf{k}} \triangleq \begin{bmatrix} -ik_x \langle \overline{u} \rangle_s + Re_\tau^{-1}\Delta & \partial_y \langle \overline{u} \rangle_s & \\ & -ik_x \langle \overline{u} \rangle_s + Re_\tau^{-1}\Delta & \\ & & -ik_x \langle \overline{u} \rangle_s + Re_\tau^{-1}\Delta \end{bmatrix}$$

$$\mathcal{D} \triangleq \begin{bmatrix} \operatorname{diag} \langle D \rangle_{xz} & & \\ & \operatorname{diag} \langle D \rangle_{xz} & \\ & & \operatorname{diag} \langle D \rangle_{xz} \end{bmatrix} \tag{4.15}$$

$$\nabla \triangleq \begin{bmatrix} ik_x \\ \frac{\partial}{\partial y} \\ ik_z \end{bmatrix}, \quad \Delta \triangleq \frac{\partial^2}{\partial y^2} - k_x^2 - k_z^2, \quad \hat{\mathbf{u}} \triangleq \begin{bmatrix} \hat{u} \\ \hat{v} \\ \hat{w} \end{bmatrix}, \quad \hat{\mathbf{f}} \triangleq \begin{bmatrix} \hat{f}_1 \\ \hat{f}_2 \\ \hat{f}_3 \end{bmatrix},$$

or in the shorter form

$$\begin{bmatrix} \hat{\mathbf{u}} \\ \hat{p} \end{bmatrix} = \underset{\sim}{\mathcal{H}} \left(\hat{\mathbf{f}} - \hat{D} \langle \overline{\mathbf{u}} \rangle_s + \hat{\mathbf{d}} \right). \tag{4.16}$$

Using the SVD $\underset{\sim}{\mathcal{H}} = \sum_{j=1}^{N} \underset{\sim}{\sigma}_j \underset{\sim}{\psi}_j \underset{\sim}{\phi}_j^\dagger$, a modal representation can be written

$$\begin{bmatrix} \hat{\mathbf{u}} \\ \hat{p} \end{bmatrix} = \sum_{j=1}^{N} \underset{\sim}{\sigma}_j \underset{\sim}{\psi}_j \underset{\sim}{\chi}_j \quad \text{where} \quad \underset{\sim}{\chi}_j = \left\langle \underset{\sim}{\phi}_j, \hat{\mathbf{f}} - \hat{D} \langle \overline{\mathbf{u}} \rangle_s + \hat{\mathbf{d}} \right\rangle. \tag{4.17}$$

It is observed that the drag term changes the modes from RAVP as compared to those from conventional resolvent analysis. Also, two additional terms in the equation for the weights appear. First, a wave number-dependent component of the forcing term appears, $\hat{D} \langle \overline{\mathbf{u}} \rangle_s$. This term is of particular interest since it is known from the inputs to RAVP, D and $\langle \overline{\mathbf{u}} \rangle_s$. It is nonzero only in the case of the wake field fluctuations where $\omega = 0$. The second term relates to the interaction between the wake field fluctuations and spatial variation of the roughness geometry, and is not known prior to the evaluation of the method.

Numerical details of the resolvent analysis presented

For the comparisons made in this chapter, the resolvent operators are computed on a 200 point Chebyshev grid defined on $y_{cheb} \in [-1, 1]$, which maps to $y/\delta \in [0, 2.064]$ by Eq. 3.2, as in Ch. 3. The reconstructions and model are calculated using the leading 25 symmetric resolvent modes.

RAVP for predicting wake field fluctuations

With modeling assumptions and simplifications, RAVP can provide predictions for turbulent fluctuations given the mean and roughness geometry.

For wake field fluctuations ($k_x \neq 0, k_z \neq 0, \omega = 0$), the $\hat{D}\langle\overline{\mathbf{u}}\rangle$ term is known, while $\hat{\mathbf{f}}$ and $\hat{\mathbf{d}}$ are unclosed. A model for predicting the wake field fluctuations can be formed by assuming that the unclosed terms are small, yielding

$$\begin{bmatrix}\hat{\mathbf{u}}\\ \hat{p}\end{bmatrix} \approx \sum_{j=1}^{N} \underset{\sim}{\sigma}_j \underset{\sim}{\psi}_j \underset{\sim}{\check{\chi}}_j \quad \text{where} \quad \underset{\sim}{\check{\chi}}_j \triangleq \left\langle \underset{\sim}{\phi}_j, -\hat{D}\langle\overline{\mathbf{u}}\rangle \right\rangle. \tag{4.18}$$

This model assumes that the wake field can be well modeled using a sum of resolvent modes computed at wave numbers $(k_x, k_z, 0)$ which are linearly excited by the corresponding roughness mode $\hat{D}(k_x, k_z)$. In this analysis, results are given using this assumption. Figure 4.2 depicts this model.

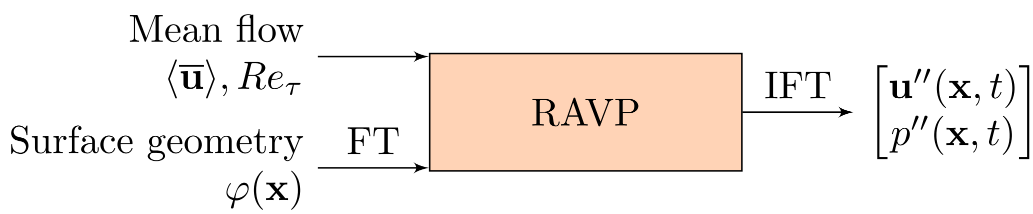

Figure 4.2: RAVP with linear excitation forms a model for the fluctuations given the mean flow and the surface geometry.

It is important to note that this form cannot account for the possibility that roughness modes can also excite responses at harmonics of that roughness mode, e.g. $(n_x k_x, n_z k_z, 0)$ where $n_x, n_z \in \mathbb{Z}^+$ are positive integers greater than 0. This phenomenon can only be accounted for through $\hat{\mathbf{d}}$.

This form also does not account for the possibility that $\hat{\mathbf{f}}$ could be large. The effectiveness of these assumptions is evaluated in the subsequent results.

RAVP for convecting fluctuations

For predicting convecting fluctuations where $\omega > 0$, the $-\hat{D}\langle\overline{\mathbf{u}}\rangle_s$ term is inactive. Therefore, the convecting modes can only be forced through the action of the nonlinear term $\hat{\mathbf{f}}$ and the interaction between convecting modes and roughness modes, $\hat{\mathbf{d}}$.

4.3 Datasets for validation

The dataset considered in this section contains the mean flow and dispersive stress profiles, roughness geometries, and temporally averaged velocity data from a DNS simulation of a channel flow with sand grain roughness on both top and bottom walls. The roughness is represented using a volume of fluid fraction IBM Hantsis,

2022. The flow is in the fully rough regime. This dataset is fully detailed in Section 2.5, and key parameters are reproduced here for convenience.

Case	Geometry	k/δ	L_x/δ	L_z/δ	Method	Re_τ	Re_b
1	SG 6x3	0.04	6	3	DNS	1745	21,400

Table 4.1: Sand grain roughness case for RAVP validation.

4.4 Evaluating the capability of RAVP modes to represent data modes

The predictive capacity of the RAVP modes is evaluated by computing the projection coefficient of data modes onto the basis modes. The projection coefficient γ of mode $\hat{\boldsymbol{u}}$ on a basis consisting of modes ψ_1 through ψ_N with respect to some inner product $\langle\cdot\rangle$ and associated norm $||\cdot||$ is defined as

$$\gamma(\hat{\mathbf{u}}, \psi_{1-N}) \triangleq \sqrt{\sum_{j=1}^{N}\left(\frac{\left|\langle\hat{\mathbf{u}}, \psi_j\rangle\right|}{||\hat{\mathbf{u}}||\,||\psi_j||}\right)^2}. \tag{4.19}$$

γ takes on a value between 1, which denotes that the data modes can be perfectly described by a weighted sum of the basis modes, and 0, which denotes that the basis cannot describe the data modes.

In this section, three sets of resolvent modes are compared as documented in Table 4.2.

Case	Description	Re_τ
RA-s	Smooth wall modeled mean	1745
RA-r	Rough wall data mean	1745
RAVP	Rough wall data mean + volume penalization	1745

Table 4.2: Resolvent analysis cases.

To determine where in wave number space the modes are energetic, a measure of mode kinetic energy is used,

$$E(\mathbf{k}) = \int_0^2 \left(|\hat{u}(\mathbf{k})|^2 + |\hat{v}(\mathbf{k})|^2 + |\hat{w}(\mathbf{k})|^2\right) dy. \tag{4.20}$$

Figure 4.3 depicts the projection coefficient for the data onto the first symmetric mode for resolvent analysis for the RA-s, RA-r, and RAVP cases. Both the RA-r and RAVP results show regions of wave number space where the projection coefficient is high, while the RA-s projection coefficient is relatively low throughout wavenumber space. RA-r performs better, and in particular there is a region at low streamwise wavenumber where the projection coefficient is particularly high, indicating that the first mode describes the data very well. RAVP also has reasonable first mode performance across wavenumber space. The overlaid contour shows where the mode kinetic energy is 10% of the observed maximum across wave number space. The contour differentiates between an energetic interior region (smaller k_x, k_z) and a less energetic outer region (larger k_x, k_z). The RA-r and RAVP bases perform well in the energetic region of wave number space, which is most relevant for modeling.

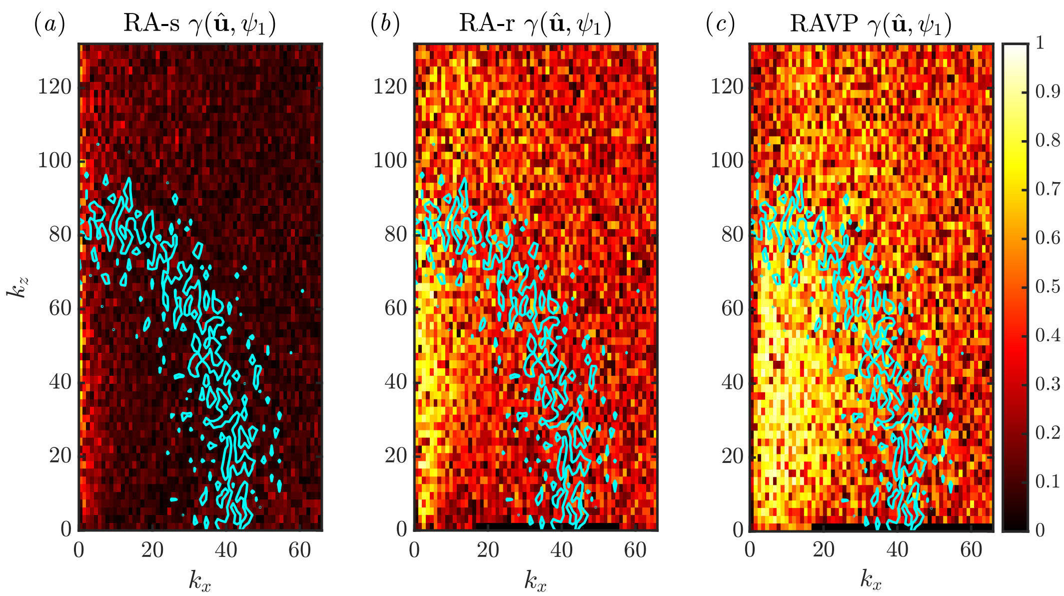

Figure 4.3: Spectra of the projection coefficient for the wake field data onto the first symmetric resolvent mode for resolvent analysis with (a) smooth mean, (b) rough mean, (c) rough mean and volume penalization (RAVP). The overlaid contour indicates where the wake field TKE is 10% of its maximum.

Figure 4.4 depicts the projection coefficient for the first through fourth symmetric modes. The additional 3 modes improve the performance of all cases, and it can be expected with additional modes that the projection coefficient will improve due to orthogonality.

To clarify what is responsible for the higher projection coefficient values demonstrated by RAVP, a single data wake field mode is compared with the leading resolvent mode from RA-s, RA-r, and RAVP in Figure 4.5. The wall-normal localization of the RA-s mode is lower than that of the RA-r mode, showcasing the effect of the different mean profiles to shift the location of peak response in the $\omega = 0$ modes. The addition of the $-\langle D \rangle_{xz}$ terms in the RAVP operator results in a further

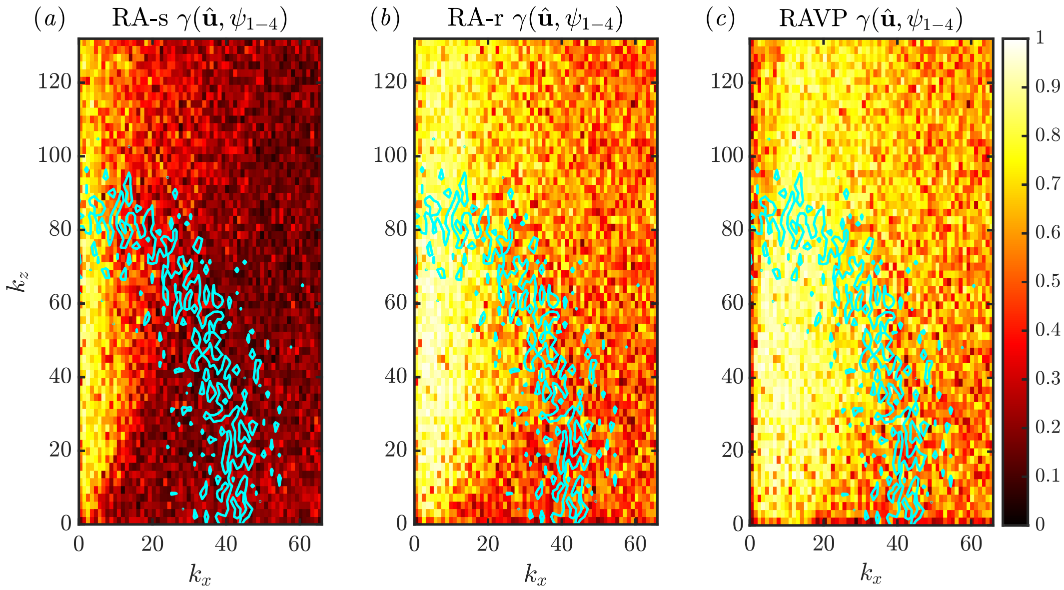

Figure 4.4: Spectra of the projection coefficient for the wake field data onto the first through fourth symmetric resolvent modes for resolvent analysis with (a) smooth mean, (b) rough mean, and (c) rough mean with volume penalization (RAVP).

shift in the location of the peak for all components, which helps the RAVP modes to describe the data more effectively.

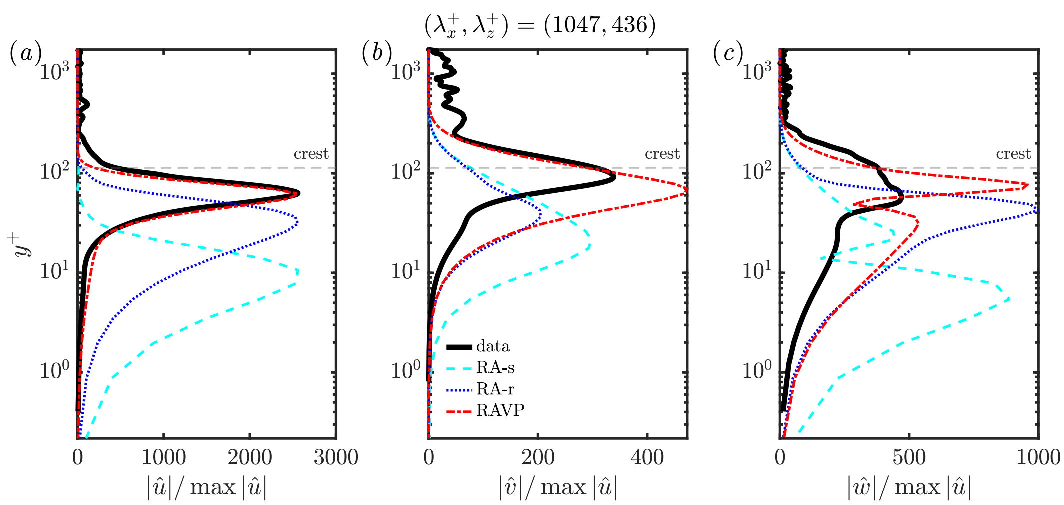

Figure 4.5: Mode shape comparison between wake field and RA-s, RA-r, and RAVP mode shapes. The mode shapes are normalized by their maximum u component magnitude.

Overall, this analysis highlights that the RAVP response mode basis is effective for describing the wake field response.

4.5 Evaluation of RAVP-predicted weights

To evaluate the ability of the forcing modes to capture the RAVP-modeled forcing, the projection coefficient of the forcing term $\hat{D}\,\langle\overline{u}\rangle_s$ onto the first forcing mode is plotted in Figure 4.6. The projection coefficient of the forcing onto the first forcing

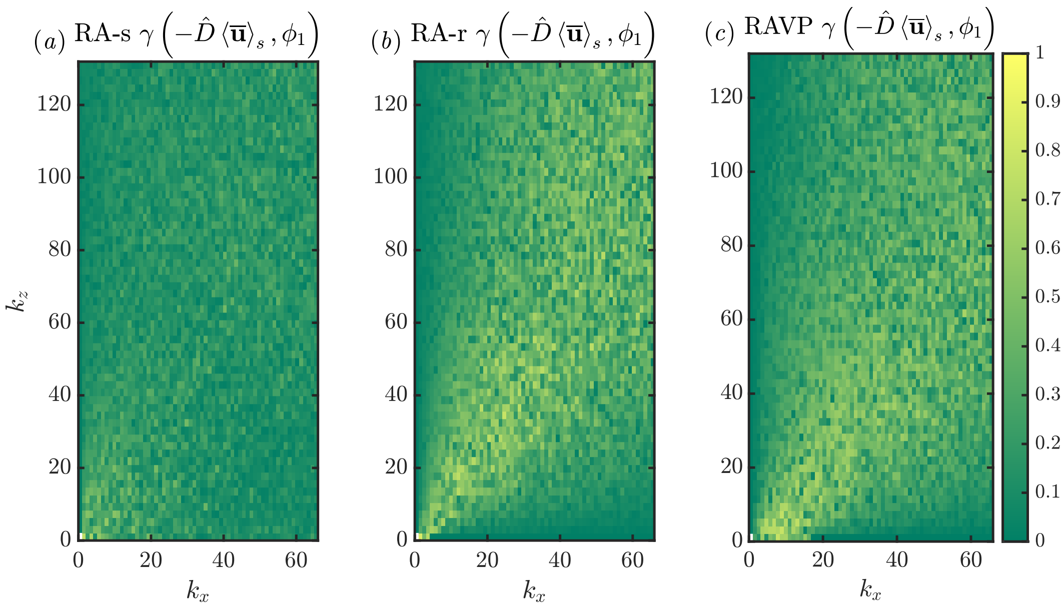

Figure 4.6: Spectra of the projection coefficient for the RAVP forcing term onto the first symmetric resolvent forcing mode for (a) RA-s, (b) RA-r, and (c) RAVP.

mode is stronger for RA-r and RAVP than RA-s. The projection coefficient of the forcing on the leading forcing modes is smaller than that of the wake field onto the leading response modes depicted in Figure 4.3. This is reasonable due to the low-rank nature of the resolvent operator, where the linear amplification of the leading mode often dominates that of the subsequent modes in the SVD expansion.

Figure 4.7 depicts the projection coefficient of the forcing onto the first eight forcing modes. For large portions of wave number space, the forcing bases provided by RA-r and RAVP can describe the forcing well. It is notable that the projection coefficient for RA-r, and to a greater extent RAVP, remains small for low streamwise wave numbers, indicating that the resolvent forcing basis is somehow inefficient at these low wave numbers.

Now that the ability of the RAVP forcing mode basis to describe the RAVP forcing has been evaluated, the question remains as to whether that projection results in reasonable values for the weights. To evaluate the efficacy of the RAVP model form for the weights, magnitude spectra of the reconstruction (best-fit) weights and

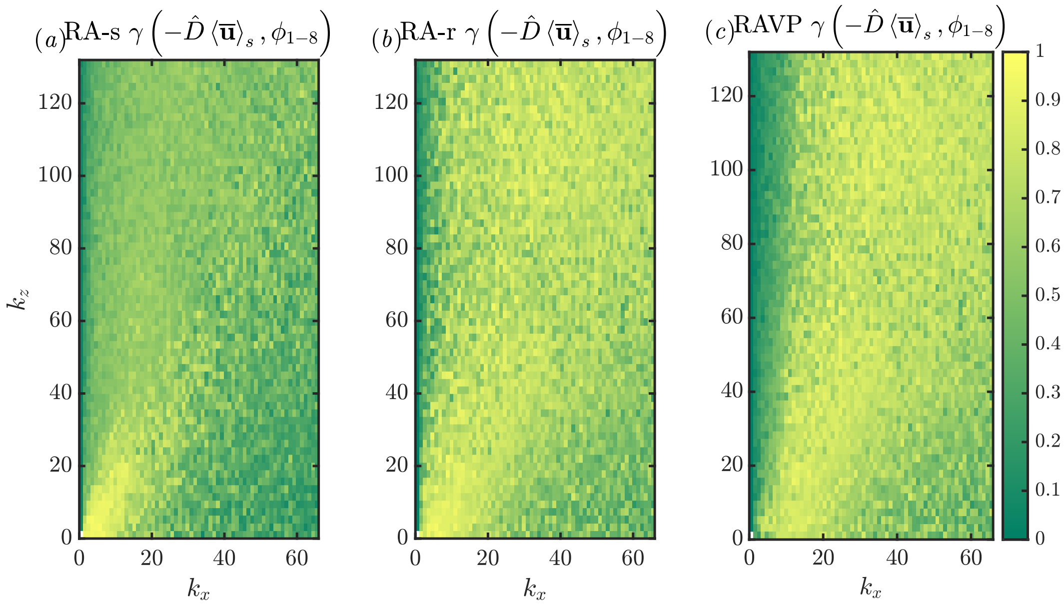

Figure 4.7: Spectra of the projection coefficient for the RAVP forcing term onto the first symmetric resolvent forcing mode for (a) RA-s, (b) RA-r, and (c) RAVP.

modeled weights for the first three symmetric RAVP modes are compared in Figure 4.8. The reconstruction weights are computed in the same manner as in Section 3.2.

Qualitatively, the modeled weights reproduce the trends in the best-fit weights, although the modeled weights generally have smaller magnitude. This trend is exacerbated at larger wave numbers, or smaller scales. The agreement between the best-fit and modeled weights also decreases from the first to third resolvent modes, indicating that the ability of the modeled weights to force modes further down the SVD decreases.

4.6 Predictions of wake field fluctuations from RAVP

The ability of RAVP to model aspects of the wake field fluctuations and statistics is examined here by comparing between the low-pass filtered wake field over sand grain roughness and the predictions given by RAVP calculated over that same set of wave numbers,

$$\begin{aligned} \frac{k_x}{\Delta k_x} &\in [0, 64] \\ \frac{k_z}{\Delta k_z} &\in [-64, 64], \end{aligned} \tag{4.21}$$

where $\Delta k_x = 1.05$ and $\Delta k_z = 2.09$. From a total of $N_x \times N_z = 512 \times 256$ wave numbers, 64×128 wave numbers are considered in this analysis.

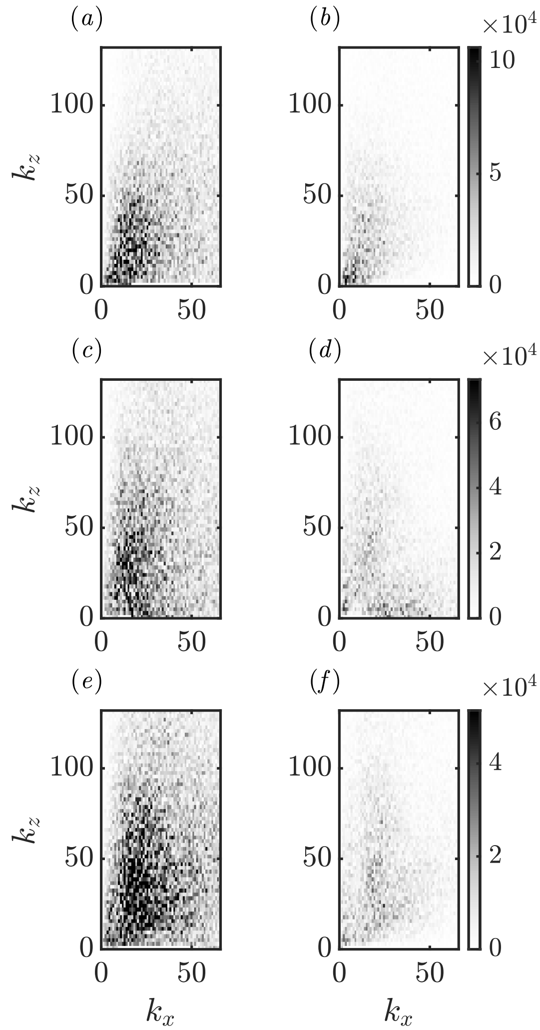

Figure 4.8: Spectra of the (left) best fit χ_j and (right) RAVP modeled χ_j weights for (a-b) $j = 1$, (c-d) $j = 2$, (e-f) $j = 3$.

Figure 4.9 compares the visual appearance of the filtered, RAVP-reconstructed, and RAVP-modeled wake field fluctuations for the velocity components at $y/\delta = 0.03$, which is approximately halfway between the lowest and highest points of the roughness geometry. Visually, the reconstruction and filtered data agree well for all three components. The prediction provided by RAVP shows promising qualitative agreement with the data for all three components, suggesting that the weights model captures at least some of the phase relationship between the velocity and roughness modes. The low streamwise velocity downstream of roughness elements and high streamwise velocity between elements is predicted by this model. Also, the model predicts the upwards wall-normal velocity behind roughness elements which occurs due to recirculation reasonably well. Comparing the spanwise velocity fields indicates that the turning of the flow around roughness elements is somewhat captured.

The predicted magnitude of fluctuations is slightly lower than the data for all three velocity components, though predominantly in the wall-normal and spanwise components. For the wall-normal velocity component, the shape of the response is well predicted, but the model struggles to reproduce areas of particularly high or low velocity. The spanwise component has the least promising agreement, suggesting that the model does not enforce the horizontal turning of the flow as effectively. The areas of low streamwise velocity downstream of the roughness elements predicted by the model are somewhat elongated compared to the data. It is possible that the model over-predicts the velocity decrease induced by a particular roughness element. Furthermore, the model does not predict well the more intuitive upwards velocity often observed in front of roughness elements.

These differences are quantified in Figure 4.10 which plots the spatially-varying normalized residual e_{pp} of the reconstruction and model with respect to the filtered data at $y/\delta = 0.03$, normalized by the peak-to-peak value of the filtered data. The definition of the normalized residual is given as

$$e_{pp}\left(y; u_f, u^\star\right) = \frac{u^\star(y) - u_f(y)}{\max\left(u_f(y)\right) - \min\left(u_f(y)\right)}. \tag{4.22}$$

The normalized residual has directionality, assuming values between -1 and 1 corresponding to underestimation and overestimation compared to the data, respectively. The reconstruction has a small residual for all three components. The residual magnitude of the modeled velocity is less than 1 across the domain for all components. The streamwise residual has the most activity, while the wall-normal and spanwise residuals have notable magnitudes only in certain locations. The streamwise residual of the model is often positive within and immediately downstream of the roughness elements, where the streamwise wake field velocity is negative due to the volume penalization. In extended regions of fluid downstream of roughness elements, the streamwise residual is often negative since the model predicts longer regions of lower velocity than exists in the data. The wall-normal residual illustrates that the model does not predict particularly strong wall-normal fluctuations that are sometimes observed next to (at similar streamwise coordinate x/δ, but adjacent spanwise coordinate z/δ) roughness elements. These regions correspond approximately to where the spanwise fluctuations are not as well estimated, suggesting that modeling errors in the wall-normal and spanwise components are possibly correlated.

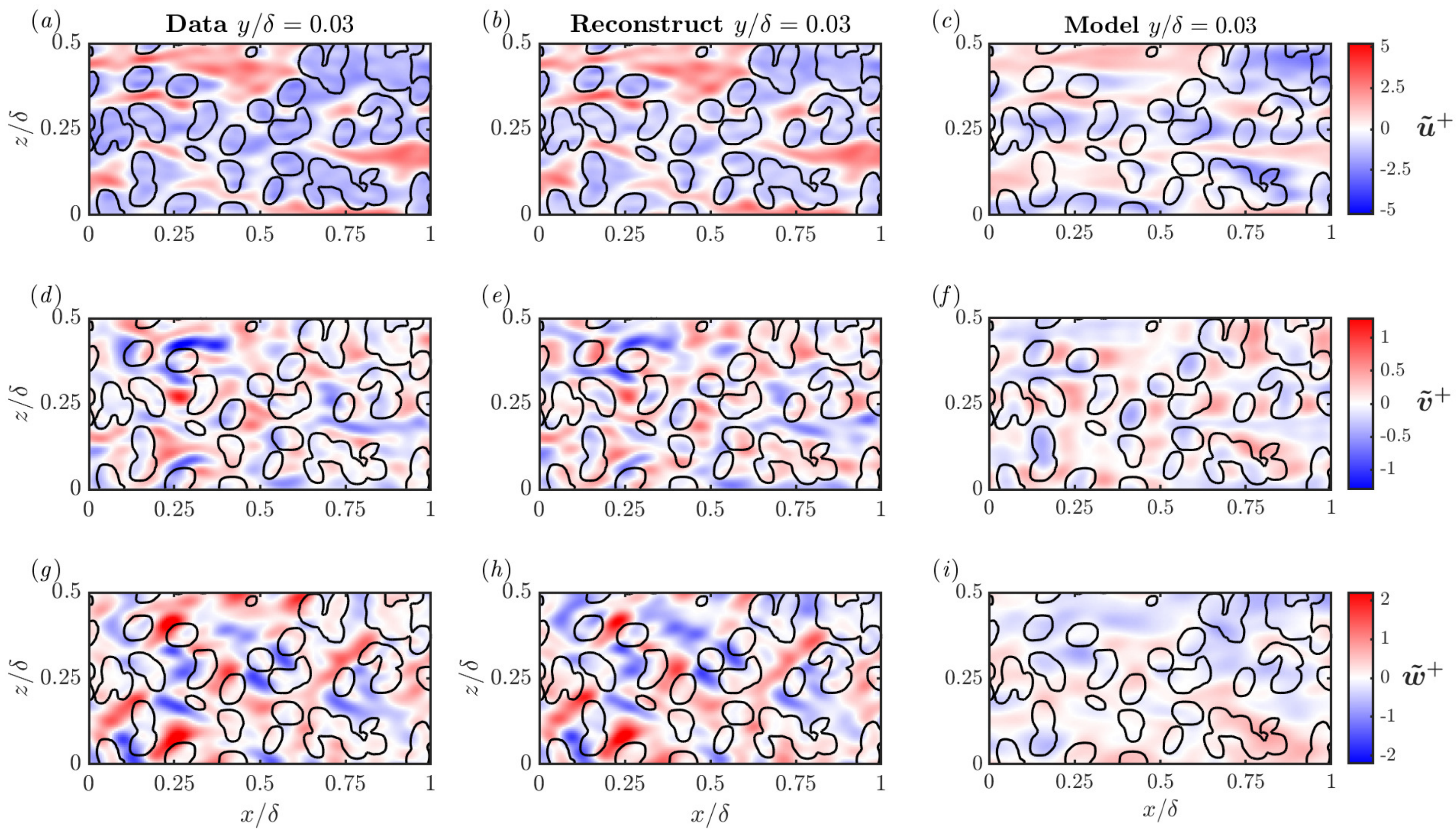

Figure 4.9: Re_τ = 1745 wake field filtered data, reconstruction, and predictions from RAVP plotted at y/δ = 0.03. (a) Data $\tilde{u}$, (b) Reconstruction $\tilde{u}$, (c) Model $\tilde{u}$, (d) Data $\tilde{v}$, (e) Reconstruction $\tilde{v}$, (f) Model $\tilde{v}$, (e) Data $\tilde{w}$, (f) Reconstruction $\tilde{w}$, (g) Model $\tilde{w}$.

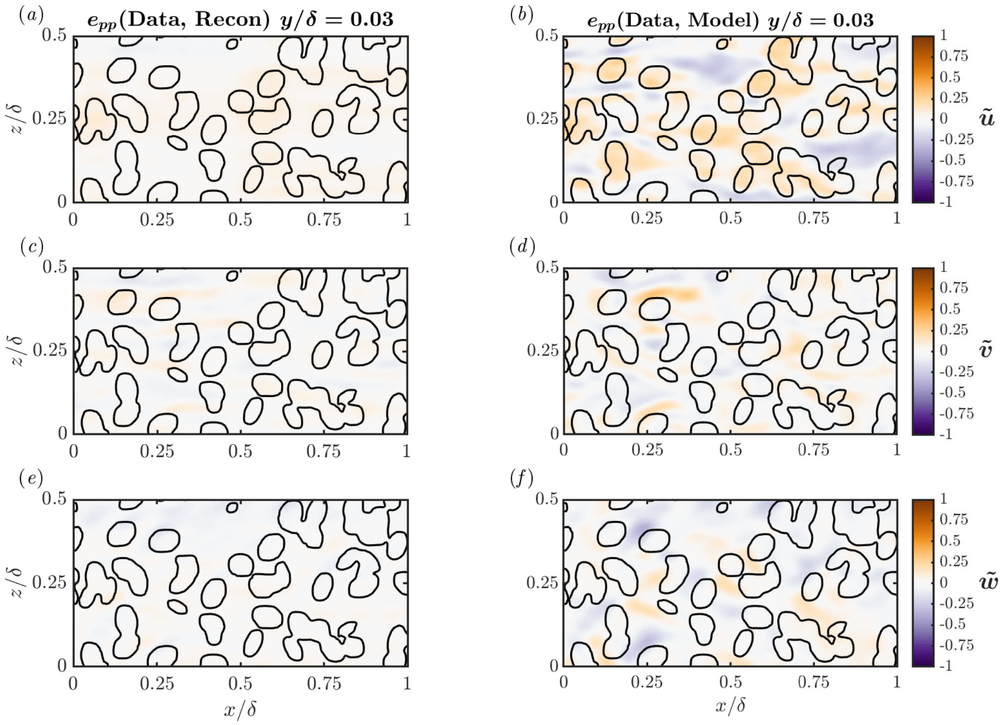

Figure 4.10: Normalized residual comparing the $Re_\tau = 1745$ wake field filtered data with the RAVP reconstruction and model plotted at $y/\delta = 0.03$. (a) Data vs. Reconstruction $\tilde{u}$, (b) Data vs. Model $\tilde{u}$, (c) Data vs. Reconstruction $\tilde{v}$, (d) Data vs. Model $\tilde{v}$, (e) Data vs. Reconstruction $\tilde{w}$, (f) Data vs. Model $\tilde{w}$.

Figure 4.11 compares the data, reconstruction, and model at $y/\delta = 0.05$, which is slightly below the highest point of the roughness at $y/\delta \approx 0.06$. At this wall-normal location, the reconstruction matches the data well. When comparing the data and modeled streamwise velocity, it is evident that the model predicts much longer regions of lower streamwise velocity. The shape of the wall-normal and spanwise responses also obey similar behavior to a lesser extent. This behavior has a few possible sources. First, the modeled weights underestimate the excitement of higher wave numbers, so smaller wavelength flow features may be underestimated by the model. Second, small streamwise wave numbers experience high linear amplification of small streamwise wave numbers in resolvent analysis, which may lead to an overestimation of long wavelength streamwise flow features. Third, the wall-normal localization of modes calculated at small streamwise wave numbers may be overestimated, though the projection coefficient plots suggest that the wall-normal localization of the RAVP and data wake field modes agree well. It is possible that modifications to the analysis, such as a careful consideration of the effective location of the wall, may improve these results.

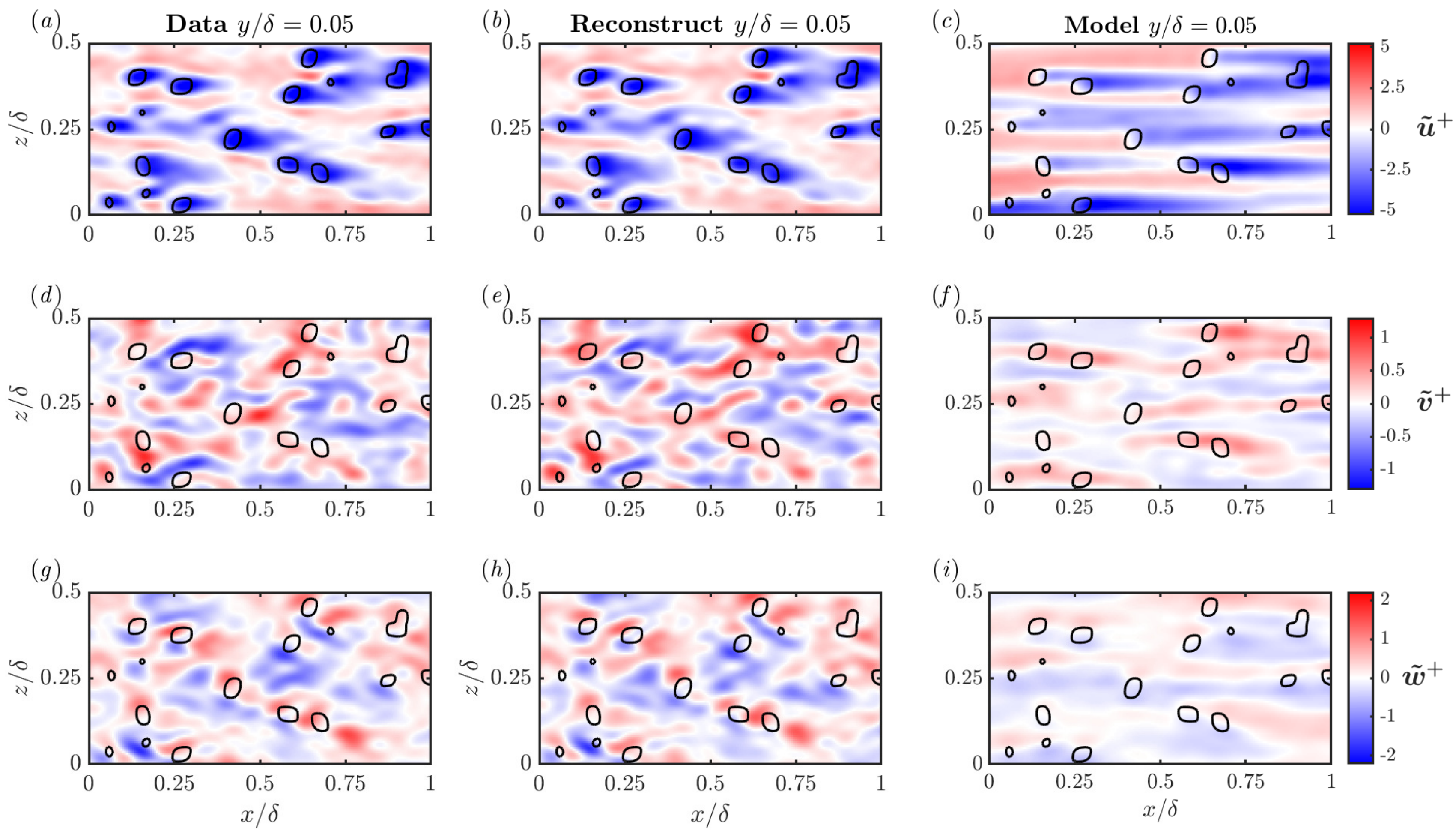

Figure 4.11: Re_τ = 1745 wake field filtered data, reconstruction, and predictions from RAVP plotted at y/δ = 0.05. (a) Data $\tilde{u}$, (b) Reconstruction $\tilde{u}$, (c) Model $\tilde{u}$, (d) Data $\tilde{v}$, (e) Reconstruction $\tilde{v}$, (f) Model $\tilde{v}$, (e) Data $\tilde{w}$, (f) Reconstruction $\tilde{w}$, (g) Model $\tilde{w}$.

Figure 4.12 plots the normalized residual e_{pp} of the reconstruction and model with respect to the filtered data at $y/\delta = 0.05$. The residual for the reconstruction is small, indicating that the modal basis remains suitable for predicting the response. The residual of the model is higher. In the streamwise component, the areas of large residual magnitude correspond to the elongated regions of lower streamwise velocity behind roughness elements, where the model overestimates the streamwise length of those regions. In the wall-normal and spanwise compoennts, areas of stronger magnitude fluctuations are underestimated by the model. The trends observed in the model residual are qualitatively similar to those observed in Figure 4.10, but the model residual at $y/\delta = 0.05$ is higher in general than at $y/\delta = 0.03$, due to the overestimated length of streaky features predicted by the model at this height.

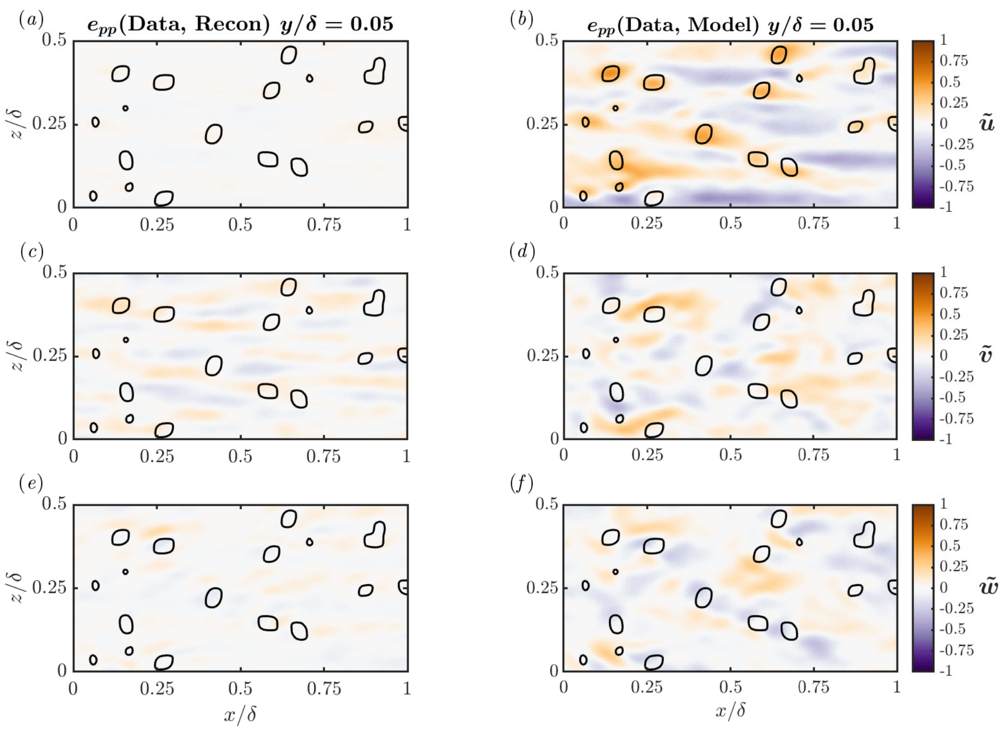

Figure 4.12: Normalized residual comparing the $Re_\tau = 1745$ wake field filtered data with the RAVP reconstruction and model plotted at $y/\delta = 0.05$. (a) Data vs. Reconstruction $\tilde{u}$, (b) Data vs. Model $\tilde{u}$, (c) Data vs. Reconstruction $\tilde{v}$, (d) Data vs. Model $\tilde{v}$, (e) Data vs. Reconstruction $\tilde{w}$, (f) Data vs. Model $\tilde{w}$.

Next, in Figure 4.13, the streamwise, wall-normal, spanwise, and shear dispersive stresses are plotted for the filtered data, RAVP reconstruction, and RAVP model. The reconstructions reproduce the streamwise stress almost exactly, while slightly under-representing the spanwise and wall-normal velocity components. The RAVP model predicts the streamwise stress above $y/\delta \approx 0.05$ reasonably well, while underestimating the streamwise stress below $y/\delta \approx 0.05$. Effectively, this results in a peak of the modeled dispersive streamwise stress that is located slightly higher than that of the data. The shear dispersive stress is also modeled reasonably well, though with a slightly lower magnitude and also a slightly higher peak.

The modeled wall-normal and spanwise stresses underestimate the data. This implies that the RAVP weights model does not excite the wall-normal and spanwise velocity components enough, given that the modes are capable of reconstructing the wall-normal and spanwise velocity components. This could reasonably be attributed to the fact that the $-D\langle\overline{\mathbf{u}}\rangle_s$ forcing only has a streamwise component, or to the low excitation of modes further down the SVD as observed in 4.5. Another possible explanation is that local resolvent modes are known to overestimate the relative strength of the streamwise velocity component as compared with the spanwise and streamwise velocity components, due to the TKE norm used when calculating the modes; this may be a feature of the RAVP modes as well. The observation that the dispersive shear and streamwise stress match well, while the wall-normal stress does not, also suggests that the weighted modes encode a phase difference between the streamwise and wall-normal components that must be larger than in the data.

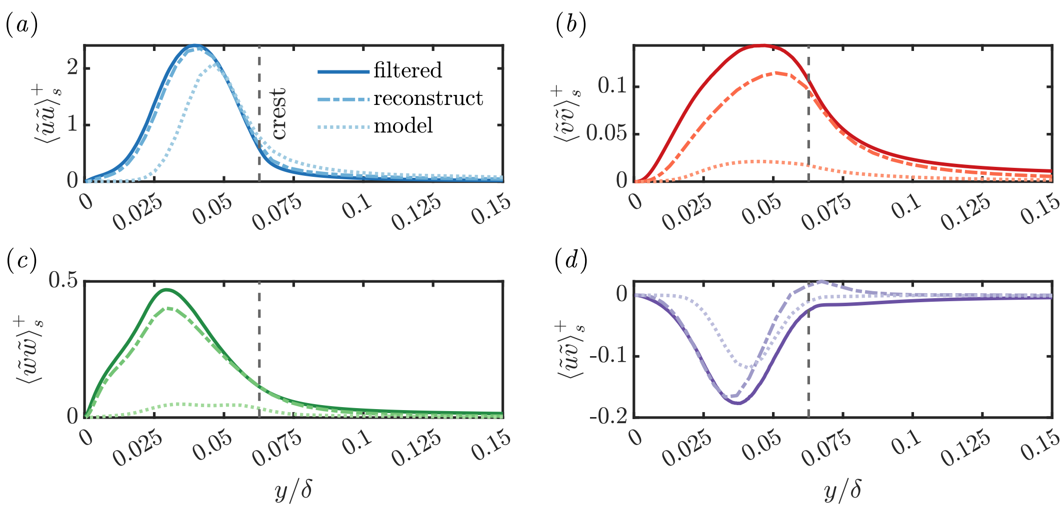

Figure 4.13: Re_τ = 1745 dispersive (a) streamwise, (b) wall-normal, (c) spanwise, and (d) shear stresses for the filtered data, RAVP reconstruction, and RAVP model.

In Figure 4.14, the correlation coefficient between the filtered data and estimates is plotted for the velocity components and the dispersive shear stress. The reconstructions correlate well with the data. The modeled $\tilde{u}$ velocity has a region where the correlation coefficient is more than 50% below the roughness crest, before rapidly decaying to 0 outside of the roughness. The other components demonstrate around

25% correlation throughout the plotted domain, and the dispersive shear stress shows a particularly low correlation. This suggests that while the model can capture the intrinsically averaged stresses well, the spatial variation of the predicted stresses differs from the data.

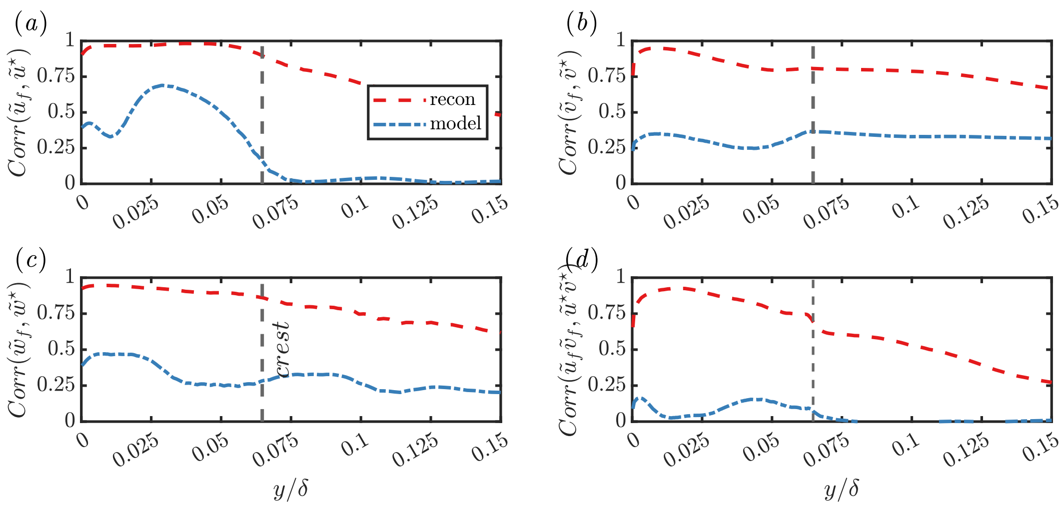

Figure 4.14: Correlation coefficient comparing the filtered wake field data to the RAVP reconstruction and RAVP model for the (a) streamwise velocity, (b) wall-normal velocity, (c) spanwise velocity, and (d) shear stress.

In Figure 4.15, the peak-to-peak normalized error between the filtered data and estimates given as

$$\mathrm{Err}_{pp}(y; \tilde{u}_f, \tilde{u}^\star) = \frac{\sqrt{\left\langle \left(\tilde{u}_f(y) - \tilde{u}^\star(y)\right)^2 \right\rangle}}{\max(\tilde{u}_f(y)) - \min(\tilde{u}_f(y))}, \tag{4.23}$$

is plotted with y. The error in the reconstructions is relatively low with respect to the range of the data at each y-height, taking values of roughly 10% or less. The model error is generally higher, with the most error observed in the streamwise component of around 25%. The wall-normal and spanwise component errors are smaller, at around 10%.

In Figure 4.16, the spectral content of the y-integrated kinetic energy is plotted for the filtered data, RAVP reconstruction, and RAVP model. The reconstruction on RAVP modes reproduces the spectra faithfully. However, the RAVP model underestimates the kinetic energy content at higher streamwise wavenumbers, and overestimates the kinetic energy content at lower streamwise wavenumbers. These results suggest that it is possible to represent the spectra with RAVP modes well. However, the

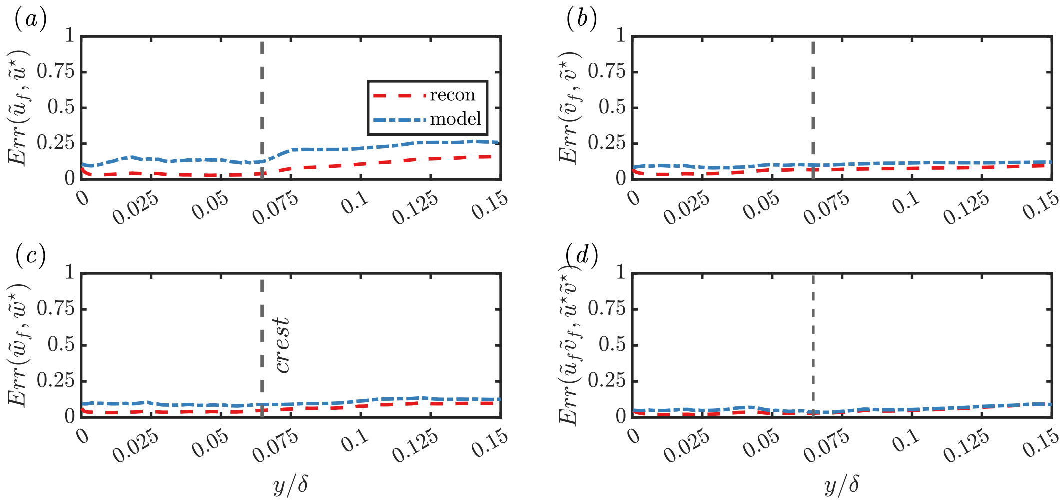

Figure 4.15: Max-min normalized error comparing the filtered wake field data to the RAVP reconstruction and RAVP model for the (a) streamwise velocity, (b) wall-normal velocity, (c) spanwise velocity, and (d) shear stress.

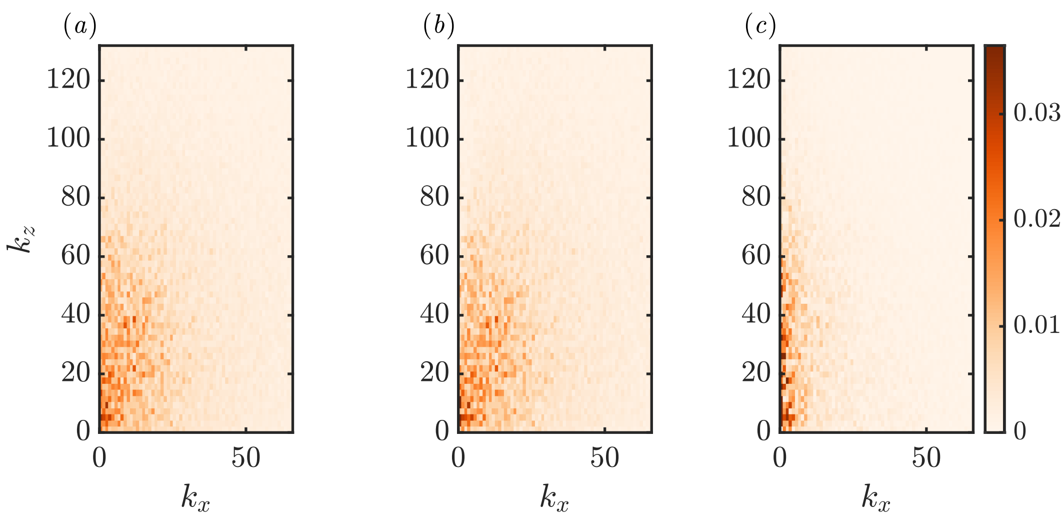

Figure 4.16: $\frac{1}{N_x N_z}\int_0^2 |\hat{\mathbf{u}}|^2+|\hat{\mathbf{v}}|^2+|\hat{\mathbf{w}}|^2 dy$ spectra of wake field for (a) data, (b) reconstruction, and (c) model.

longer regions of lower streamwise velocity may be attributed to the RAVP-modeled weights or the linear amplification of the modes, which may overexcite the RAVP modes at lower streamwise wavenumbers and/or over-exciting the modes at lower streamwise wave numbers.

To isolate these trends, the energetic content of the u, v, and w components are broken out in Figures 4.17, 4.18, and 4.19. The results for the u component strongly resemble that of the energy spectra, which is sensible because the mode kinetic energy is dominated by the streamwise velocity component. In the data, the spectra of the wall-normal and spanwise velocity components are active at higher k_x than that of the streamwise velocity component. The model does not seem to overestimate the spectral content at lower wave numbers, but underestimates the contribution of higher wave numbers to the wall-normal and spanwise velocity components. This analysis shows that the overestimation of the kinetic energy at low wave numbers is due to the overestimation of streamwise kinetic energy, even though the wall-normal and spanwise velocity spectra are still underestimated.

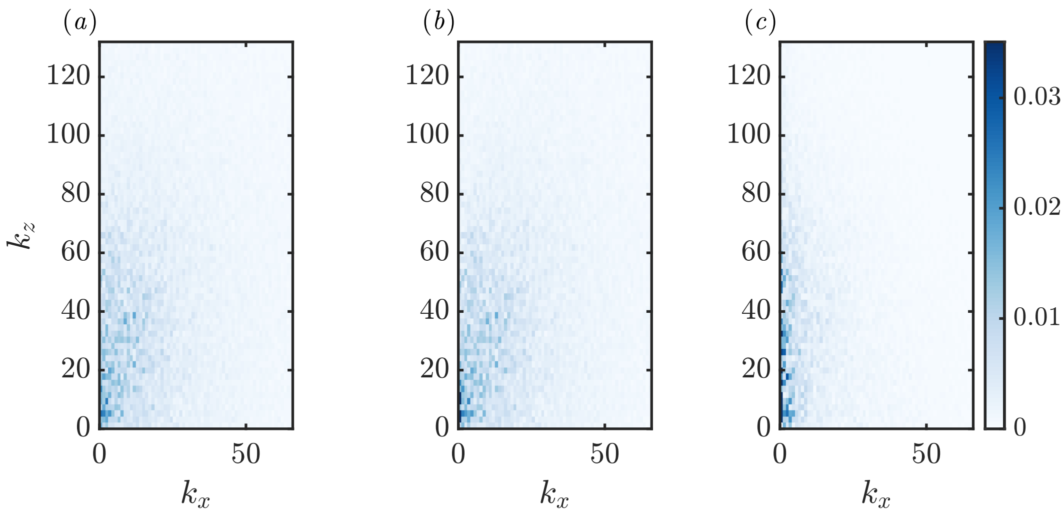

Figure 4.17: $\frac{1}{N_x N_z}\int_0^2 |\hat{\mathbf{u}}|^2 dy$ spectra of wake field for (a) data, (b) reconstruction, and (c) model.

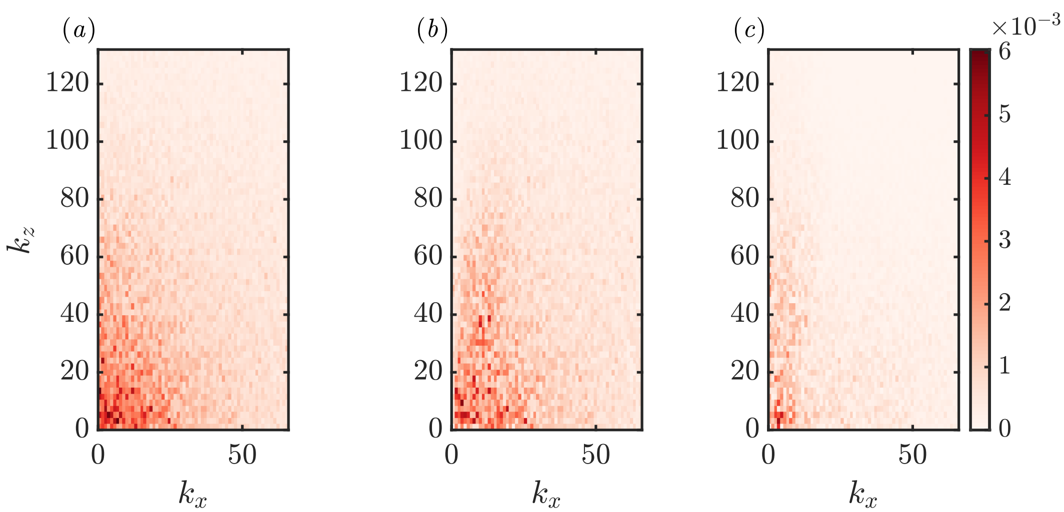

Figure 4.18: $\frac{1}{N_x N_z}\int_0^2 |\hat{\mathbf{v}}|^2 dy$ spectra of wake field for (a) data, (b) reconstruction, and (c) model.

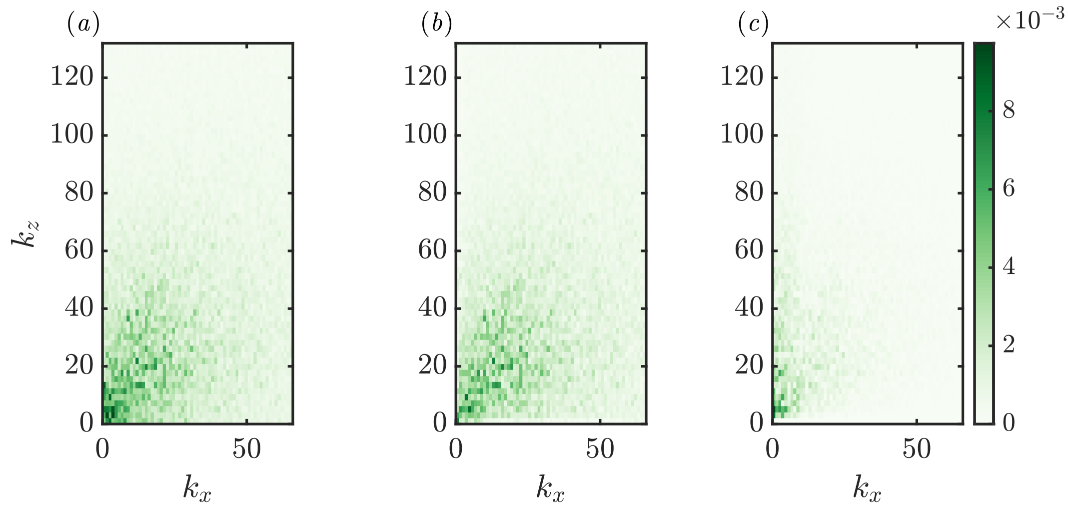

Figure 4.19: $\frac{1}{N_x N_z}\int_0^2 |\hat{\mathbf{w}}|^2 dy$ spectra of wake field for (a) data, (b) reconstruction, and (c) model.

4.7 Summary and future work

In this chapter, resolvent analysis with volume penalization (RAVP) is developed for a channel flow over multiscale roughness with a drag-normalized, Reynolds-decomposed treatment of the volume penalization term. RAVP produces a modal basis that improves the description of the roughness sublayer turbulence at low rank, and a linear model for the weights that predict the wake field response to the Fourier modes of the surface roughness. This makes the RAVP model readily applicable to multiscale, k-type roughness geometries, since it can be evaluated cheaply on a wavenumber-by-wavenumber basis. The model is used in a channel flow over sand grain roughness at $Re_\tau = 1745$ and compared against DNS results. RAVP demonstrates that a linear model ansatz for the weights can be reasonably effective at predicting wake field fluctuations and dispersive stresses over a multiscale roughness geometry.

RAVP provides reasonable predictions of roughness sublayer fluctuations at low computational cost. While simulations require a fine grid resolution to obtain converged results, the actual flow features in the wake field occur on large spatial scales, and can be captured with fewer wave numbers. For the analysis presented in this chapter, RAVP is computed over a small grid of $(N_x, N_z) = (64, 128)$ wave numbers, on a 200 point Chebyshev grid, giving $64 \times 128 \times 200 = 1.6 \times 10^6$ degrees of freedom. This is compared with datasets simulated in a $(N_x, N_y, N_z) = (1024, 530, 1024)$ averaged over ≈ 100 snapshots, for 5.5×10^{10} degrees of freedom. This gives a 10,000× model order reduction. Furthermore, since RAVP can be run in a wavenumber-by-wavenumber fashion, the memory requirements of RAVP are much lower than for a DNS or LES simulation. Practically, the results presented for RAVP in this chapter can be run in around 20 minutes on a laptop, while fully resolved simulations and post-processing take hours to days on a high performance computing cluster.

RAVP provides a physics-based modeling paradigm that predicts the spatially-varying sensitivity of the turbulent fluctuations to roughness features, using the linear amplification of the resolvent operator and a forcing corresponding to the roughness geometry. This differs from other modeling approaches in the literature that seek to relate surface statistics and spectra to mean flow parameters, and do not predict the sensitivity of the fluctuations to the surface roughness. The model predicts the shear dispersive stress $\langle \tilde{u}\tilde{v} \rangle_s$, which is not addressed in previous modeling efforts and is important for the momentum balance in a channel flow.

One possible avenue for future study is using RAVP to determine which roughness features contribute most to the turbulent flow response. By studying the linear amplification to the resolvent operator and the roughness forcing, the wave numbers corresponding to the most energetic flow response modes can be ranked. This ranking, based on the modeled turbulent flow response, is different than ranking the surface roughness modes by amplitude as in Ch. 3. Then, it should be possible to define a minimal flow response composed of a subset of energetic flow response modes, and study the corresponding minimal roughness containing only those wave numbers. Trends in the wave numbers and the most significant roughness features that contribute to the flow response could be identified using an RAVP-based approach. It may also be possible to visualize the important roughness features by studying the isosurfaces of temporally averaged flow response as in Ch. 3.

Future work also includes improving and extending the predictive abilities of the model. Since the model underestimates the activation of higher wave numbers in the wake field, it is potentially useful to study the harmonic forcing of wake field modes by roughness modes at lower wave numbers to determine its importance and potential for modeling using the $\widehat{\tilde{D}\tilde{\mathbf{u}}}$ term contained in $\hat{\mathbf{d}}$. This might also suggest investigating whether harmonic resolvent analysis, which solves for the velocity components at particular wave numbers and harmonics simultaneously, might be used to handle this term. Alternatively, it is possible that the nonlinear term $\hat{\mathbf{f}}$ contributes significantly and needs to be modeled. It would also be useful to study whether the overestimation of the magnitude of small wake field modes can be improved, by modifying the treatment of the wall location or some improved modeling approach that handles the high linear amplification of long wavelength modes in resolvent analysis. Also, it would be useful to study how RAVP can model convecting fluctuations. This requires the development of a modeling treatment of the $\widehat{\tilde{D}\mathbf{u}'}$ term contained in $\hat{\mathbf{d}}$, which might also involve harmonic resolvent analysis.

Another important aspect for future work is to characterize the performance of this model for other roughness geometries and at other Reynolds numbers. This model is expected to perform well for a k-type roughness geometry where $k \ll \delta$, so such geometries are natural candidates for testing.

In addition, an extension to handle heterogeneous roughness, such as a configuration of rough patches, may be possible. By employing a windowed analysis, RAVP may be able to predict the roughness sublayer fluctuations over the roughness patches. Over the intervening smooth wall patches, RAVP reverts to the standard resolvent analysis when appropriately windowed. Since motions that describe the transitional effects between the smooth and rough patches occur at larger scales than the roughness sublayer, modeling these motions requires an extension to the present work or the prescription of an outer layer solution as in WMLES.

The model should also be tested for other Reynolds numbers, where a key consideration is to define a grid that captures the spatial scales of the roughness sublayer, which are set by the roughness geometry. Finally, the RAVP methodology should be developed and evaluated for other canonical flows, such as pipe and boundary layer flows.

Chapter 5

MODELING THE ROUGH WALL MEAN FLOW USING RESOLVENT ANALYSIS

5.1 Introduction

Previously, Ch. 3 and 4 focused on modeling roughness sublayer fluctuations, with the smooth or rough wall spatiotemporal mean flow profile as an input. In engineering applications, the quantities of interest are often related to the mean flow, such as the Hama roughness function ΔU^+, equivalent sand grain roughness k_s^+, or the mean flow profile shape itself. In this chapter, a physics-based model is developed for predicting the rough wall mean flow profile in a channel, given only a scan of the surface geometry and a desired bulk Reynolds number. The mean flow model utilizes resolvent analysis with volume penalization (RAVP) developed in Chapter 4 and a physically-informed eddy viscosity treatment to link the drag force, dispersive stress, and stochastic stress to the shape of the mean flow profile. This allows the model to solve for the rough wall mean flow profile and friction Reynolds number iteratively, beginning with smooth wall estimates of the mean flow and friction Reynolds number at the desired bulk Reynolds number. Along the way, the drag force, dispersive stress, and stochastic stresses are also modeled, so this modeling methodology captures aspects of the sensitivity of the spatially-varying and mean turbulent flow to a given roughness geometry. In a sense, this model presents a simple method for closing the loop in resolvent analysis, utilizing the link between the mean profile shape and the dispersive stresses and drag force encoded in RAVP to converge on the mean flow profile over the roughness geometry. The model is demonstrated to work well for the sand grain roughness given reasonable estimates of the model parameters.

5.2 Comparing the smooth and rough wall mean momentum balances

The shape of the mean velocity profile $\langle \overline{u} \rangle (y)$ in a channel flow is a consequence of the mean momentum balance. In the case of a smooth wall channel, the Reynolds stress and mean flow gradient sum to the total stress. With velocity scaled in inner units and spatial variables scaled in outer units, this equation is

$$\frac{d}{dy}\left[\frac{1}{Re_\tau}\frac{d\langle \overline{u} \rangle_s}{dy} - \left\langle \overline{u'v'} \right\rangle\right] = -1. \tag{5.1}$$

To close this equation, the Reynolds stress is often related to the mean flow profile with a eddy viscosity profile $\nu_T(y)$

$$\left\langle \overline{u'v'} \right\rangle = -\frac{\nu_T}{Re_\tau} \frac{d \langle \overline{u} \rangle_s}{dy} \tag{5.2}$$

so that equation 5.1 can now be solved for the mean flow profile.

The rough wall case

Adding surface roughness changes the mean flow by adding and changing terms in the mean momentum balance, written in terms of superficial averages,

$$\frac{d}{dy}\left[\frac{1}{Re_\tau}\frac{d\langle \overline{u}\rangle_s}{dy} - \left\langle \overline{u'v'} \right\rangle_s - \langle \tilde{u}\tilde{v} \rangle_s \right] + f = -1. \tag{5.3}$$

A drag force f now appears, which represents the plane-average of viscous and pressure forces on the roughness elements. The dispersive stress $\langle \tilde{u}\tilde{v} \rangle_s$ also appears due to the wake field fluctuations. Figure 5.1(a) plots the terms in the mean momentum balance for the smooth wall mean modeled using a Cess eddy viscosity with parameters $A = 25.4$ and $\kappa = 0.426$, while in Figure 5.1(b) the rough wall balance calculated from the velocity and pseudopressure using the methods outlined in Sec. 2.6 for the DNS simulation at $Re_\tau = 1745$ is plotted. In the rough wall

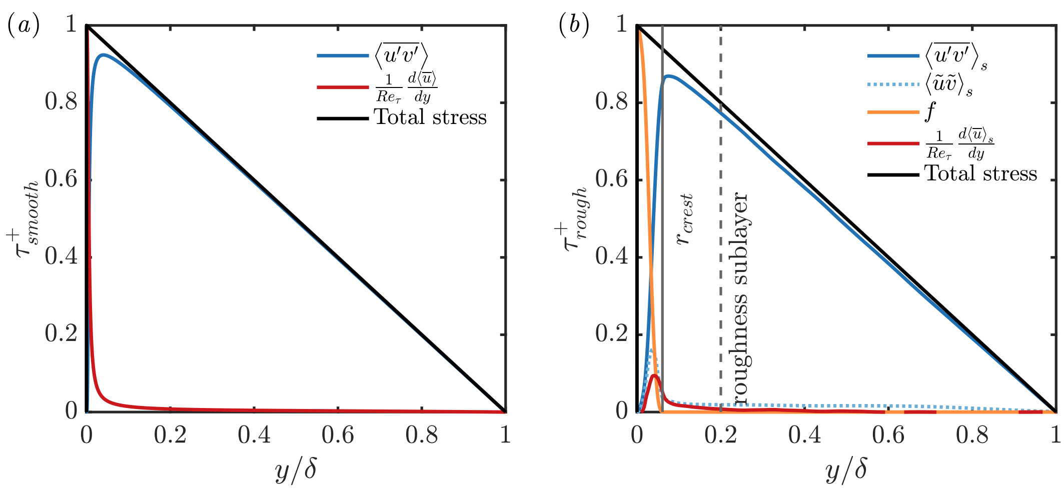

Figure 5.1: (a) Smooth wall mean momentum balance. (b) Rough wall mean momentum balance for sand grain DNS data at $Re_\tau = 1745$.

data, the stochastic stress $\left\langle \overline{u'v'} \right\rangle_s$ resembles the smooth wall Reynolds stress above outer region, but decreases rapidly beneath the roughness crest where the drag force dominates the stress balance. The stochastic stress is also attenuated particularly up until approximately $y/\delta \approx 0.4$. The roughness sublayer is classically understood to reach to roughly $y/\delta = 3k - 5k$, which is $y/\delta \approx 0.12$ to 0.2. The attenuation above $y/\delta \approx 0.2$ may simply indicate that roughness effects penetrate slightly higher before dissipating in this flow, or that perhaps additional averaging time might be required to converge the dispersive and stochastic stresses, since the dispersive stresses are small above the roughness sublayer.

In Figure 5.2, the eddy viscosity profiles which relate the mean flow to the Reynolds stress in the smooth wall case and the stochastic stress in the rough wall data are compared, where ν_T is as used in Eq. 5.2 and the rough wall eddy viscosity ν_{T_r} corresponds to the form

$$\left\langle \overline{u'v'} \right\rangle_s = -\frac{\nu_{T_r}}{Re_\tau} \frac{d\left\langle \overline{u} \right\rangle_s}{dy}. \tag{5.4}$$

The rough wall eddy viscosity is less than the smooth wall eddy viscosity within

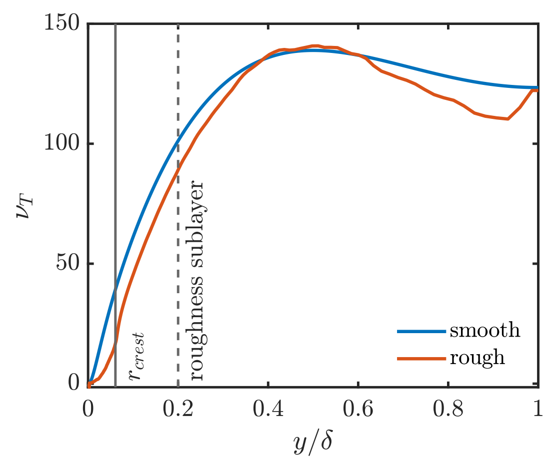

Figure 5.2: Eddy viscosity for smooth and rough wall at $Re_\tau = 1745$.

the roughness sublayer and slightly above. The profiles then match reasonably well, before diverging again near the channel centerline, where it is possible that, due to the small values of $\frac{d\langle \overline{u} \rangle_s}{dy}$ and possible discrepancy in the dispersive stress data, the rough wall eddy viscosity profile may be subject to error.

This suggests a possible model form for the rough wall eddy viscosity ν_{T_r} could be an attenuation of the smooth wall eddy viscosity in the roughness sublayer, which will be implemented in the model.

5.3 Closing the rough wall mean momentum balance with RAVP

To solve for the rough wall mean flow profile, the roughness-induced changes in the mean momentum balance must be taken into account and all terms must be related to the mean flow. The value of RAVP from Ch. 4 in this context is to provide relations between the mean flow and the drag and dispersive stress terms in the momentum balance. This amounts to writing the rough wall mean flow model as

$$\frac{d}{dy}\left[\frac{1}{Re_\tau}\frac{d\left\langle\overline{u}\right\rangle_s}{dy}-\mathcal{S}(Re_\tau,k,\left\langle\overline{u}\right\rangle_s)-\mathscr{D}(\left\langle\overline{u}\right\rangle_s,\varphi,\mathcal{K})\right]+\mathscr{F}(\left\langle\overline{u}\right\rangle_s,\varphi)=-1, \quad (5.5)$$

where

$$\begin{aligned} f &= \mathscr{F}(\left\langle\overline{u}\right\rangle_s,\varphi) \\ \left\langle\tilde{u}\tilde{v}\right\rangle_s &= \mathscr{D}(\left\langle\overline{u}\right\rangle_s,\varphi,\mathcal{K}) \\ \left\langle\overline{u'v'}\right\rangle &= \mathcal{S}(Re_\tau,k,\left\langle\overline{u}\right\rangle_s). \end{aligned} \quad (5.6)$$

Drag term modeling using volume penalization term

The drag term is modeled based on the mean momentum forcing term from RAVP,

$$f=\mathscr{F}(\left\langle\overline{u}\right\rangle_s,\varphi)=-\left\langle D\right\rangle\left\langle\overline{u}\right\rangle_s \quad (5.7)$$

where $D=D_{max}(1-\varphi)$ and D_{max} is closed by the condition

$$\int_0^1\left\langle D\right\rangle\left\langle\overline{u}\right\rangle_s dy=1, \quad (5.8)$$

since the drag term integral must approach 1 in inner units, as developed in Section 4.2.

This term can be cheaply evaluated given only the mean profile, without needing to actually evaluate RAVP.

Dispersive stress modeling using RAVP

For a given mean flow profile, roughness geometry, and set of wave numbers $\mathcal{K}$, RAVP can be evaluated to model $\tilde{u}$, $\tilde{v}$, and $\tilde{w}$, and therefore $\left\langle\tilde{u}\tilde{v}\right\rangle$. The RAVP function for the dispersive stress is denoted $\check{\mathscr{D}}$. Depending on the wave number choice $\mathcal{K}$, it is possible that the dispersive stress is underestimated, so a multiplicative scaling factor S is also defined. Then, the dispersive stress is modeled as,

$$\left\langle\tilde{u}\tilde{v}\right\rangle=\mathscr{D}(\left\langle\overline{u}\right\rangle_s,\varphi,\mathcal{K}), \quad (5.9)$$

where

$$\mathscr{D}(\left\langle\overline{u}\right\rangle_s,\varphi,\mathcal{K})=S\check{\mathscr{D}}(\left\langle\overline{u}\right\rangle_s,\varphi,\mathcal{K}). \quad (5.10)$$

Stochastic stress modeling via eddy viscosity

The stochastic stress $\left\langle\overline{u'v'}\right\rangle$ is modeled in terms of the mean flow profile $\left\langle\overline{u}\right\rangle_s$, Re_τ, and an empirical eddy viscosity profile ν_{T_r} which is adjusted for the presence of the roughness based on the shape of the drag force f modeled as described in Sec. 5.3,

$$\left\langle \overline{u'v'} \right\rangle = \mathcal{S}(Re_\tau, k, \langle \overline{u} \rangle_s) = \frac{\nu_{T_r}(f; Re_\tau)}{Re_\tau} \frac{d \langle \overline{u} \rangle_s}{dy}. \tag{5.11}$$

The eddy viscosity profile ν_T is computed using the Cess model with parameters $\kappa = 0.426$ and $A = 25.4$ which were chosen based on a mean flow profile at $Re_\tau = 2000$ as in Del Álamo and Jiménez, 2009,

$$\nu_T(y) = \frac{\nu}{2} \left[1 + \frac{\kappa^2 Re_\tau^2}{9} \left(1 - y^2\right)^2 \left(1 + 2y^2\right)^2 \left(1 - \exp\left[(|y| - 1) \frac{Re_\tau}{A} \right] \right)^2 \right]^{1/2} + \frac{\nu}{2}. \tag{5.12}$$

Then, the rough wall eddy viscosity profile is modeled as

$$\nu_{T_r} = (1 - \zeta(f))\nu_T, \tag{5.13}$$

where $\zeta(f)$ is a piecewise continuous function which attenuates the smooth wall eddy viscosity to model the rough wall eddy viscosity. $\zeta(f)$ consists of Cauchy functions which are normalized such that their peak values are 1 and centered at $y = 0$ and 2. The extents of the Cauchy functions are determined based on the shape of the drag force f.

First, a normalized Cauchy function $\hat{g}$ is fitted to the drag force f using a least-squares approach. The normalized Cauchy function is of the form

$$\hat{g}(y; y_0, \gamma) = \frac{1}{1 + \left(\frac{y - y_0}{\hat{\gamma}}\right)^2}, \tag{5.14}$$

where y_0 denotes the peak location, and γ is the scale parameter which specifies the half-width at half-maximum of the normalized Cauchy function. Essentially, γ sets the wall-normal presence of the normalized Cauchy function. To model the attenuation of the eddy viscosity above the roughness itself, a new normalized Cauchy function with a larger scale parameter is defined

$$g(y; y_0, C\gamma) = \frac{1}{1 + \left(\frac{y - y_0}{C\gamma}\right)^2}, \tag{5.15}$$

where a value of $C = 3.48$ is found to be suitable for describing the behavior of the rough wall eddy viscosity. Then, $\hat{\zeta}(f)$ is defined as

$$\zeta(y; f) = \begin{cases} g(y; 0, C\gamma) & \text{for } 0 \leq y < 1 \\ g(y; 2, C\gamma) & \text{for } 1 \leq y \leq 2. \end{cases} \tag{5.16}$$

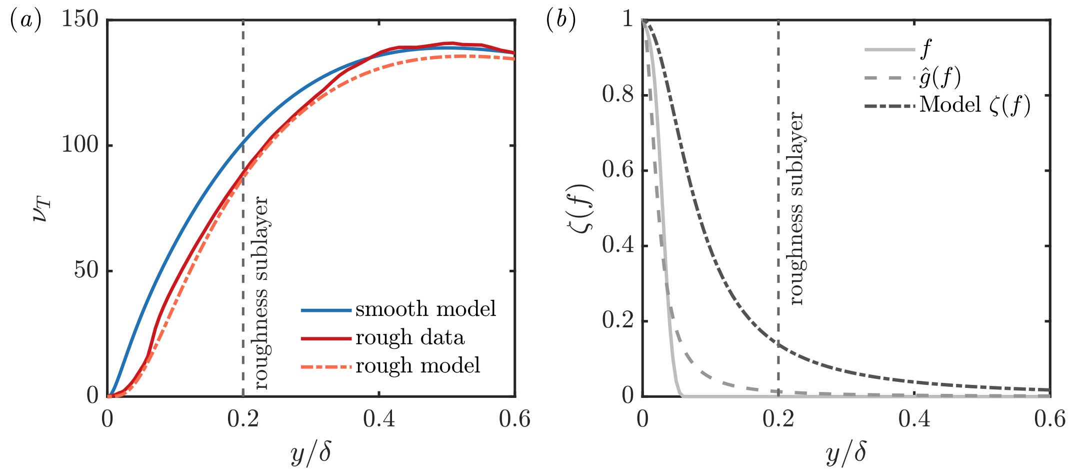

Figure 5.3: (a) Eddy viscosity profiles plotted for $Re_\tau = 1745$ for the smooth wall, rough wall data, and rough wall model, (b) Attenuation function ζ for $C = 3.48$.

$\hat{\zeta}(f)$ is defined on both sides because the same roughness is imposed on both the top and bottom of the channel. This formulation opens the possibility of applying a different roughness on the top and bottom walls, but this is not explored in this work.

The Cauchy function is chosen because it captures the attenuation of the eddy viscosity observed in the data well. The dependence on the shape of the drag force is also desirable, as the eddy viscosity attenuation should be such that the stochastic stress is present only where the drag force is weak. A comparison between the eddy viscosity profiles from the model and data is given in Figure 5.3(a) for $Re_\tau = 1745$. The model replicates the attenuation beneath the roughness crest and achieves similar peak magnitude at roughly $y/\delta = 0.5$ with respect to the data. In Figure 5.3(b), the attenuation function used is plotted.

5.4 A numerical method for solving the rough wall mean flow model iteratively for a given bulk flow

The mean flow model equation can then be written

$$\frac{d}{dy}\left[(1+\nu_{T_r})\frac{d}{dy} - Re_\tau \langle D \rangle_s\right] \langle \overline{u} \rangle_s = -Re_\tau + Re_\tau \frac{d}{dy}\mathscr{D}(\langle \overline{u} \rangle_s, \varphi, \mathcal{K}). \qquad (5.17)$$

In this form, the equation is amenable to a numerical solution. Since the dispersive term must be solved using RAVP given the mean, the solution for the mean flow is now iterative. The equations are discretized and solved using Chebyshev differentiation matrices Weideman and Reddy, 2000.

The iterative scheme is laid out in Figure 5.4. The inputs for the analysis are the

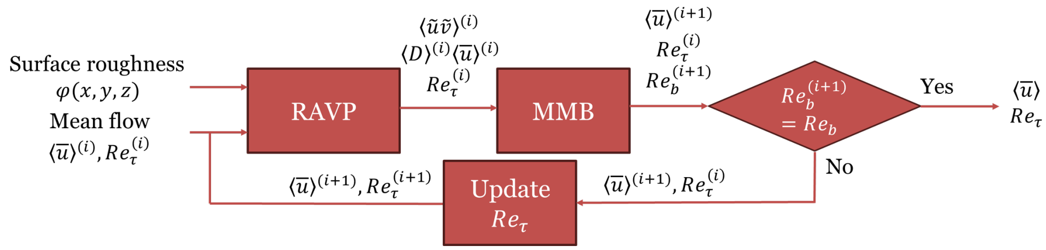

Figure 5.4: Full workflow for rough wall mean flow model.

surface roughness geometry and an initial guess for the inner-scaled mean flow profile $\langle \overline{u} \rangle_s^{(i)}$ at the desired bulk Reynolds number $Re_b^{desired}$. The smooth wall mean profile for that Re_b is a reasonable starting point. Those are fed into RAVP, which gives predictions for the drag force and dispersive stress. Then, the mean momentum balance is solved to give a new inner-scaled mean profile, $\langle \overline{u} \rangle_s^{(i+1)}$. From this mean profile, $u_\tau^{(i+1)}$ and a new $Re_b^{(i+1)}$ are computed using

$$\begin{aligned} u_\tau^{(i+1)} &= \frac{1}{\int_0^1 \langle \overline{u} \rangle_s^{(i+1)}\, dy} \\ Re_b^{(i+1)} &= \frac{Re_\tau^{(i)}}{u_\tau^{(i+1)}}. \end{aligned} \tag{5.18}$$

To determine whether the loop needs to continue, the resulting bulk Reynolds number is compared with the desired bulk Reynolds number. This loop finishing condition is stated as

$$\frac{\left| Re_b^{(i+1)} - Re_b^{desired} \right|}{Re_b^{desired}} < \epsilon \tag{5.19}$$

for some choice of ϵ. If the condition is not met, Re_τ is updated using

$$Re_\tau^{(i+1)} = Re_\tau^{(i)} + \left(Re_b^{(i+1)} - Re_b^{desired} \right) u_\tau^{(i+1)}. \tag{5.20}$$

The loop repeats until the finishing condition is met.

Reduced models implemented

Since $O(100)$ iterations are usually required to converge the mean, and RAVP can take $O(10)$ minutes to run, the mean flow modeling framework becomes time-consuming if RAVP is evaluated to find the dispersive stress at every iteration. Two reduced versions of the full mean flow model are presented.

The first reduced model is a proof-of-concept that uses the data value of the dispersive stress. This model is reasonable to use if the dispersive stress can already be modeled for a given roughness, either independently or as combined with the stochastic stress using the eddy viscosity. This model is cheap, as it only updates the drag term from RAVP and the eddy viscosity on each iteration. It runs in $O(10)$ seconds.

The second reduced model evaluates RAVP at the second iteration, and every N_{eval} iterations. The dispersive stress is initialized as 0. Starting the evaluation of RAVP for the dispersive stress at the second iteration allows the mean profile shape to be somewhat corrected by the drag term and adjusted eddy viscosity first, so that the estimate for the dispersive stress is more realistic. Evaluating every N_{eval} iterations reduces cost while still encoding the relationship between the mean flow profile and dispersive stress in the model results. For $N_{eval} \approx 40$, the model runs in $O(1)$ hour.

Estimation of ΔU^+ and k_s^+

To compute ΔU^+ and k_s^+, the values of the mean profile $\langle \overline{u} \rangle_s$ over $y^+ \in [3Re_\tau^{0.5}, 0.15Re_\tau]$ are taken, which are suggested conservative limits for the extent of the logarithmic layer (Marusic, Monty, et al., 2013). For this calculation, $\langle \overline{u} \rangle_s$ is given on coordinates $y/\delta \in [-0.032, 2.032]$ to account for the roughness blockage. Then, the values of ΔU^+ across the logarithmic layer are computed by

$$\Delta U^+(y^+) = \frac{1}{\kappa} \ln y^+ + B - \langle \overline{u} \rangle_s \quad \text{for} \quad y^+ \in [3Re_\tau^{0.5}, 0.15Re_\tau]. \tag{5.21}$$

A final value for ΔU^+ is given by taking the median of $\Delta U^+(y)$. It is also possible to take the mean, and this does not have a substantial effect on the results.

To estimate k_s^+, the relationship

$$k_s^+ = \exp\left[\kappa(\Delta U^+ - B + D)\right] \tag{5.22}$$

is used, where $B = 5$ is the smooth wall constant and $\kappa = 0.39$ is the von Karman constant. For the sand grain roughness, $k_s \approx 1.6k$. For this relationship to hold true, $D = 7.9$ is found to be a good value; it is similar to $D = 8.5$, which is common in the literature. This value of D is taken for all models shown in this chapter.

5.5 Dataset considered and parameters of analysis

The sand grain roughness at $Re_\tau = 1745$ is used for this analysis. The wave number set $\mathcal{K}$ chosen is the same low pass filtered set as in Chap. 4,

$$\begin{aligned} \frac{k_x}{\Delta k_x} &\in [0, 64] \\ \frac{k_z}{\Delta k_z} &\in [-64, 64] \end{aligned} \tag{5.23}$$

where $\Delta k_x = 1.05$ and $\Delta k_z = 2.09$. From a total of $N_x \times N_z = 512 \times 256$ wave numbers, 64×128 wave numbers are considered in this analysis. The number of Chebyshev points considered is $N_y = 200$. The volume fraction representation of the sand grain roughness is mapped to the Chebyshev grid using Eq. 3.2.

5.6 Proof of concept using fixed dispersive stress

In this section, the iterative framework is tested using the data value of the dispersive stress. In this test, the parameters $C = 3.48$, $S = 1$, and $\epsilon = 0.00001$ are taken. This model runs in 260 iterations, taking approximately 13 seconds on a laptop.

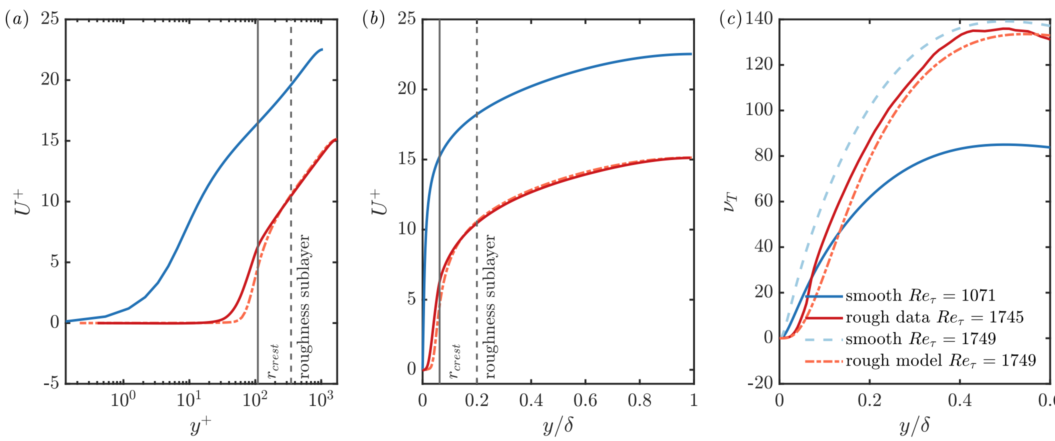

Figure 5.5: The mean flow prediction for the fixed dispersive stress cases in (a) inner and (b) outer units, and the (c) eddy viscosity profile.

Figure 5.5 shows the prediction of the mean flow and eddy viscosity profiles. The mean flow profile is well predicted, though with a discrepancy close to $y^+ = 100$. This error is particularly noticeable when plotted with inner-scaled spatial units, but is less noticeable when plotted with outer spatial units. The modeled eddy viscosity compares qualitatively well with the data eddy viscosity, though with regions of slight underestimation in the roughness sublayer and outer regions.

Figure 5.6 compares the terms in the mean momentum balance from the model and data. This image shows that the mean flow gradient is underestimated in a region below $y/\delta \approx 0.045$, and slightly overestimated above this region, which leads to the discrepancy in the mean profile shape near $y^+ = 100$. The drag force is also overestimated beneath the roughness crest, corresponding to the error in the mean profile. The stochastic stress is underestimated where the drag force is overestimated because of the form of the eddy viscosity attenuation based on the drag force, which helps the model still perform well in predicting the right logarithmic layer profile.

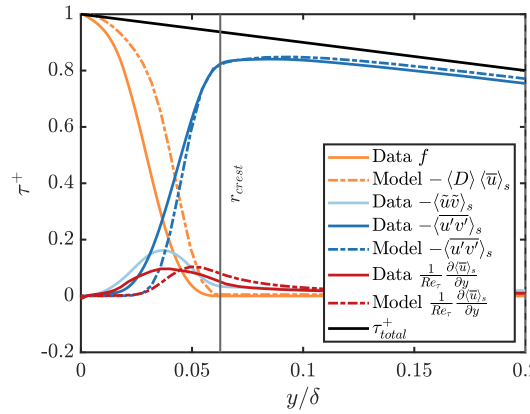

Figure 5.6: Stress balance for the fixed dispersive stress case.

	Data	**Model**	**Error**
Re_b	21,400	21,400	0.007%
Re_τ	1745	1749	0.2%
u_τ	0.0814	0.0817	0.4%
ΔU^+	9.2	9.3	0.5%
k_s^+	112	116	2%

Table 5.1: Comparison of data and model results for the fixed dispersive stress case.

The roughness function ΔU^+ and k_s^+ are then calculated from the modeled mean flow. Table 5.1 summarizes those results, and the agreement between the model and data is good.

5.7 Results for mean flow model incorporating RAVP evaluation

In this section, results are presented for the mean flow model with the RAVP-modeled dispersive stress. For the model presented here, $\langle\tilde{u}\tilde{v}\rangle_s$ is initialized as 0. The modeling parameters $C = 3.48$, $S = 1$, $\epsilon = 0.0005$, and $N_{eval} = 40$ are used. Then, the drag force, dispersive stress, and stochastic stresses are iteratively estimated. The model computes 148 iterations in approximately 2 hours.

Figure 5.7 gives the final predictions of the mean flow and eddy viscosity profiles. The agreement between the data and predictions is good in inner and outer units. The predicted eddy viscosity curve underestimates the data, which occurs because the final friction Reynolds number is underestimated.

Figure 5.8 compares the terms in the mean momentum balance of the model and data. The mean flow gradient matches reasonably well, but is slightly underestimated within the roughness geometry. The dispersive stress is overestimated, due to the underestimation of the mean flow gradient causing an overestimation of D_{max} from

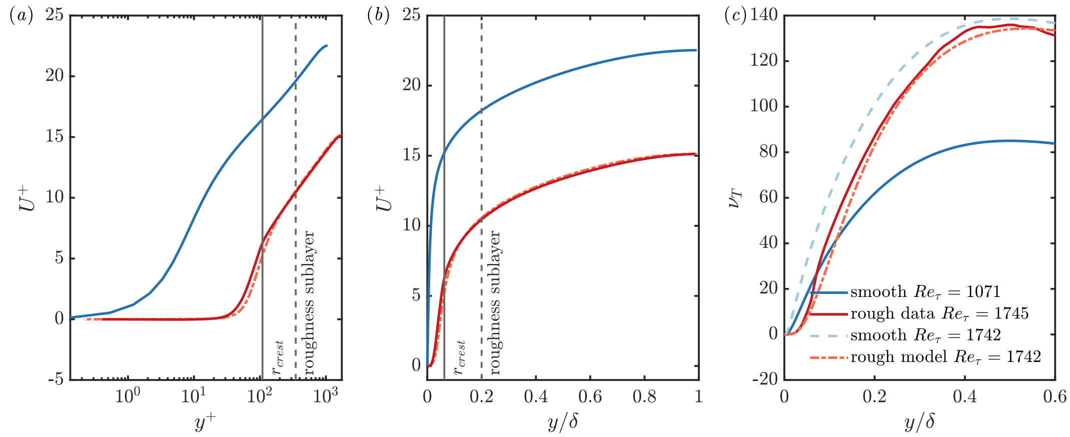

Figure 5.7: Mean flow prediction in (a) inner and (b) outer units, and the (c) predicted eddy viscosity for the model including RAVP evaluations.

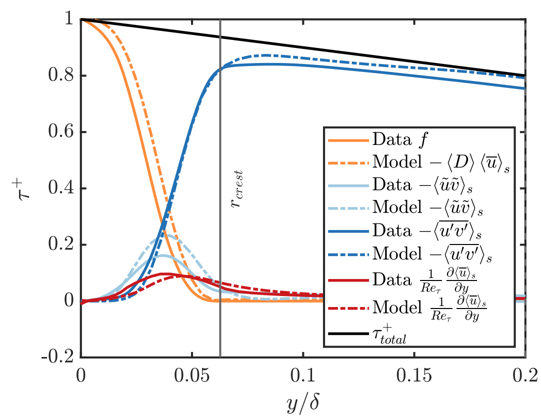

Figure 5.8: Mean flow prediction in inner and outer units for the model including RAVP evaluations.

	Data	**Model**	**Error**
Re_b	21,400	21,390	0.05%
Re_τ	1745	1742	0.2%
u_τ	0.0814	0.0814	0.03%
ΔU^+	9.2	9.3	0.2%
k_s^+	112	113	0.7%

Table 5.2: Comparison of data and results of model incorporating RAVP evaluations.

the integral condition of Eq. 5.8. The drag force is slightly overestimated, which is characteristic of the RAVP analysis. The stochastic stress agrees well with the data.

Table 5.2 summarizes the results of the iteration. The error in the estimates is reasonably small,

On sensitivity of the RAVP-estimated dispersive stress to the mean flow

One important observation made while evaluating the mean flow model is that the RAVP estimate of the dispersive stress is highly sensitive to the mean flow gradient. This is because the D_{max} parameter that controls the magnitude of the volume penalization term is set by an integral condition based on the mean flow profile shape and the roughness.

This has consequences for the convergence behavior of the mean flow model if the mean flow gradient is during any iteration underestimated within the roughness. This is not a problem at the outset because the mean flow profile from the smooth wall case used to initialize the method overestimates the mean flow gradient. However, if the mean flow gradient is underestimated during an iteration, the D_{max} parameter increases, which increases the RAVP-predicted dispersive stress magnitude and the fullness of the drag force profile (effectively, an overestimation at any given y-height). When evaluating the momentum balance, the overestimation of these stresses further decreases the resulting mean flow gradient. This results in the method moving farther away from the solution.

This behavior is mitigated somewhat by increasing ϵ so the method does not iterate to a point where the mean flow gradient is underestimated, and this measure has been taken for the results presented in Sec. 5.7.

5.8 Discussion and future work

In this section, an iterative mean flow modeling framework is developed to predict mean flow quantities for a given bulk flow in a channel with surface roughness, which utilizes RAVP and a roughness-modified eddy viscosity profile to close the terms in the mean momentum balance. The model requires only the bulk Reynolds number and the surface geometry as inputs, provides a starting point for the iteration as the corresponding smooth wall profile and friction Reynolds number, and iteratively solves for the rough wall mean flow and friction Reynolds number. Two computationally efficient reductions of that framework are tested, one with a fixed dispersive stress and one which evaluates RAVP for the dispersive stress every N_{eval} iterations. For physically justifiable choices of the model parameters, both models deliver reasonable estimates for the mean flow profile shape, drag force, Hama roughness function, and equivalent sand grain roughness. The model that evaluates RAVP also provides predictions for the wake field fluctuations and dispersive stresses. In this way, the developed approach models the spatially-varying and mean turbulent flow response to a given roughness geometry in a channel flow, providing more information than is provided by models that link the surface statistics and spectra to aspects of the drag response only.

One major challenge of the method is the computational time associated with evaluating RAVP for the dispersive term. To mitigate this, results are given for the case where the dispersive term is evaluated only once every 40 iterations, where O(100) iterations are run. This amount is sufficient to recover the mean flow profile, since the drag force term dominates the effect on the mean flow near the wall. Parallelizing the wave number by wave number evaluation of RAVP could also speed up the process considerably and lead to time savings.

Another important area of work is towards improving the convergence properties of the method as discussed in 5.7. The condition where the mean flow gradient is underestimated during an iteration results in the method driving away from the solution. A modification to the treatment of D_{max} that prevents the overestimation of the dispersive stress magnitude, or another algorithmic improvement is desirable.

An important avenue for further investigation is improving the modeling of the stochastic stress contribution. The eddy viscosity modeling used here has virtue in its simplicity and ease of implementation. However, the model is highly sensitive to the shape of the eddy viscosity profile and how it is attenuated near the roughness. A more general method may involve improvements to the eddy viscosity modeling to better represent the data, or using RAVP to model the effects on the convecting fluctuations, i.e. solving for the stochastic stress or its modulation in some way.

The ideas presented here complement other existing works in the literature for closing the loop to estimate the mean and fluctuations in resolvent analysis. For instance, the work of Rosenberg and McKeon, 2019 demonstrates that by modeling the self-interaction of one resolvent mode description of an ECS, it is possible to iteratively estimate the 2D turbulent mean and the resolvent mode representation of the ECS starting from a laminar solution. The present model develops a simple closure for the flow over sand grain roughness that incorporates the self-interaction of the wake field fluctuations. To model this flow demands additional modeling assumptions, including an eddy viscosity formulation which is less elegant than capturing the self-interaction of stochastic modes. Nonetheless, the iterative process presented recovers the mean and dispersive stresses, which is significant because this means that the wake field fluctuations were predicted using RAVP without having to supply the mean a priori.

Chapter 6

DATA-DRIVEN REDUCED ORDER MODEL OF TURBULENT FLUCTUATIONS USING RESOLVENT ANALYSIS FOR WALL-MODELED LES

6.1 Introduction

Fully-resolved turbulence contains a huge range of scales of motion, and can only be resolved in physical space by sampling at a high frequency over long time on a large computational grid with fine spatial resolution. This makes simulations expensive, and the storage and analysis of turbulence data challenging. In particular, spatiotemporal (modal) representations of turbulence calculated using techniques such as SPOD have many degrees of freedom, and many modes must still be retained even in a reduced-order representation to preserve the statistics and characteristics of the original data.

This chapter explores whether there is a way to leverage ideas about the structure of wall-bounded turbulence to help reduce the dimensionality of spatiotemporal (modal) representations of turbulence, while still preserving the essential characteristics of the original data. Such classical ideas include the attached eddy hypothesis of Townsend, 1976, who painted a picture of turbulence in the logarithmic layer as composed of hierarchies of geometrically self-similar eddies with inversely-varying population density.

In this chapter, data-driven methods for coarse-graining modal representations of turbulence in (k_x, k_z, ω)-space are developed. These methods are different than the coarse-graining approach Grinstein et al., 2025 takes to coarse-grain the governing equations, the NSE. The presented method rebins already-existing, high-dimensional datasets to give reduced order spatiotemporal representations of turbulence. The presented methods take high-dimensional data from a highly resolved turbulent channel flow simulation at moderate Reynolds number, and output coarse-grained modal representations which reproduce the statistics and qualitative characteristics, but with a large reduction in the number of modes required. Selection criteria based on the magnitude of the modes and their wave speeds are developed, so that modal representations that capture dynamic inner and outer layer motions can be isolated. The data-driven coarse-grained representations are used to weight resolvent mode bases, which are shown to represent the data reasonably well. Then, the effect of applying wave number scalings to the coarse-grained representations to predict inner region turbulence at higher Reynolds number is explored.

Aspects of the feasibility and efficacy of using these near-wall representations in wall-modeled LES (WMLES) are investigated, and the impact on the turbulent flow statistics is highlighted by results obtained in collaboration with Piomelli et. al.[1]It is noted that for the purposes of including modes in WMLES, the modal representation used does not need to represent a full dynamic ROM; all it needs to do is add energy to the flow where it is desirable.

6.2 General methodology for generating coarse-grained resolvent mode representations of near-wall turbulence

The coarse-graining methods presented in this chapter start by taking an SPOD on a time series of velocity fields from a highly resolved simulation of turbulent channel flow as inputs. Then, the spatiotemporal representations are coarse-grained, i.e. the energy content of the modes is redistributed into an appropriate selection of spatial frequency and temporal frequency or critical layer bins, each represented by a characteristic mode shape. From these coarse-grained representations, criteria are developed to select modes that most effectively represent fluctuations present in the inner, logarithmic, and outer regions of the flow. Then, the coarse-grained modal representation can be projected onto resolvent modes, resulting in a coarse-grained resolvent mode representation of near-wall turbulence. Furthermore, these representations can be scaled to give predictions for fluctuations at different Re_τ, and they can be inverted back into physical space. Figure 6.1 outlines the overarching structure of the method, and the subsequent subsections document the details of the data generation, SPOD averaging, coarse-graining, mode selection, projection onto resolvent modes, and wave number scaling.

[1]Data-driven and resolvent mode representations of near-wall turbulence are developed using data analysis and mode selection guidelines as developed in the present chapter by the author. The WMLES results are obtained by Piomelli et. al., who developed the numerical scheme for a wall model that incorporates the modal representations in WMLES. Hantsis also develops some empirical amplifications for modal representations. The results are presented in

- Hantsis, Z., M. J. Chan, B. J. McKeon, and U. Piomelli (2024). *Resolvent modes as the foundation for LES wall models*. 77th Annual Meeting of the Division of Fluid Dynamics, Salt Lake City, Utah. URL: Abstract
- Piomelli, U., Z. Hantsis, M. J. Chan, and B. J. McKeon (2024). *Resolvent modes as the foundation for LES wall models*. 16th World Congress on Computational Mechanics, Vancouver, Canada.

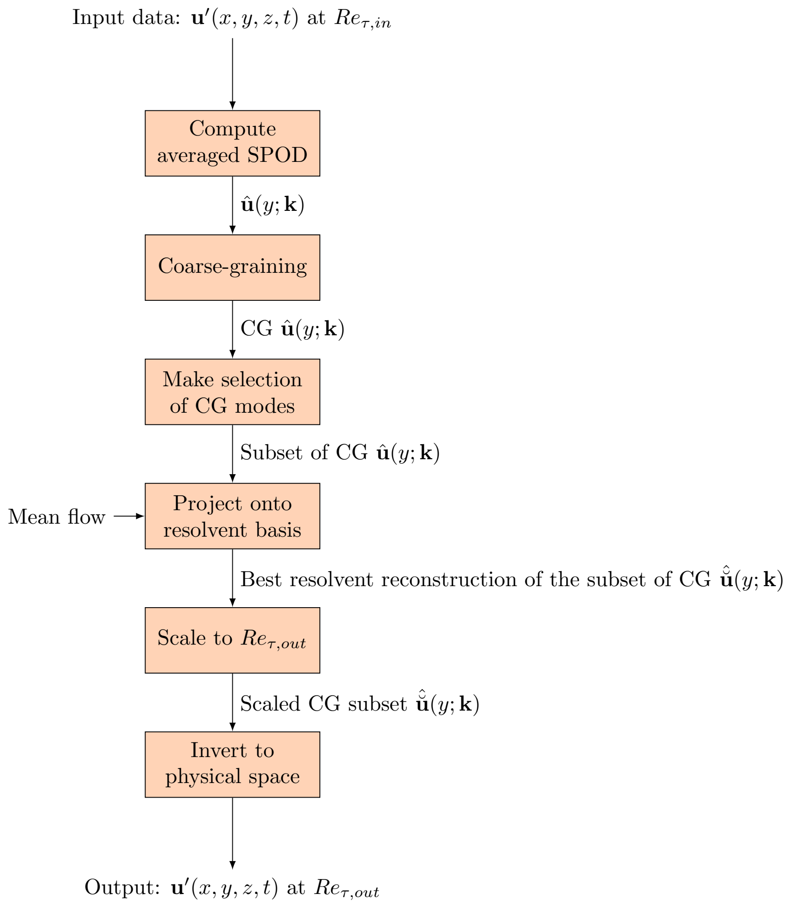

Figure 6.1: Workflow for developing coarse-grained spatiotemporal representations of turbulence using resolvent modes.

On the definition and properties of a mode

In this chapter, a spatiotemporal mode $\hat{\mathbf{u}}$ at a given wave number (k_x, k_z, ω) contains the three Fourier-transformed y-varying components of velocity, $\hat{u}$, $\hat{v}$, and $\hat{w}$ stacked in a vertical vector,

$$\hat{\mathbf{q}} = \begin{bmatrix} \hat{u} \\ \hat{v} \\ \hat{w} \end{bmatrix}. \tag{6.1}$$

Therefore, a mode embeds information about the y-varying phase and magnitude of each velocity component. The relative phase and magnitude between velocity components is fixed. Velocity modes calculated from the Fourier transform are divergence-free based on their wave number and velocity components

$$ik_x\hat{u} + \frac{d\hat{v}}{dy} + ik_z\hat{w} = 0. \tag{6.2}$$

Re_τ	L_x	L_y	L_z	N_x	N_y	N_z	Δx^+	Δy^+_{min}	Δy^+_{max}	Δz^+
1000	16δ	2δ	3δ	640	256	256	25	0.258	23.2	11.7

Table 6.1: Simulation parameters.

To maintain this favorable property, the manipulations on a mode are limited to multiplication by a complex scalar, which can set the alignment and magnitude of a mode while preserving incompressibility.

Channel flow data generation

A wall-resolved LES (WRLES) of channel flow at $Re_\tau = 1000$ is performed using the MPI-parallelized code employed by Piomelli et al (Keating et al., 2004). The filtered Navier-Stokes equations are solved using a second-order accurate central difference in space on a staggered mesh. The Vreman subgrid scale model is used. A second-order accurate semi-implicit time advancement method is used, where Crank-Nicolson is used for the wall-normal diffusive terms and low-storage third-order Runge-Kutta is applied to the remaining terms. The Poisson equation is solved using an efficient Fourier Transform solver. The simulation is run at a constant $Re_b = 20000$. The parameters of the simulation are documented in Table 6.1. 2000 snapshots of velocity data are collected, with a time interval of $\Delta t^+ = 1.5$ or $\Delta t = 0.03$.

Then, each snapshot is Fourier transformed in the streamwise and spanwise directions, so the data is passed to SPOD as a time series of y-varying data in (k_x, k_z)-space, where k_x and k_z denote the streamwise and spanwise wave numbers respectively.

Averaged SPOD

To give a spatiotemporal representation of the data, an averaged SPOD is performed on the Fourier-transformed data in space and time. The time series is broken into several windowed blocks, or realizations of the flow, each with a phase offset corresponding to the initial time of each window applied. Then, calculating SPOD gives mode shapes and expansion coefficients that best reconstruct each flow realization included in the analysis with respect to a kinetic energy norm. Finally, the expansion coefficients are averaged across realizations to give an average SPOD representation of the data. The results are given as a y-varying dataset in (k_x, k_z, ω)-space.

For each wave number, SPOD relates the original realizations of the Fourier transformed data $\hat{\mathbf{Q}} \in \mathbb{C}^{n \times n_{blk}}$, SPOD modes $\mathbf{\Phi} \in \mathbb{C}^{n \times n_{blk}}$, and matrix of expansion coefficients $\mathbf{A} \in \mathbb{C}^{n_{blk} \times n_{blk}}$,

$$\hat{\mathbf{Q}} = \mathbf{\Phi}\mathbf{A}. \tag{6.3}$$

The structure of $\mathbf{A}$ is

$$\mathbf{A} = \begin{bmatrix} a_{11} & a_{12} & \cdots & a_{1n_{blk}} \\ a_{21} & a_{22} & \cdots & a_{2n_{blk}} \\ \vdots & \vdots & \ddots & \vdots \\ a_{n_{blk}1} & a_{n_{blk}2} & \cdots & a_{n_{blk}n_{blk}} \end{bmatrix}, \tag{6.4}$$

where the a_{ij} coefficient gives the contribution of the i-th SPOD mode to the j-th realization of data. The coefficients are averaged to give a reasonable representation of all the data blocks, which is calculated as the multiplication of the root-mean-squared modulus and the average unit vector over all realizations,

$$\breve{\mathbf{A}} = \begin{bmatrix} \sqrt{\frac{1}{n_{blk}} \sum_{j=1}^{n_{blk}} |a_{1j}|^2} \frac{1}{n_{blk}} \sum_{j=1}^{n_{blk}} \frac{a_{1j}}{|a_{1j}|} \\ \sqrt{\frac{1}{n_{blk}} \sum_{j=1}^{n_{blk}} |a_{2j}|^2} \frac{1}{n_{blk}} \sum_{j=1}^{n_{blk}} \frac{a_{2j}}{|a_{2j}|} \\ \vdots \\ \sqrt{\frac{1}{n_{blk}} \sum_{j=1}^{n_{blk}} |a_{n_{blk}j}|^2} \frac{1}{n_{blk}} \sum_{j=1}^{n_{blk}} \frac{a_{n_{blk}j}}{|a_{n_{blk}j}|} \end{bmatrix}. \tag{6.5}$$

Then, an average modal representation $\hat{\breve{\mathbf{q}}} \in \mathbb{C}^n$ at a given frequency is obtained using

$$\hat{\breve{\mathbf{q}}} = \mathbf{\Phi}\breve{\mathbf{A}}. \tag{6.6}$$

A time series of 2000 snapshots is collected, with a time interval of $\Delta t^+ = 1.5$ or $\Delta t = 0.03$ in outer units. The time series covers 60 outer time units. The SPOD is carried out on 19 Hamming windows of 200 snapshots each, with an overlap of 50%. Therefore, each window is 6 outer time units long. This window is chosen so that near-wall motions are captured, and it is permissible for outer motions that have a temporal wavelength longer than 6 outer time units to be binned in the 0 frequency component.

Coarse-graining modal representations in (k_x, k_z, ω)-space

The SPOD modal representations are given in (k_x, k_z, ω)-space. To reduce the order, approximately logarithmically spaced bins are defined in (k_x, k_z, ω)-space, and each bin is represented by one mode which is amplified to preserve the streamwise velocity intensity originally contained in the bin.

The wave numbers for rebinning in (k_x, k_z, ω) are calculated by calculating logarithmically spaced wave numbers, and selecting the closest (k_x, k_z, ω) wave numbers from the original grid to define the bin edges. Only positive wave numbers $(+k_x, +k_z, +\omega)$ are considered, with Hermitian symmetry accounting for $(-k_x, -k_z, -\omega)$ and a cross flow symmetry applied when inverting back to physical space,

$$\begin{aligned}
\hat{u}(k_x, -k_z, \omega) &= \hat{u}(k_x, k_z, \omega) \\
\hat{v}(k_x, -k_z, \omega) &= \hat{v}(k_x, k_z, \omega) \\
\hat{w}(k_x, -k_z, \omega) &= -\hat{w}(k_x, k_z, \omega).
\end{aligned} \tag{6.7}$$

The axis of positive wave numbers is defined by the maximum frequency $k_{x_{max}}$, $k_{z_{max}}$, and ω_{max}, as well as the frequency resolution Δk_x, Δk_z, and $\Delta\omega$. Then, the logarithmically spaced wave numbers are computed as

$$\begin{aligned}
\breve{k}_x &= \left[k_{x_1}, k_{x_2}, \ldots, k_{x_{max}}\right], \quad k_{x_l} = k_{x_1} \cdot \left(\frac{k_{x_{max}}}{\Delta k_x}\right)^{\frac{l-1}{L-1}}, \quad \text{for } l = 1, 2, \ldots, L \\
\breve{k}_z &= \left[k_{z_1}, k_{z_2}, \ldots, k_{z_{max}}\right], \quad k_{z_m} = k_{z_1} \cdot \left(\frac{k_{z_{max}}}{\Delta k_z}\right)^{\frac{m-1}{M-1}}, \quad \text{for } m = 1, 2, \ldots, M-1 \\
\breve{\omega} &= \left[\omega_1, \omega_2, \ldots, \omega_{max}\right], \quad \omega_n = \omega_1 \cdot \left(\frac{\omega_{max}}{\Delta\omega}\right)^{\frac{n-1}{N-1}}, \quad \text{for } n = 1, 2, \ldots, N-1,
\end{aligned} \tag{6.8}$$

where $k_{x_1} = \Delta k_x$, $k_{z_1} = \Delta k_z$, and $\omega_1 = \Delta\omega$ by construction. Then, the closest values from the original k_x, k_z, and ω grids are taken to denote the bin wave numbers,

$$\begin{aligned}
\tilde{k}_{x_l} &= k_{x_i}, \quad \text{where} \quad \arg\min_i \left|k_{x_i} - \breve{k}_{x_l}\right| \\
\tilde{k}_{z_m} &= k_{z_i}, \quad \text{where} \quad \arg\min_i \left|k_{z_i} - \breve{k}_{z_m}\right| \\
\tilde{\omega}_n &= \omega_i, \quad \text{where} \quad \arg\min_i \left|\omega_i - \breve{\omega}_n\right|.
\end{aligned} \tag{6.9}$$

Then, each bin is defined by the mode calculated at its representative wave number. The bin defined by $\mathbf{k}_{bin} = (k_{x_l}, k_{z_l}, \omega_l)$ encompasses the set $\mathcal{K}$ of all wave numbers from the original (k_x, k_z, ω) axes that meet the criteria,

$$\begin{aligned}
k_x &\in (k_{x_{l-1}}, k_{x_l}] \\
k_z &\in (k_{x_{m-1}}, k_{z_m}] \\
\omega &\in (\omega_{n-1}, \omega_n].
\end{aligned} \tag{6.10}$$

Then, the mode which represents the bin is amplified by a real scalar b such that amplitude of the mode's streamwise velocity component captures the streamwise

Region	y	c^+
Inner	$y^+ < 100$	$[2, 16]$
Logarithmic	$y^+ = 100$ to $y/\delta > 0.1$	$[16, U_{cl} - 6.15]$
Outer	$y/\delta > 0.1$	$[U_{cl} - 6.15, U_{cl}]$

Table 6.2: Regions of flow delineated by wall normal height with the corresponding guidelines for convecting velocity.

energy intensity of all the modes contained in the bin. The scalar b is calculated as

$$b = \frac{\sum_{\mathbf{k}\in\mathcal{K}} \int_0^\delta |\hat{u}(\mathbf{k})|^2 dy}{\int_0^\delta |\hat{u}(\mathbf{k}_{bin})|^2}. \tag{6.11}$$

The logarithmic spacing is important because it preserves the distinction between large wavelength modes that convect at different but similar speeds to produce important near-wall motions, while binning together small wavelength modes to reduce the degrees of freedom of the modal representation. The choice to rebin using wave numbers contained in the original frequency axis is crucial because it minimizes the manipulations carried out on the retained modes to multiplication by a scalar.

Mode selection and filtering by convecting velocity

From spatiotemporal representations of turbulence, it is possible to select and extract modes that are characteristic of motions in the inner, logarithmic, and outer regions of the flow. Those regions are delineated by their wall-normal extent and the mean velocity at those wall-normal locations in Table 6.2 (Moarref, Sharma, et al., 2013). For modes to contribute to dynamic motions in a particular region of the flow, they must be energetic in that region. The amplitude of the streamwise velocity component of a mode is usually highest near its critical layer, which is the height y_{crit} where the wave speed of the mode $c = \omega/k_x$ is equal to the mean velocity. This critical layer mechanism can be described by the linear dynamics captured in the linearized Navier-Stokes operator. Therefore it is reasonable to select modes based on whether their convecting velocities are characteristic of the particular region of the flow of interest.

Selecting a mode that is only energetic in the inner region is straightforward because the wall-normal extent of the mode is compressed when its amplitude is localized in the inner region. Selecting a mode that is active in the outer region but not in the inner region is tricky because a mode that has a higher critical layer height also tends to have significant amplitude spread out over a larger wall-normal extent. These modes are representative of large scale motions that reach from the outer region into the inner region.

Even amongst modes that convect at a particular speed, some modes are more energetic than others, and it is often possible to truncate a modal representation further while capturing the statistics. Selecting modes by their integrated streamwise energy intensity within a region of the flow of interest,

$$\hat{E}_{uu}(y_1, y_2) = \int_{y_1}^{y_2} |\hat{u}|^2 dy, \tag{6.12}$$

is a reasonable choice, especially since the streamwise energy dominates the turbulent kinetic energy. However, it is also possible to select modes by shear Reynolds stress,

$$\hat{E}_{uv}(y_1, y_2) = \int_{y_1}^{y_2} Re(\hat{u}\hat{v}^*) dy, \tag{6.13}$$

or another mode quantity of interest,

$$\hat{E}_{q}(y_1, y_2) = \int_{y_1}^{y_2} \hat{q} dy. \tag{6.14}$$

A final consideration is to select modes based on the wave numbers expected to be active in the flow; motions of $\lambda_x^+ \approx 1000$ and $\lambda_z^+ \approx 100$ are characteristic of near-wall streaks, while superstructures exist in the logarithmic region of boundary layers of roughly 6δ in streamwise length.

The metric for choosing the modes can be based on what statistics are desired to be reproduced or considered important for a numerical scheme. For the scheme of Piomelli et. al, it is shown that having concentrated Reynolds shear stress in the inner layer is desirable, as it excites additional turbulent activity in the near-wall region, resulting in an increase in the inner layer peak which improves the matching of statistics from WMLES and wall-resolved simulations. From the perspective of selecting modes which best represent turbulent kinetic energy, choosing by TKE or streamwise stress, which is the bulk of TKE, works well.

Determining weights for resolvent modes using SPOD modes

Weights for resolvent modes are determined to best reconstruct the SPOD modal representations with respect to the kinetic energy norm. For each frequency, a rank M SPOD approximation is taken,

$$\hat{\mathbf{q}} = \sum_{i=1}^{M} \varphi_i \breve{a}_i. \tag{6.15}$$

Then, the best projection of the SPOD mode onto the jth resolvent mode from the SVD expansion can be found by solving

$$\chi_j = \underset{\chi_j}{\arg\min} ||\hat{\hat{\mathbf{q}}} - \sigma_j \psi_j \chi_j||_W^2, \tag{6.16}$$

where W is a matrix of grid weights. The 2-norm is used here, but other norm choices are possible. Solving this problem yields

$$\mathbf{X} = \left(\mathbf{B}^{\mathsf{H}}\mathbf{W}\mathbf{B}\right)^{-1} \mathbf{B}^{\mathsf{H}}\mathbf{W}\hat{\hat{\mathbf{q}}}, \tag{6.17}$$

where $\mathbf{B} = [\sigma_1\psi_1, \sigma_2\psi_2, ..., \sigma_J\psi_J]$, $\mathbf{X} = [\chi_1, \chi_2, \cdots, \chi_J]^\top$, and J is the number of resolvent modes to include in the expansion. Then, the state can be reconstructed as

$$\hat{\hat{\mathbf{q}}}(\mathbf{k}) = \mathbf{B}(\mathbf{k})\mathbf{X}(\mathbf{k}). \tag{6.18}$$

6.3 Scaling modal representations to higher Reynolds numbers

In the equilibrium channel flows considered considered in this chapter, turbulent fluctuations obey known scalings with Re_τ. The inner layer motions maintain their sizes in inner units, the outer layer motions scale in outer units, and the logarithmic layer motions are observed to be self-similar. This behavior appears in wave number space, where resolvent analysis gives the expected scalings for wave numbers, mode shapes, and gains for inner, self-similar, and outer-scale modes (Moarref, Sharma, et al., 2013; Moarref, Sharma, et al., 2014).

In this chapter, the subset of scaling rules developed for inner modes are applied to scale the coarse-grained modal representations of inner layer turbulent fluctuations. For inner modes, the wave numbers and wall-normal shape are held constant in inner units. The inner mode amplitude is also kept the same in inner units. The application of these rules means that the modal representations of inner scaled motions calculated from data at a lower Re_τ become smaller in outer units, so the fluctuations have higher spatial frequencies and smaller wall-normal extents.

6.4 Results

In this section, coarse-grained modal representations of near-wall turbulence in (k_x, k_z, ω) are calculated and compared with SPOD to evaluate their efficacy in representing statistics and turbulent motions. Then, the effectiveness of the best-fit resolvent mode representations is also evaluated.

Baseline: SPOD representations of near-wall turbulence

To develop representations of the near-wall motions, SPOD is calculated using a short temporal window. This choice decreases the amount of data required to converge SPOD but sacrifices some resolution of large motions that occur on long time scales. Figure 6.2 verifies that the Reynolds stresses computed from the averaged SPOD approach match well with those obtained using Welch's method on the same short window. The streamwise peak is somewhat lower than that expected at this Reynolds number, and this is attributed to the truncation of large motions which extend down to the wall and contribute to the streamwise peak, but are not captured in the short-windowed analysis. Both the Welch's method and SPOD therefore have 8.2×10^6 modes, which when multiplied by $N_y = 200$ is the degrees of freedom required to describe the data.

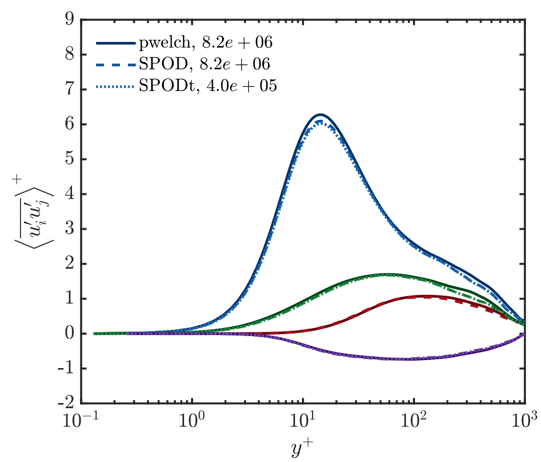

Figure 6.2: Reynolds stresses captured by the Welch's analysis and SPOD containing 8.2×10^6 modes, as well as a truncated SPOD containing 4.0×10^5 modes.

In general, modal representations of turbulence can be truncated but still capture the same energy. One form of truncation has already been applied; the number of SPOD modes for each frequency was truncated to 8 out of a possible 19. The dotted curve in Figure 6.2 shows that when a reduced modal representation (denoted SPODt) is constructed by retaining only the leading 4.0×10^5 modes ranked by streamwise energy content out of a possible 8.2×10^6 modes, and Hermitian and cross-flow symmetries are applied, it is possible to recover the Reynolds stresses. The cross flow symmetry, defined as

$$\begin{aligned} \hat{u}(k_x, -k_z, \omega) &= \hat{u}(k_x, k_z, \omega) \\ \hat{v}(k_x, -k_z, \omega) &= \hat{v}(k_x, k_z, \omega) \\ \hat{w}(k_x, -k_z, \omega) &= -\hat{w}(k_x, k_z, \omega), \end{aligned} \tag{6.19}$$

must at least hold in an integrated sense across wave number space in a channel. Applying the cross-flow symmetry on a wave number by wave number sense is informed by the desire to develop truncated modal representations of near-wall turbulence, which is made more feasible when the symmetry is encoded in the modal basis.

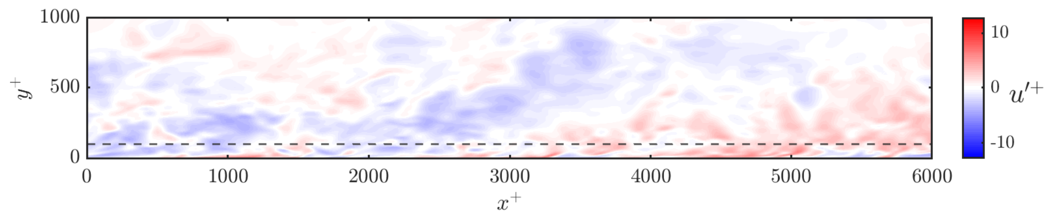

(a)

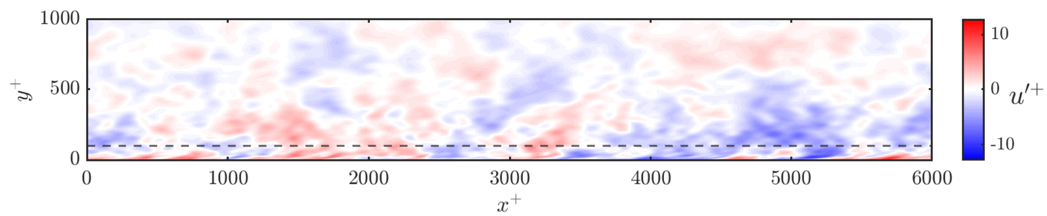

(b)

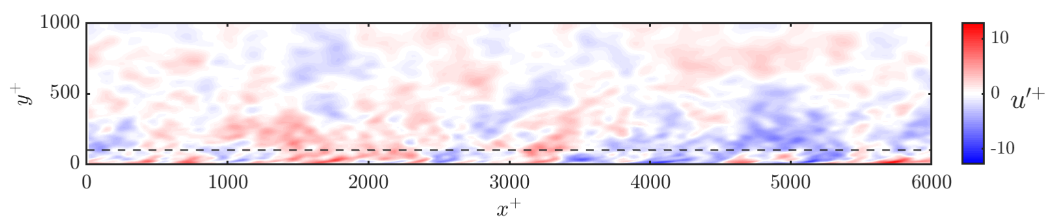

(c)

Figure 6.3: Comparison among (a) streamwise velocity from data, (b) SPOD, and (c) SPODt. The domain shown is $x/\delta \in [0, 6]$, $y/\delta \in [0, 1]$, and $z/\delta = 1.5$. SPOD captures qualitatively similar turbulent motions to the original data, and SPODt reproduces the fluctuations well.

In Figure 6.3, the streamwise velocity fields at $t = 0$ are compared from a data snapshot, SPOD, and SPODt. The data and SPOD agree qualitatively, though the phase encoded in the average SPOD representations is different, such that the fields appear almost as though they are at different times. SPOD and SPODt agree well, indicating that the choice of modes retained in SPODt still capture the energetic streamwise motions.

The SPOD modes can be filtered by their convecting velocities, and the resulting stresses are plotted in Figure 6.4. The modes that convect primarily at speeds

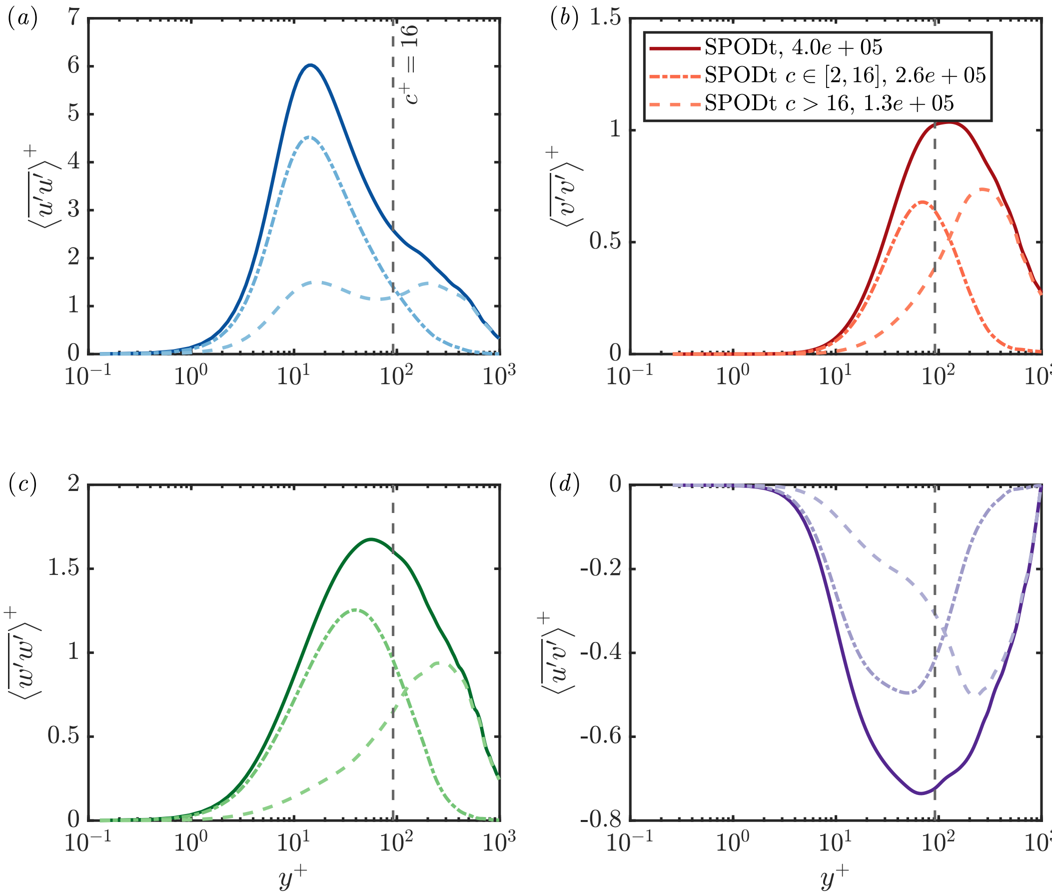

Figure 6.4: Effect of filtering SPOD modes by convecting velocity on the Reynolds (a) streamwise, (b) wall-normal, (c) spanwise, and (d) shear stresses.

characteristic of the mean velocity in the inner region, denoted $c^+ \in [2, 16]$, have peaks primarily in the inner region and represent most of the contribution to the inner peak of streamwise stress. Those inner modes have $\langle \overline{v'v'} \rangle$, $\langle \overline{w'w'} \rangle$, and $\langle \overline{u'v'} \rangle$ stresses that span the inner and outer regions. The modes that convect primarily at speeds characteristic of the outer velocity $c^+ > 16$ have sizeable contributions in the inner and outer layer, so they also contribute to the inner streamwise peak. The outer modes contribute to $\langle \overline{v'v'} \rangle$, $\langle \overline{w'w'} \rangle$, and $\langle \overline{u'v'} \rangle$ stresses mainly in the outer layer. As compared to the 4.0×10^5 modes retained in the SPODt representation, 2.7×10^5 inner modes and 1.3×10^5 outer modes are required to represent the inner and outer layer motions respectively.

In Figure 6.5, xy-planes in physical space of the SPODt and subsets corresponding to the inner and outer modes are plotted. The effect of retaining only modes that have convecting velocities $c^+ \in [2, 16]$ is to represent turbulent motions that occur within the inner region and, to a lesser extent, some motions that occur above the inner

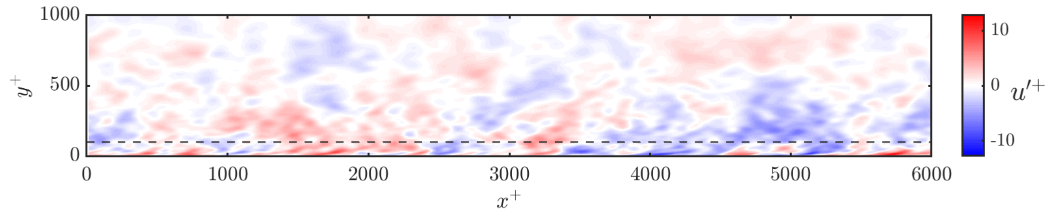

(a)

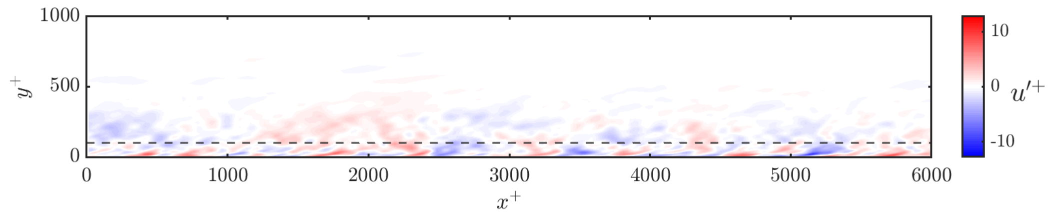

(b)

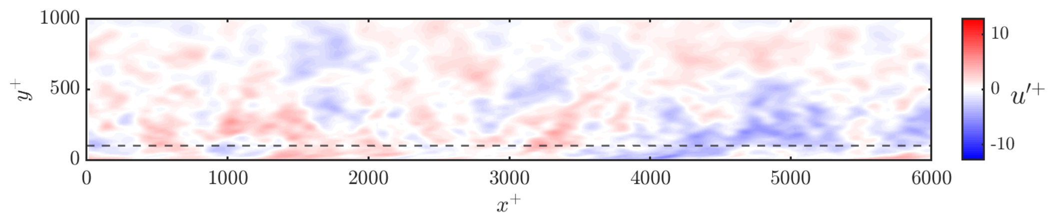

(c)

Figure 6.5: Streamwise velocity fluctuations for SPODt containing (a) all convection speeds, (b) $c^+ \in [2, 16]$, and (c) $c^+ > 16$.

region. The effect of retaining modes that have convecting velocities $c^+ > 16$ is to retain turbulent motions that have significant strength across the domain, including the inner region; these modes reach to the wall. Since this data is at $Re_\tau = 1000$, the inner and outer regions are close together, which contributes to this observed effect. At higher friction Reynolds numbers, the inner and outer regions will be separated by a logarithmic layer of increasing extent in plus units, and the outer layer would be defined by a higher minimum c^+. It is reasonable to assume that by setting a higher minimum c^+, as would be the case in a higher Re_τ flow, that the outer motions might not be uniformly as strong across the domain, though there will still be large-scale motions that reach the wall.

Coarse-grained (k_x, k_z, ω) SPOD modal representations of near-wall turbulence

In this section, the coarse-graining methodology is applied in (k_x, k_z, ω)-space, and the ability of the coarse-grained representations to reproduce the statistics, flow features, and behavior when filtered by convecting velocity is evaluated.

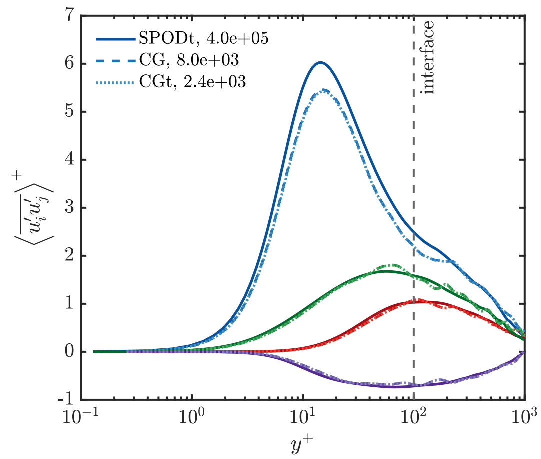

Figure 6.6: Comparison of the Reynolds stresses of the SPODt, coarse-grained (CG), and truncated coarse-grained (CGt) representations.

In Figure 6.6, the Reynolds stresses calculated for coarse-grained representations are compared with the Reynolds stress of SPODt. The coarse-grained SPOD (CG) reproduces the streamwise, wall-normal, spanwise, and shear stresses, though it underestimates the streamwise peak. This behavior is also captured by a truncated version of the coarse grained representation (CGt), based on retaining only the leading modes ranked by their streamwise energy. The CGt representation reproduces the statistics with 2.4×10^3 modes, for a $O(100)$ order of magnitude reduction. The Reynolds stress curves remain reasonably smooth even with the extreme coarse-graining of the wave number space.

In Figure 6.7, the Reynolds stresses for the original truncated SPOD and coarse-grained SPOD are compared for modal representations filtered by wave speed. The behavior of the data is mostly reproduced by the coarse-grained approach, particularly in the streamwise and shear Reynolds stresses. The agreement for the v and w components is not as favorable. This disagreement is possibly attributable to the selection method for representative mode for each bin, which is purely based on the wave number that defines the bin, without any consideration for whether the mode represents the relative phase and magnitude of velocity components obtained from the modes originally in the bin. Nonetheless, the stresses from SPODt and CGt agree reasonably well, and CGt captures that information with an order of magnitude reduction of around $O(100)$.

In Figure 6.8, the physical fields at $z/\delta = 1.5$ between SPODt and CGt retaining wave speeds $c^+ \in [2, 16]$ are plotted. Both representations narrow the wall-normal

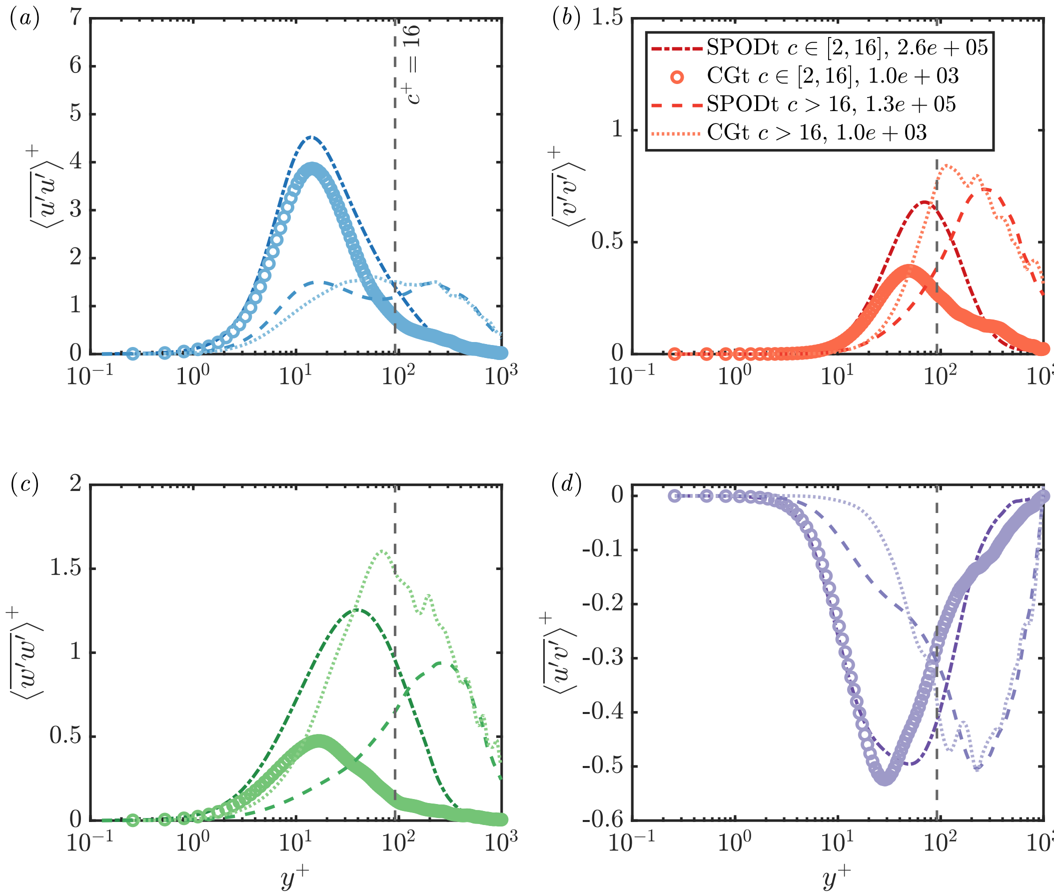

Figure 6.7: The Reynolds (a) streamwise, (b) wall-normal, (c) spanwise, and (d) shear stresses captured by subsets of the SPODt and CGt modal representations corresponding to inner $c^+ \in [2, 16]$ and outer $c^+ > 16$ motions.

extent of fluctuations captured to be mostly at the wall. The general length and size of fluctuations in the inner region appears reasonably similar. The coarse-grained representation appears to have slightly more activity in the outer region, although the magnitude remains low as desired.

In Figure 6.9, the physical fields are compared between SPODt and CGt. Here, the fields do not look as similar, and it appears that small scale activity has been attenuated in the outer region. This may be due to the logarithmic binning of ω; at high ω and high k_x characteristic of smaller scale motions, the bin sizes are larger, so more small scale modes in the outer region are binned together.

Resolvent mode representations of coarse-grained data

The coarse-grained modal representations can be approximated well using resolvent bases. In Figure 6.10, the stresses calculated from coarse-grained representations

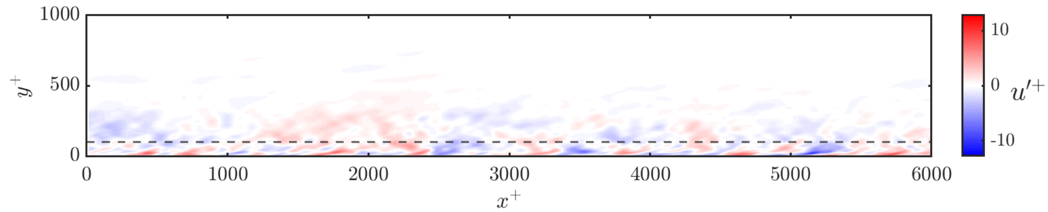

(a)

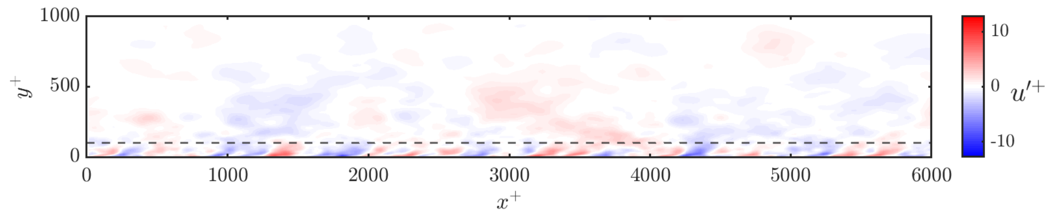

(b)

Figure 6.8: Comparison between (a) coarse-grained SPOD and (b) convection velocity-filtered SPOD (bottom), where $c^+ \in [2, 16]$ was retained.

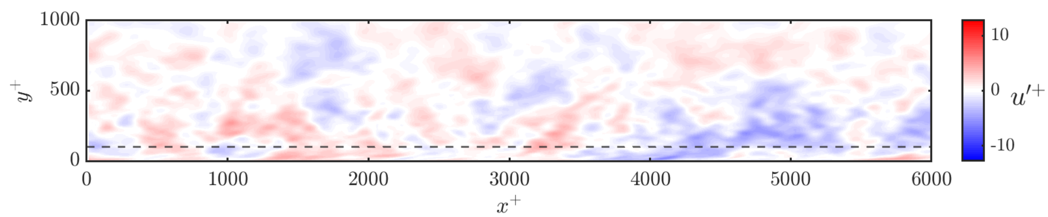

(a)

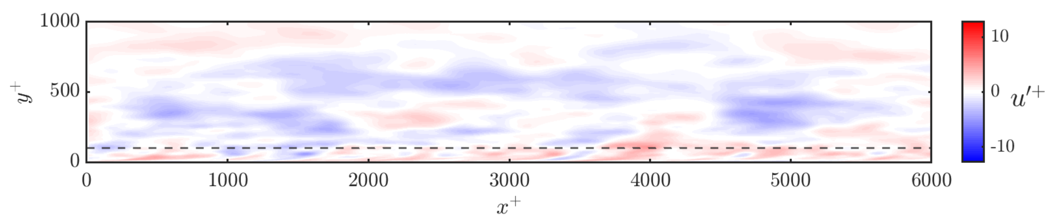

(b)

Figure 6.9: Comparison between (a) coarse-grained SPOD and (b) convection velocity-filtered SPOD (bottom), where $c^+ > 16$ was retained.

and the best-fit local and eddy resolvent mode reconstructions on a $N_y = 240$ Chebyshev grid with 50 SVD modes are compared. The eddy resolvent mode reconstructions reproduce the Reynolds stresses better than the local resolvent mode reconstructions for this number of SVD modes. This may be attributed to the improved ability of the leading eddy resolvent modes to represent mode shapes in turbulence for the wave numbers characteristic of near-wall motions, since the eddy

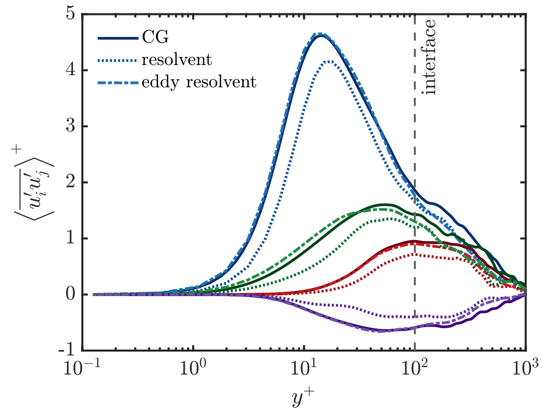

Figure 6.10: Spatiotemporally averaged Reynolds stresses from coarse-grained SPOD, eddy resolvent, and local resolvent reconstructions.

modes embed some information about the flow nonlinearity (Morra et al., 2019; Symon et al., 2023). It is noted that since resolvent modes form a complete basis for the fluctuations, retaining more SVD modes should enable the local resolvent reconstructions to match the Reynolds stresses as well.

6.5 WMLES results incorporating Re_τ-scaled modal representations

In this section, a selection of spatiotemporal modes describing near wall motions is made from the $Re_\tau = 1000$ data. The mode selection criteria, statistics, and appearance of the near wall representation are documented. Then, the modal representations are scaled and inserted into the wall layer of a wall-modeled LES at $Re_\tau = 5200$ by Piomelli et. al. Their results demonstrate the potential utility of spatiotemporal modal representations of near-wall turbulence to augment existing wall modeling schemes in LES.

The modal representation, denoted $\tilde{\mathbf{u}}$, consists of 22 resolvent modes with weights computed to best fit SPOD data at the considered wave numbers. In addition, the modes are amplified to achieve a peak Reynolds shear stress of approximately 20% of the maximum, which permits the usage of a very compact modal representation as a proof-of-concept. The mode selection is made using wave numbers of order $O(10^2-10^3)$ and convecting velocities generally within $c^+ \in [2, 16]$ that are approximately representative of inner layer motions, as plotted in Figure 6.11. Their localization is visualized in Figure 6.12(a), where the modes are plotted in physical space at $Re_\tau = 1000$.

The magnitude of amplification is a tunable parameter for the presented results; adding modes that are not amplified does not change the modeled turbulence significantly, while adding modes that are too highly amplified results in un-physical behavior. The goal for future work is to incorporate the coarse-grained modes, which have already been amplified as part of that modeling scheme.

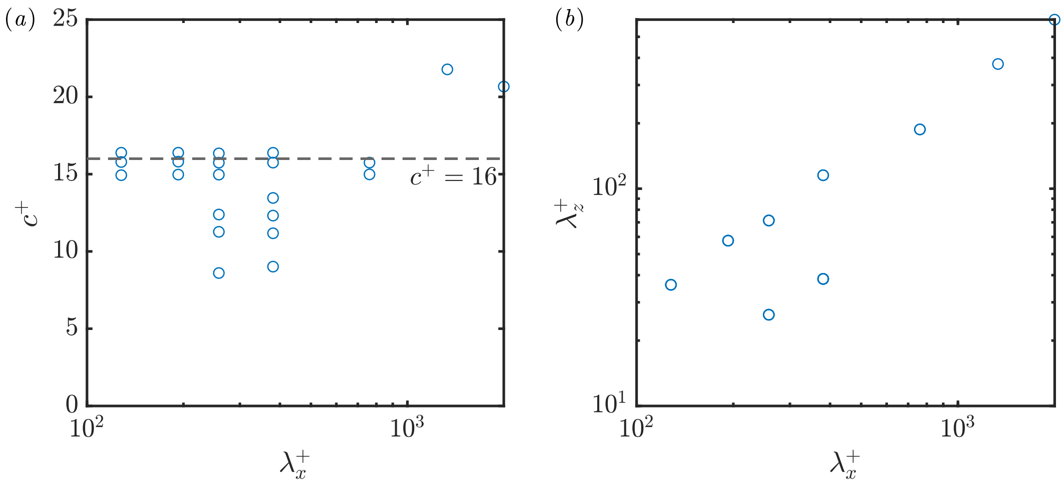

Figure 6.11: Wave number and convecting velocities of the resolvent modes, plotted in (a) (λ_x^+, c^+)-space and (b) $(\lambda_x^+, \lambda_z^+)$-space.

To apply the modes at $Re_\tau = 5200$, the modes are scaled to preserve their dimensions and amplitudes in inner units. The theoretical effect of that scaling is to shrink the spatial extent of the modes in outer units, while the intensity remains similar. This effect is observed in Figure 6.12(b), which depicts the scaled modal representation. The height of the wall layer interface is plotted at $y/\delta = 0.1$ on both plots for reference.

Figure 6.13 shows the Reynolds shear stress components of the modes scaled to $Re_\tau = 5200$. These modes reproduce the streamwise energy peak behavior, and capture shear stress content which spans the inner layer and extends to slightly above the interface.

The modes are transformed into physical space and their contribution $\tilde{\mathbf{u}}$ is added to the wall layer velocity of a WMLES on the embedded grid only; the wall interface ensures that the outer flow matches the wall layer solution across the boundary. Now, the wall layer velocity is given by the sum of a modified inner layer model and the mode contribution $\tilde{\mathbf{u}}$. The inner layer model for the inner layer velocity $\mathcal{U}$ is modified to account for the contribution of the modes,

$$\frac{\partial}{\partial y}\left[(\nu + \nu^*_{T,wm})\frac{\partial \mathcal{U}_i}{\partial y} - \tilde{u}_i\tilde{v}\right] = \frac{1}{\rho}\frac{\partial \mathcal{P}}{\partial x_i} \tag{6.20}$$

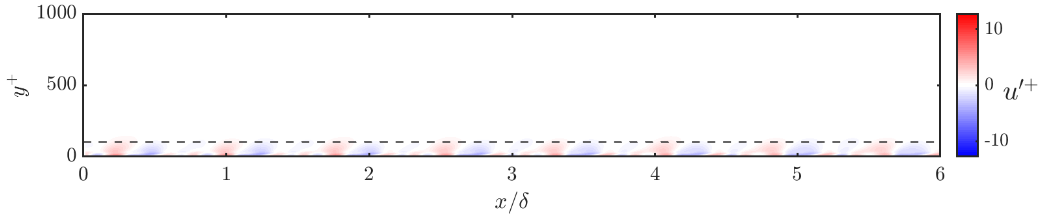

(a)

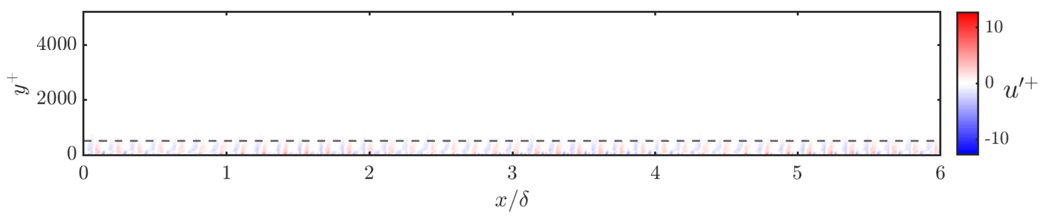

(b)

Figure 6.12: Streamwise velocity fluctuations for the modal representation at (a) $Re_\tau = 1000$ and scaled to (b) $Re_\tau = 5200$.

by adding the $\tilde{u}_i\tilde{v}$ contribution and by using a modified eddy viscosity $\nu^*_{T,wm}$ defined as

$$\nu^*_{T,wm} = \tilde{\kappa}\,[yD(y)]^2\,\frac{\partial \mathcal{U}}{\partial y} \quad \text{where} \quad D(y) = 1 - \exp(-y^+/25) \tag{6.21}$$

that accounts for the mode contribution through a modification to the von Karman constant $\tilde{\kappa}$. For a channel, $\tilde{\kappa}$ is given by,

$$\widetilde{\kappa}^2 = \kappa^2 + \frac{\langle \widetilde{u}\widetilde{v} \rangle}{y^2\left\langle D^2(y)\right\rangle \left|\frac{\partial\langle\mathcal{U}\rangle}{\partial y}\right| \frac{\partial\langle\mathcal{U}\rangle}{\partial y}}. \tag{6.22}$$

Therefore, in this formulation, the turbulent motions influence the near wall stress directly by making their own contribution, as well as by exciting additional inner layer motions through $\tilde{u}_i\tilde{v}$ where $i = 1, 2$ for the stresses formed by the wall-normal velocity and the streamwise and spanwise components respectively.

In Figure 6.14, the effect of including the modal representation in the wall layer of WMLES is evaluated by comparing the streamwise stress behavior with DNS data from M. Lee and Moser, 2015 and a baseline WMLES using an equilibrium wall model. The baseline WMLES underestimates the streamwise energy intensity in the inner layer compared to the DNS results. Adding the modes to the inner layer of WMLES has two effects. First, the modes excite additional activity in the inner layer model solution, modifying the stress from the inner velocity $\langle \mathcal{U}'\mathcal{U}' \rangle$. Second, the modes add their own contribution to the streamwise energy content

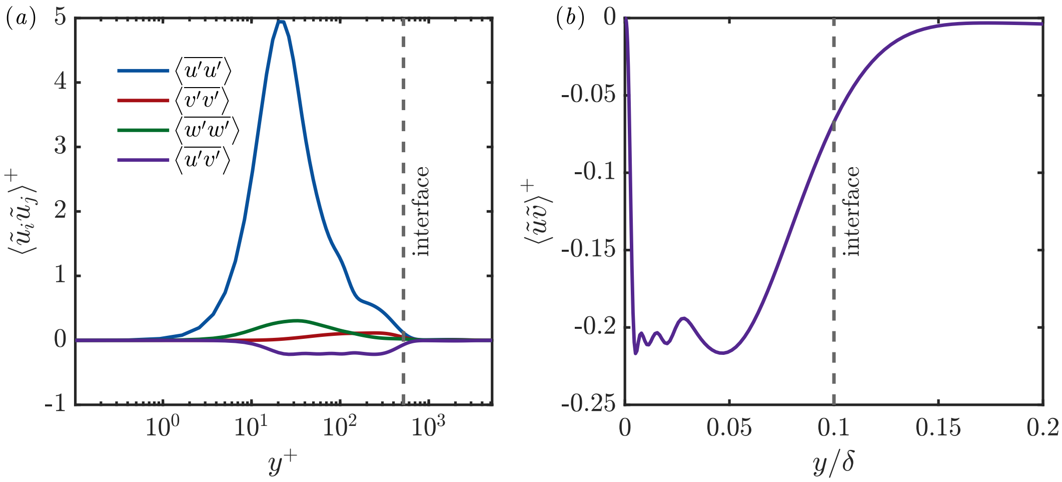

Figure 6.13: (a) Reynolds stress components plotted for the near wall representation on inner spatial units and (b) the Reynolds shear stress component on outer spatial units.

$\tilde{u}\tilde{u}$. These additions sum, resulting in an increase in the peak streamwise stress that approximately matches the behavior observed in the DNS. Outside of the wall layer, both WMLES schemes match and underestimate the DNS, which is expected because on a coarse grid, the WMLES statistics will never match the DNS in the outer region. However, in the inner region, the addition of the modes improves the streamwise stress, demonstrating the potential of the method to improve the modeling capabilities of WMLES.

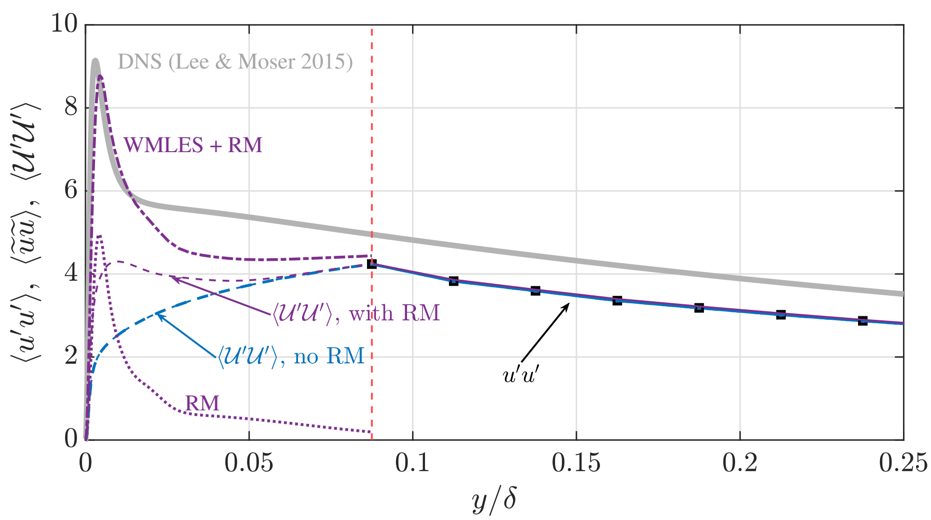

Figure 6.14: Comparison of the streamwise stress from DNS, WMLES, and WMLES with the resolvent mode-based near-wall representation of turbulent motions.

6.6 Conclusions

In this work, a method for producing dynamic coarse-grained modal representations of near-wall turbulent motions is presented, which drastically reduces the number of modes required to represent turbulent motions and statistics. An averaged SPOD is developed to generate a spatiotemporal representation of a time series of flow fields, and that representation is rebinned on logarithmically spaced axes, where each bin is represented by a mode which is amplified to preserve the energetic content of the bin. Those amplified modes retain amplitude and phase information. The logarithmic rebinning maintains the distinction of large wavelength modes while binning small wavelength modes together, so that the flow motions captured by larger wavelength modes convecting at different speeds are captured in the coarse-grained representations. The coarse-grained modal representations reproduce the qualitative appearance of the turbulent fluctuations and the spatiotemporally averaged Reynolds stresses at a degree-of-freedom reduction of $O(100)$. Future work could include developing ways of using the data compression capabilities of the coarse-graining algorithm to assist with data storage and super-resolution.

The coarse-grained modal representations are amenable to reconstruction by resolvent modes and rescaling to represent turbulent motions at higher Reynolds numbers. The choice of resolvent mode basis can be informed by the knowledge that resolvent mode bases constructed with an eddy viscosity reconstruct the Reynolds stresses more readily with fewer SVD modes. The inner layer motions from $Re_\tau = 1000$ can be scaled to $Re_\tau = 5200$ by scaling the wave numbers and mode shapes using rules from resolvent analysis.

Finally, a compact resolvent mode representation of near-wall motions is developed by choosing convecting velocities and wave numbers representative of inner layer motions. The representation is scaled from $Re_\tau = 1000$ to $Re_\tau = 5200$ and added to the wall layer of a WMLES by Piomelli et. al. The addition of the resolvent modes improves the streamwise stress resolved by the simulation as compared with WMLES with an equilibrium wall model. The improvement is such that it matches the streamwise stress from DNS at the same Reynolds number. These results demonstrate the predictive promise of the methods for calculating compact resolvent mode representations of turbulence developed in this chapter. It also motivates future development on using resolvent mode scaling to make predictions for flow motions in the logarithmic region which grows with Reynolds number, since these motions make up the majority of the WMLES wall layer at higher Re_τ.

Chapter 7

CONCLUSIONS AND FUTURE WORK

This thesis contributes to the capabilities of reduced order modeling techniques to capture roughness sublayer turbulence in multiscale roughness geometries, and the construction of compact modal representations of near-wall turbulence with applications to wall-modeling schemes in LES. First, a physics-based reduced-order model is developed to predict the sensitivity of the spatially-varying roughness sublayer turbulence to a multiscale roughness geometry using resolvent analysis with a drag-normalized, Reynolds-decomposed volume penalization term. This model provides computationally inexpensive, quantitatively useful predictions of the roughness sublayer turbulence and mean flow profile over a multiscale roughness geometry, capabilities which are only partially addressed by other methods in the literature which seek to bypass the details of the roughness sublayer fluctuations and connect the statistics and spectra of the surface geometry directly to the mean response. This model has the potential to predict these flow quantities for realistic surfaces that have not been previously tested in numerical or physical experiments. The coarse-graining chapter develops a method for capturing motions in near-wall turbulence using a modal representation with a large decrease in degrees of freedom, which admits scaling rules developed for modal representations to make predictions for near-wall motions at higher Reynolds numbers. These predictions are used in the WMLES of Piomelli et. al to improve the matching of the streamwise velocity statistics between DNS and WMLES of a channel flow, and points towards how to use data-driven, scaled modal representations in conjunction with physics knowledge to make predictions outside of the original training data.

In Chapter 3, the ability of a resolvent mode basis developed using different mean flow profiles with standard no-slip, no-penetration boundary conditions at the wall to model wake field $\omega = 0$ fluctuations in the turbulent flow over sand grain roughness in the fully rough regime is evaluated using weights calculated to best reconstruct the observed fluctuations. The analysis reveals that a resolvent mode basis developed using a smooth wall mean and standard boundary conditions at the walls can still represent the wake field velocity fluctuations effectively. Furthermore, those wake field velocities also represent components of the wake field pressure and can be used to model the pressure force on roughness elements, and an approximate linear relationship between the weights and modes of the surface geometry exists in the turbulent flow over a multiscale roughness geometry. Finally, a modeling framework for the wake field is developed using the physics-based resolvent modes and a data-informed model for the weights utilizing the average linear relationship identified between the surface roughness modes. This framework represents a way of using data to inform the description of turbulence using resolvent modes. However, the data-informed model is evaluated and shown to not perform well for the given flow.

The promise embedded in a linear model for wake field fluctuations even in a multiscale roughness geometry motivates the development of a physics-based method to model resolvent mode weights as linearly related with the surface geometry. In Chapter 4, resolvent analysis with a drag-normalized, Reynolds-decomposed treatment of the volume penalization is developed to model roughness sublayer fluctuations given only a mean flow profile and the roughness geometry. The key insight that the magnitude of the volume penalization should be scaled to give the correct magnitude of integrated inner-scaled drag force allows a simple closure of the model. RAVP gives resolvent modes that are descriptive of the wake field fluctuations even at low SVD rank, and mode weights which contain the contributions from a linear relationship with the roughness geometry, the usual nonlinear term in the fluctuations, and the interaction between the roughness geometry and fluctuations at other wave numbers. It is shown that modeling using only the portion that linearly relates the surface geometry and the fluctuations is sufficient to make predictions of the wake field fluctuations and dispersive stresses. In addition, RAVP predicts the relationship between the shape of the drag force profile and the mean flow profile. RAVP works for a multiscale roughness, and future work should include the characterization of the model performance over other realistic roughness geometries. In addition, RAVP should be applied to convecting ($\omega \neq 0$) modes, with the goal of determining approaches to approximate the stochastic fluctuations and stresses.

Oftentimes, quantities related to the mean flow, such as the Hama roughness function, equivalent sand grain roughness, and the shape of the mean flow profile are the quantities of interest for engineers in a given bulk flow. In Chapter 5, a modeling framework for mean flow quantities is developed that takes advantage of the link between the roughness sublayer fluctuations and the mean flow profile embedded in the RAVP methodology. The framework is iterative; for a desired bulk flow and starting from a modeled smooth wall mean flow profile, the method predicts the fluctuations, drag force, and stresses, updates the mean flow profile, and iterates until the rough wall mean profile is predicted for the given bulk flow. This work gives a different perspective on the modeling problem for the rough wall mean flow profile; previous modeling methodologies in the literature for rough surfaces are based on fitting the parameters of a model form to data. By modeling the mean flow profile as the sum of the stresses which define its shape, and closing the model by capturing the relationship between the stresses and the mean flow profile encoded in RAVP and a modeled rough wall eddy viscosity, this model has almost all of the ingredients for a fully physics-based framework for predicting the mean flow profile and mean quantities of interest over an arbitrary surface geometry using reduced order modeling. One important avenue of development for this modeling methodology is to improve or find an alternative to the eddy viscosity profile for relating the stochastic stress to the mean, which would reduce the remaining empiricism embedded in the model. One clear avenue for this is to investigate the modeling of the stochastic fluctuations and stresses using RAVP itself. Another, more speculative suggestion for future study is to incorporate the physical relationships embedded in RAVP and this mean flow model into the regularization of physics-informed neural networks, which may improve out-of-sample performance and enable these methods to predict more than k_s^+.

Finally, in Chapter 6, a coarse-graining method is presented which dramatically reduces the number of modes required to describe the statistics and motions of turbulence in channel flow. Methods for selecting modes that represent motions in particular regions of the flow are developed, and a Reynolds-number-scaled representation of inner region motions is placed in the wall layer of an WMLES in collaboration with Piomelli et. al. Its inclusion improves the agreement between the streamwise energy peaks from DNS and that of the wall layer velocity in WMLES. The coarse-graining method takes spatiotemporal modal representations of data in (k_x, k_z, ω)-space onto logarithmically spaced bins. This representation permits an extremely compact representation of the turbulence, with a degree of freedom reduction of $O(10^2)$ times. To determine which modes are retained in a near-wall turbulence representation for input into a wall-modeling scheme, criteria for selecting modes based on metrics, wave number, and wall-normal localization are developed. Future work should include working out how to form a spatiotemporal representation in (k_x, k_z, c)-space, which lends itself naturally to the representation of turbulence as the superposition of convecting motions. Another important avenue for future work is to apply the scaling findings of Moarref, Sharma, et al., 2014 to extend the predictions of higher Reynolds number turbulence to self-similar modes. Also, developing methods for data storage and super-resolution using the data compression capabilities of the coarse-graining methodology could be a useful pathway for future research.

Overall, this thesis contributes to the development of physics-based methods for reduced order modeling of near wall and roughness sublayer turbulence to give generalizable insights. The resolvent analysis method forms a transfer function between the surface and 3D flow response that yields the drag and turbulent fluctuations, which goes beyond the capabilities of existing empirical methods. The physical insights embedded in RAVP offer a particular lens through which to understand the sensitivity of turbulence and drag to surface roughness, which are generally useful and could also be applied in other modeling architectures. The coarse-graining methodology and mode selection criteria represent a promising step towards Reynolds-number-scalable modal representations of turbulence that augment wall layer prediction schemes for wall modeled simulations.

BIBLIOGRAPHY

Abdelaziz, M. et al. (2024). "On predictive models for the equivalent sand grain roughness for wall-bounded turbulent flows". In: *Phys. Fluids*.

Aghaei Jouybari, M. et al. (2021). "Data-driven prediction of the equivalent sand-grain height in rough-wall turbulent flows". In: *J. Fluid Mech.* 912, A8.

Alves Portela, F., A. Busse, and N. D. Sandham (Aug. 2021). "Numerical study of Fourier-filtered rough surfaces". In: *Phys. Rev. Fluids* 6 (8), p. 084606.

Bornhoft, B. (2024). "Large eddy simulation of aircraft icing aerodynamics". Stanford University.

Brereton, G. and J. Yuan (Oct. 2018). "Wall-roughness eddy viscosity for Reynolds-averaged closures". In: *Int. J. Heat Fluid Flow* 73, pp. 74–81.

Brown, G. and A. Roshko (1974). "On density effects and large structure in turbulent mixing layers". In: *J. Fluid Mech.* 64.4, pp. 775–816.

Busse, A., M. Thakkar, and N. Sandham (2017). "Reynolds-number dependence of the near-wall flow over irregular rough surfaces". In: *J. Fluid Mech.* 810, pp. 196–224.

Cess, R. (1958). "A survey of the literature on heat transfer in turbulent tube flow". In: *Res. Rep*, pp. 8–0529.

Chavarin, A. and M. Luhar (Feb. 2020). "Resolvent Analysis for Turbulent Channel Flow with Riblets". In: *AIAA Journal* 58.2, pp. 589–599.

Chung, D. et al. (2021). "Predicting the Drag of Rough Surfaces". In: *Annu. Rev. Fluid Mech.* 53.Volume 53, 2021, pp. 439–471.

Colebrook, C. (1939). "Turbulent flow in pipes, with particular reference to the transition region between the smooth and rough pipe laws". In: *J. Inst. Civil Eng.* 11.1, pp. 133–156.

Del Álamo, J. and J. Jiménez (2009). "Estimation of turbulent convection velocities and corrections to Taylor's approximation". In: *J. Fluid Mech.* 640, pp. 5–26.

Flack, K. and D. Chung (2022). "Important Parameters for a Predictive Model of k_s for Zero Pressure Gradient Flows". In: *AIAA Journal* 60.10, pp. 5923–5931.

Flack, K. and M. Schultz (Apr. 2010). "Review of Hydraulic Roughness Scales in the Fully Rough Regime". In: *J. Fluids Eng.* 132.4, p. 041203.

Flack, K., M. Schultz, and J. Barros (Mar. 2020). "Skin Friction Measurements of Systematically-Varied Roughness: Probing the Role of Roughness Amplitude and Skewness". In: *Flow Turbul. Combust.* 104.2–3, pp. 317–329.

Flynn, Z., H. Bae, and A. Goza (2024). “Towards an Immersed-Boundary Resolvent Analysis Framework for Wall-Bounded Flows With Various Surface Configurations”. In: *AIAA Aviation Forum and Ascend 2024*.

Forooghi, P. et al. (Aug. 2017). “Toward a Universal Roughness Correlation”. In: *J. Fluids Eng.* 139.12, p. 121201.

Grinstein, F., P. F.S., and G. M. (2025). *Coarse Graining Turbulence: Modeling and Data-Driven Approaches and their Applications*. Cambridge University Press.

Hama, F. (1954). “Boundary-Layer Characteristics for Smooth and Rough Surfaces”. In: *Trans. SNAME* 62, pp. 333–393.

Hantsis, Z. (Nov. 2022). “Effects of Roughness on Passive-Scalar Transport”. PhD thesis. Queen’s University.

Hantsis, Z. and U. Piomelli (Nov. 2020). “Roughness effects on scalar transport”. In: *Phys. Rev. Fluids* 5 (11), p. 114607.

Huynh, D., Y. Huang, and B. McKeon (2021). “Experiments and Modeling of a Compliant Wall Response to a Turbulent Boundary Layer with Dynamic Roughness Forcing”. In: *Fluids* 6.5.

Jackson, P. (1981). “On the displacement height in the logarithmic velocity profile”. In: *J. Fluid Mech.* 111, pp. 15–25.

Jafari, A., B. McKeon, and M. Arjomandi (2023). “Frequency-tuned surfaces for passive control of wall-bounded turbulent flow – a resolvent analysis study”. In: *J. Fluid Mech.* 959, A26.

Jiménez, J. (2004). “Turbulent Flows Over Rough Walls”. In: *Ann. Rev. Fluid Mech.* 36.Volume 36, pp. 173–196.

Kadivar, M., D. Tormey, and G. McGranaghan (2021). “A review on turbulent flow over rough surfaces: Fundamentals and theories”. In: *Int. J. Thermofluids* 10, p. 100077.

Keating, A. et al. (2004). “Large-eddy simulation of heat transfer downstream of a backward-facing step”. In: *J. Turbul.* 5, N20.

Kline, S. J. et al. (1967). “The structure of turbulent boundary layers”. In: *J. Fluid Mech.* 30.4, pp. 741–773.

Kuwata, Y. and Y. Kawaguchi (2019). “Direct numerical simulation of turbulence over systematically varied irregular rough surfaces”. In: *J. Fluid Mech.* 862, pp. 781–815.

Lee, M. and R. Moser (2015). “Direct numerical simulation of turbulent channel flow up to $Re_\tau \approx 5200$”. In: *J. Fluid Mech.* 774, pp. 395–415.

Lee, S. et al. (Feb. 2022). “Predicting drag on rough surfaces by transfer learning of empirical correlations”. In: *J. Fluid Mech.* 933, A18.

Luhar, M., A. Sharma, and B. McKeon (2015). "A framework for studying the effect of compliant surfaces on wall turbulence". In: *J. Fluid Mech.* 768, pp. 415–441.

Lumley, J. (1970). *Stochastic tools in turbulence*. Academic Press.

Marusic, I., R. Mathis, and N. Hutchins (2010). "Predictive Model for Wall-Bounded Turbulent Flow". In: *Science* 329.5988, pp. 193–196.

Marusic, I., J. Monty, et al. (2013). "On the logarithmic region in wall turbulence". In: *J. Fluid Mech.* 716, R3.

McKeon, B. and A. Sharma (2010). "A critical-layer framework for turbulent pipe flow". In: *J. Fluid Mech.* 658, pp. 336–382.

Mejia-Alvarez, R. and K. Christensen (2010). "Low-order representations of irregular surface roughness and their impact on a turbulent boundary layer". In: *Phys. Fluids* 22.1, p. 015106.

Meneveau, C., N. Hutchins, and D. Chung (2024). "The wind-shade roughness model for turbulent wall-bounded flows". In: *J. Fluid Mech.* 1001, A3.

Moarref, R., M. Jovanović, et al. (May 2014). "A low-order decomposition of turbulent channel flow via resolvent analysis and convex optimization". In: *Phys. Fluids* 26.5, p. 051701.

Moarref, R., A. Sharma, et al. (2013). "Model-based scaling of the streamwise energy density in high-Reynolds-number turbulent channels". In: *J. Fluid Mech.* 734, pp. 275–316.

– (2014). "A foundation for analytical developments in the logarithmic region of turbulent channels". In: *arXiv:1409.6047*.

Morgan, J. (Feb. 2019). "Linear and Non-linear Interactions in a Rough-Wall Turbulent Boundary Layer". PhD thesis. California Institute of Technology.

Morra, P. et al. (2019). "On the relevance of Reynolds stresses in resolvent analyses of turbulent wall-bounded flows". In: *J. Fluid Mech.* 867, pp. 969–984.

Nekkanti, A. and O. Schmidt (2021). "Frequency–time analysis, low-rank reconstruction and denoising of turbulent flows using SPOD". In: *J. Fluid Mech.* 926, A26.

Nikuradse, J. (1933). "Strömungsgesetze in rauhen Rohren". In: *VDI-Forschungsheft* 361. Based on sand grain experiments, Nikuradse's work defined a friction factor for rough pipes based on the relative roughness (k/D)., pp. 1–22.

Perry, A. E. and M. S. Chong (1982). "On the mechanism of wall turbulence". In: *J. Fluid Mech.* 119, pp. 173–217.

Raupach, M. (1981). "Conditional statistics of Reynolds stress in rough-wall and smooth-wall turbulent boundary layers". In: *J. Fluid Mech.* 108, pp. 363–382.

Reynolds, O. (1883). “XXIX. An experimental investigation of the circumstances which determine whether the motion of water shall be direct or sinuous, and of the law of resistance in parallel channels”. In: *Philos. Trans. R. Soc.* 174, pp. 935–982.

Rosenberg, K. and B. McKeon (Aug. 2019). “Computing exact coherent states in channels starting from the laminar profile: A resolvent-based approach”. In: *Phys. Rev. E* 100 (2), p. 021101.

Schmid, P. (2010). “Dynamic mode decomposition of numerical and experimental data”. In: *J. Fluid Mech.* 656, pp. 5–28.

Scotti, A. (Mar. 2006). “Direct numerical simulation of turbulent channel flows with boundary roughened with virtual sandpaper”. In: *Phys. Fluids* 18.3, p. 031701.

Symon, S. et al. (June 2023). “Use of eddy viscosity in resolvent analysis of turbulent channel flow”. In: *Phys. Rev. Fluids* 8 (6), p. 064601.

Toedtli, S., M. Luhar, and B. McKeon (July 2019). “Predicting the response of turbulent channel flow to varying-phase opposition control: Resolvent analysis as a tool for flow control design”. In: *Phys. Rev. Fluids* 4 (7), p. 073905.

Toedtli, S., C. Yu, and B. McKeon (2020). “On the origin of drag increase in varying-phase opposition control”. In: *Int. J. Heat Fluid Flow* 85, p. 108651.

Towne, A., O. Schmidt, and T. Colonius (2018). “Spectral proper orthogonal decomposition and its relationship to dynamic mode decomposition and resolvent analysis”. In: *J. Fluid Mech.* 847, pp. 821–867.

Townsend, A. (1976). *The structure of turbulent shear flow, 2nd ed.* Cambridge Univ. Pr.

Weideman, J. and S. Reddy (2000). “A MATLAB Differentiation Matrix Suite”. In: *ACM Transactions on Mathematical Software (TOMS)* 26.4, pp. 465–519.

Yang, J. et al. (Nov. 2023). “Prediction of equivalent sand-grain size and identification of drag-relevant scales of roughness – a data-driven approach”. In: *J. Fluid Mech.* 975, A34.

Yuan, J. (2015). “Numerical simulations of rough-wall turbulent boundary layers”. PhD thesis. Queens University.

Yuan, J. and U. Piomelli (2014). “Roughness effects on the Reynolds stress budgets in near-wall turbulence”. In: *J. Fluid Mech.* 760, R1.